Synergistic Effects in Magnesium-Rare-Earth-Zinc Alloys - A Gateway to Informed Alloy Design

Von der Fakultät für Georessourcen und Materialtechnik der Rheinisch-Westfälischen
Technischen Hochschule Aachen

zur Erlangung des akademischen Grades einer
Doktorin der Ingenieurwissenschaften

genehmigte Dissertation

vorgelegt von

Fatim Zahra Mouhib, M. Sc. RWTH

Berichter: Univ.-Prof. Dr. Sandra Korte-Kerzel
Prof. Dr. Chad Sinclair

Tag der mündlichen Prüfung: 17.01.2024

F. Z. Mouhib et al. “Texture Selection Mechanisms during Recrystallization and Grain Growth of a Magnesium-Erbium-Zinc Alloy”. In: Metals 11.1 (2021), DOI: 10.3390/ met11010171.

F. Z. Mouhib et al. “Synergistic effects of solutes on active deformation modes, grain boundary segregation and texture evolution in Mg-Gd-Zn alloys”. In: Materials Science and Engineering: A 847 (2022), DOI: 10.1016/j.msea.2022.143348.

F. Z. Mouhib et al. “On the role of selective nucleation and growth to recrystallization texture development in a Mg-Gd-Zn alloy”. In: Journal of Materials Science 59 (2023), DOI: https://doi.org/10.1007/s10853-023-09243-3.

F. Z. Mouhib et al. “Exploring solute behavior and texture selection in magnesium alloys at the atomistic level”. In Acta Materialia 266 (2024),
DOI: https://doi.org/10.1016/j.actamat.2024.119677.

J. Guénolé et al. ”Basal slip in laves phases: The synchroshear dislocation” In: Scripta Materialia 166 (2019), DOI: 10.1016/j.scriptamat.2019.03.016.

D 82 (Diss. RWTH Aachen University, 2024)

Acknowledgements

Ich möchte mich an dieser Stelle für jegliche Hilfe, die mir während meiner Promotion entgegengebracht wurde bedanken. Besonderer Dank gilt der Institutsleitung Prof. Sandra Korte-Kerzel und dem Fachgruppenleiter für Magnesium Dr. Talal Al Samman für die Möglichkeit zur Promotion und der fortlaufendenden Unterstützung bei dieser. Auch möchte ich mich bei Dr. Julien Guénolé für die Betreuung meiner Masterarbeit und die damit verbundene Einführung in wissenschaftliches Arbeiten bedanken. Für die Finanzierung meiner Promotion im Rahmen des Forschungsprojekts AL 1343/7-1 bedanke ich mich bei der Deutschen Forschungsgemeinschaft (DFG). Dr. Talal Al Samman möchte ich zusätzlich für zahlreiche konzeptionelle und analytische Diskussionen danken. Neben Dr. Talal Al-Samman, möchte ich mich auch bei Dr. Risheng Pei für die Möglichkeit von seiner Erfahrung im Feld der Magnesiumforschung zu profitieren bedanken.

In diesem Sinne bedanke ich mich bei allen Mitarbeitern des Instituts für ihre Hilfsbereitschaft und tatkräftige Unterstützung. Auch möchte ich mich bei Allen für eine gute Atmosphäre und angenehme Pausen bedanken. Dank gebührt an dieser Stelle, Setareh Medghalchi, Dr. Carl Kusche, Dr. Doreen Andre, und Mattis Seehaus, die meine Promotion mit fachlichen Gesprächen und meist konstruktiven Pausen bereichert haben. Zudem gilt ein besonderer Dank meinen studentischen Hilfswissenschaftlern und Abschlussarbeitern, Venkatesh Pandian, Bugra Koksal, Ramandeep Pandian, Burak Erol, Fengyang Sheng und Bohang Gao, die mich während meiner Promotion unterstützt haben. Ihre Kooperation und Bereitschaft hat einige interessante Ergebnisse und Erkenntnisse ermöglicht. Ein besonderer Dank gebührt auch allen Co-Autoren, die mit ihrer Expertise und Mitarbeit, die Publikationen die meiner Promotion zugrundeliegen ermöglicht haben.

Für die Unterstützung bei der Probenpräparation, technischen und organisatorischen Aspekten, möchte ich mich bei David Beckers, Arndt Ziemons, Nico Poschmann, Sergej Laiko und allen weiteren technischen Mitarbeitern, sowie dem Sekretariat bedanken.

Abschließend möchte ich mich bei meiner Familie, insbesondere bei meinen Eltern und Geschwistern, für Unterstützung und Zuspruch während meiner Promotionszeit bedanken.

Vielen Dank!

Abstract

In dilute magnesium (Mg) alloys, solute effects were proven crucial for microstructure and texture development rendering a deep understanding of solute-solute and solute-defect interactions indispensable for property predictions and alloy design. This dissertation aimed at clarifying the underlying factors contributing to the formation of texture components deviating from the common basal texture in ternary magnesium-rare earth (RE) -zinc (Zn) alloys. The main focus was on understanding the role of solute-defect interactions and resulting synergistic solute effects. A multi-scale characterization involving classical electron backscatter diffraction (EBSD) analysis, mechanical testing, and atom probe tomography (APT) was adopted to establish microstructure correlations concerning atomic scale segregation phenomena, slip activation and arising material properties.

Binary and ternary dilute Mg-Gd-(Zn), Mg-Er-(Zn) and Mg-Ca-(Zn) alloy sheets were investigated subsequent to rolling deformation and various heat treatments. The results confirmed the formation of a unique ±40° transverse direction (TD) recrystallization texture in ternary Mg-RE-Zn alloys. A texture transition from an RD to an TD dominated texture was found to take place during the early stages of recrystallization. To understand texture selection during recrystallization, further investigations on nucleation and early nucleus growth during static recrystallization were carried out. An as-cast Mg-Gd-Zn sample was subjected to uniaxial compression at 200°C up to 40% strain and subsequently cut into two mirroring sample halves of which one was annealed for 60 min. Classical and quasi-in-situ EBSD analysis proved the importance of specific nucleation sites, especially compression-tension double twins, to the final texture. Quasi-insitu EBSD investigations revealed selective growth of off-basal texture components, which would ultimately dominate the resulting recrystallization texture. Combined solute effects and their dependence on the solute ratio, were explored by comparing solute segregation and texture formation of three Mg-Gd-Zn alloys, with varying Gd:Zn ratios of 2:1, 1;1 and 1:2. A low Gd:Zn ratio led to higher solute segregation and a more pronounced TD texture. Solute clusters with a ratio of approximately 0.33 were found in all alloys indicating that the formation of effective solute clusters may require a high Zn concentration. These results prove that alterations of the solute ratio rather than the absolute solute concentration govern segregation and texture formation.

A possible replaceability of RE solutes by Ca, was addressed by EBSD investigations, atom probe tomography and ab initio calculations of binary and ternary Mg-Gd-(Zn) and Mg-Ca-(Zn) alloys. Texture investigations showed similar off-basal texture trends in Mg-Ca alloys compared to RE containing alloys. However, significant combined solute effects were observed in ternary RE containing alloys, e.g. Mg-Gd-Zn, rather than the counterpart Ca alloy. Ab initio calculations of binding energies revealed preferential Ca-Zn binding compared to Ca-Zn. Additionally, solute-vacancy binding was investigated to estimate the behaviour of solutes in vacancy rich regions, e.g. grain boundaries, and revealed that solute-vacancy binding is preferential for Ca rather than Gd, which may explain the off-basal texture trends emerging in binary Mg-Ca.

In terms of mechanical properties, Mg-Er-Zn and Mg-Gd-Zn both exhibited an enhancement in the yield strength, strain hardening capability, and failure ductility compared to binary alloy systems. EBSD-assisted slip trace analysis at 5% strain showed promoted non-basal slip in ternary alloys compared to the binary counterpart alloy. Alterations of the Gd:Zn ratio lead to further enhancements of non basal slip activation for lower Gd:Zn ratios. Additionally, a RD/TD yield stress anisotropy, equally scaling with the Gd:Zn ratio, was observed and attributed to an increased activation of twinning under strain in TD. To explore alternative deformation modes in Mg-Ca alloys synchroshear in Mg_2Ca Laves phases was investigated by classical atomistic simulation and ab initio calculations. It was proven that synchro-shear is energetically favorable and therefore the main mechanism for dislocation motion on the basal plane.

Zusammenfassung

In Magnesiumlegierungen haben sich die Auswirkungen gelöster Legierungselementen als entscheidend für die Entwicklung von Mikrostruktur und Textur erwiesen, so dass ein tiefes Verständnis der Wechselwirkungen zwischen gelösten Elementen und Gitterfehlern für die Vorhersage von Eigenschaften und das Legierungsdesign unerlässlich ist. Ziel dieser Studie war es, die zugrundeliegenden Faktoren zu klären, die dazu beitragen, dass die Texturkomponenten in ternären Magnesium (Mg)-seltenen Erden (SE)-Zinc (Zn)-Legierungen von der üblichen Basaltextur abweichen. Der Fokus lag dabei auf dem Verständnis der Wechselwirkungen zwischen gelösten Elementen und Gitterfehlern, sowie synergistischen Effekten der gelösten Elementen untereinander. Es wurde ein kombinierter Ansatz aus klassischer Elektronenrückstreubeugung (EBSD), mechanischer Prüfung und Atomsondentomographie gewählt, um Mikrostrukturentwicklung ausgehend von Korngrenzseigerungsphänomenen auf atomarer Ebene und Versetzungsgleiten, bis hin zu den endgültigen Materialeigenschaften zu untersuchen.
Binäre und ternäre Mg-Gd-(Zn)-, Mg-Er-(Zn)- und Mg-Ca-(Zn)-Walzbleche wurden nach Abschluss verschiedener Wärmebehandlungen untersucht. Die Ergebnisse bestätigten die Bildung einer einzigartigen ±40° Kippung zur Querrichtung (QR) in der Rekristallisationstextur von ternären Mg-SE-Zn -Legierungen. Es wurde festgestellt, dass in den frühen Stadien der Rekristallisation ein Texturübergang von einer Waltz- zu einer Querrichtungs-dominierten Textur stattfindet. Um die Texturauswahl während der Rekristallisation zu verstehen, wurden weitere Untersuchungen zur Keimbildung und zum frühen Keimwachs-tum während der statischen Rekristallisation durchgeführt. Eine Mg-Gd-Zn-Probe im Gusszustand wurde bei 200°C einer uniaxialen Kompression bis zu 40% Dehnung unterzogen und anschließend in zwei spiegelbildliche Probenhälften geschnitten, von denen eine 60 Minuten lang geglüht wurde. Klassische und Quasi-Insitu-EBSD-Analysen belegten die Bedeutung spezifischer Keimbildungsstellen, insbesondere Druck-Zug-Doppelzwillinge, für die endgültige Textur. Quasi-Insitu-EBSD-Untersuchungen ergaben ein selektives Wachs-tum von nicht-basalen-Texturkomponenten, die letztendlich die resultierende Rekristal-lisationstextur dominieren. Die kombinierten Effekte der gelösten Legierungselemente und ihre Abhängigkeit von ihrem Ausgangsverhältnis in der Legierung wurden durch den Vergleich der Korngrenzseigerung der Legierungselemente und der

Texturbildung in drei Mg-Gd-Zn-Legierungen mit unterschiedlichen Gd:Zn-Verhältnissen, 2:1, 1;1 und 1:2, untersucht. Ein niedriges Gd:Zn-Verhältnis führte zu einer stärkeren Korngrenzseigerung der gelösten Stoffe und einer ausgeprägteren QR-Textur. In allen Legierungen wurden Cluster mit einem Verhältnis von etwa 0,33 gefunden, was darauf hindeutet, dass für die Bildung effektiver Cluster eine hohe Zn-Konzentration erforderlich ist. Diese Ergebnisse belegen, dass eher Änderungen des Elementverhältnisses als ihre absolute Konzentration Korngrenzseigerung und Texturbildung bestimmen.
Was die mechanischen Eigenschaften betrifft, zeigten Mg-Er-Zn und Mg-Gd-Zn im Vergleich zu den entsprechenden binären Legierungen, eine verbesserte Streckgrenze, die Fähigkeit zur Kaltverfestigung und eine hohe Bruchduktilität. EBSD-gestützte Gleitlinienanalyse nach 5 % Dehnung zeigte ein erhöhtes nichtbasales Gleiten in den ternären Legierungen im Vergleich zu binären Legierungen. Änderungen des Gd:Zn-Verhältnisses führen zu einer weiteren Verstärkung der Aktivierung des nichtbasalen Gleitens bei niedrig-eren Gd:Zn-Verhältnissen. Darüber hinaus wurde eine Anisotropie der Fließspannung zwischen Spannung in Waltz- (WR) und Querrichtung (QR) beobachtet, die gleichermaßen mit dem Gd:Zn-Verhältnis skaliert und auf eine verstärkte Aktivierung der Zwillingsbildung unter Belastung in TD zurückgeführt wird.
Die Ersetzbarkeit von seltenen Erden durch Ca wurde durch EBSD-Untersuchungen, Atomsondentomographie und ab initio-Berechnungen von binären und ternären Mg-Gd-(Zn)- und Mg-Ca-(Zn)-Legierungen untersucht. Die Texturuntersuchungen ergaben, dass die Mg-Ca-Legierung im Vergleich zu den SE-haltigen Legierungen eine ähnliche Ab-weichung von der Basaltextur aufweist. Allerdings wurden bei SE- und Zn-haltigen Legierungen signifikante synergistische Legierungselementeffekte beobachtet, nicht jedoch in der entsprechenden Ca-Legierung. Ab-initio-Berechnungen der Bindungsenergien ergaben eine bevorzugte Gd-Zn Bindung im Vergleich zu Ca-Zn. Zusätzlich wurde die Bindungsenergie zwischen Legierungselement und Leerstellen untersucht, um das Verhalten von Legierungselementen in Bereichen mit vielen Leerstellen, z. B. an Korngrenzen, abzuschätzen und es zeigte sich, dass Ca gegenüber Gd bevorzugt wird, was die abwei-chenden Texturtendenzen bei binärem Mg-Ca erklären könnte.
Zur Erforschung alternativer Verformungsmodi in Mg-Ca-Legierungen wurde der Synchro-Shear Mechanismus in Mg_2Ca-Laves-Phasen untersucht. Durch klassische atomistische Simulationen und ab initio Berechnungen wurde nachgewiesen, dass Synchro-Shear energetisch günstig und daher der Hauptmechanismus für die Versetzungsbewegung auf der Basalebene ist.

Abbreviations and Symbols

APT	Atom probe tomography
α	Chan-Lücke-Stüwe model constant
α'	Chan-Lücke-Stüwe model constant
b	Burgers vector
c	Concentration
c_0	Solute concentration of the alloy
Ca	Calcium
CD	Compression direction
D	Mean grain diameter
D_0	Mean grain diameter at the onset of grain growth
DTN	Deformation twin nucleation
D_t	Mean grain diameter at the annealing time t
DFT	Density functional theorem
E	Energy
EAM	Embedded atom method
EBSD	Electron back scatter scanning diffraction
Er	Erbium
G	Shear modulus
$\dot{\mathbf{G}}$	Growth rate

GB	Grain boundary
Gd	Gadolinium
γ	Specific surface energy
ΔG_{seg}	Segregation energy
HAGB	High angle grain boundary
hcp	Hexagonal closed packed
$\hat{H}$	Hamilton operator
JMAK	Jonson-Mehl-Avrami-Kolmogorov
k	Boltzmann constant
K	Kinetic growth konstant
K_0	Kinetic growth constant at 0K
LAGB	Low angle grain boundary
m	Grain boundary mobility
MEAM	Modified embedded atom method
MD	Molecular dynamics
Mg	Magnesium
$\dot{\mathbf{N}}$	Nucleation rate
n	Avrami exponent
P	Driving force
PSN	Particle stimulated nucleation
PAW	Projector augmented wave
P_c	Capillary driving force
P_{el}	Stored elastic energy driving force
P_s	Solute drag force

P_{tot}	Total driving force
ψ	Wave function
Q	Activation energy
R	Radius of curvature (also ideal gas constant)
RD	Rolling direction
ρ	Dislocation density
RE	Rare earth
SBN	Shear band nucleation
SIBM	Strain induced grain boundary migration
t	Time
T	Temperature
t_R	Recrystallization time for a recrystallized volume fraction of 0.63
TD	Transverse direction
TKD	Transmission Kikuchi diffraction
U	Interaction energy
v	Grain boundary velocity
VASP	Vienna Ab-Initio Package
X	Recrystallized volume fraction
X_{GB}	Solute concentrations at the grain boundary
X_M	Solute concentrations in the matrix
XRD	X-ray diffraction
Zn	Zinc

List of Figures

1.1 Schematic research strategy including a brief summary of used methods and findings. 5

2.1 Scheme of Atom probe tomography (APT)-tip preparation. (a) SE image of a selected grain boundary marked by a protective platinum layer. (b) Schematic image of a wedge-shaped lift out with marked slices and a side view of the Si posts with mounted and milled tips. (c) Exemplary, IPF map from TKD measurements of the APT tip during milling and SE image of a final APT tip. (d) Top view of Gd solute (marked in blue) segregation at a grain boundary measured by APT 8

3.1 (a) Typical slip planes in hexagonal crystals, e. g. Magnesium. (b) Dependence of the critical resolved shear stress τ_c from the temperature for the slip systems shown in (a) and tensile twinning, reprinted from [4]. 10

3.2 Scheme of recovery and its stages: (a) tangled dislocations; (b) Cell formation; (c) dislocation annihilation; (d) subgrain formation. Adapted from [40]. 11

3.3 Shematic curves of (a) hardness and (b) recrystallized volume fraction during recrystallization. (c) ln(-ln(1-X)) over ln(t) plot for the determination of the Avrami exponent n. 13

3.4 Illustration of the main acting driving forces during grain growth at the example of four different growth conditions. As ρ_1 is equal to ρ_3, ρ_4 and ρ_5 the force of the elastic energy gradient plays only a role in chase 2. (i) Capillary driving force (P_c). (ii) P_c and elastic energy driving force (P_{el}) acting in the same direction and the resulting driving force (P_{tot}). (iii) P_c and equally strong counteracting solute drag force (P_s). (iv) P_c and weaker counteracting P_s and the resulting P_{tot} in favor of P_c. 15

3.5 a) top: Interaction force between solutes and the grain boundary in the vicinity of the boundary. bottom: Concentration profile near the grain boundary in the case of a static and a moving boundary (dotted line). b) Evolution of the velocity with the driving pressure for different solute concentrations after the Chan-Lücke-Stüwe model. Adapted from [39]. 18
3.6 Typical textures of hexagonal materials depending on their c/a ratio. 19

5.1 Graphical abstract showing the main findings on texture selection in Mg-Er-(Zn) [57]. 26
5.2 Graphical abstract showing the main findings on selective nucleation and growth in Mg-Gd-Zn [54]. 27
5.3 Graphical abstract showing the main findings on synergistic effects in Mg-Gd-Zn [56]. 28
5.4 Graphical abstract showing the main findings on solute effects on binding, segregation and texture [55]. 29

List of Tables

2.1 Investigated binary and ternary alloys with the corresponding solute concentration in atom percentage and peer review publications 1 [57], 2 [56], 3 [54] and 4 [55]. 6

3.1 Typical slip systems in hexagonal crystals depending on the c/a ratio at the example of Zinc, Magnesium and Titanium [82]. 9

Declaration on Publications

This dissertation is based on the following research articles, of which two are available online and to be published (3,4) and three are published in international peer-reviewed journals (1,2,5) :

1. F. Z. Mouhib et al. “Texture Selection Mechanisms during Recrystallization and Grain Growth of a Magnesium-Erbium-Zinc Alloy”. In: Metals 11.1 (2021), DOI: 10.3390/met11010171.

2. F. Z. Mouhib et al. “Synergistic effects of solutes on active deformation modes, grain boundary segregation and texture evolution in Mg-Gd-Zn alloys”. In: Materials Science and Engineering: A 847 (2022), DOI: 10.1016/j.msea.2022.143348.

3. F. Z. Mouhib et al. “On the role of selective nucleation and growth to recrystallization texture development in a Mg-Gd-Zn alloy”. In Journal of Materials Science 59 (2023), DOI: https://doi.org/10.1007/s10853-023-09243-3.

4. F. Z. Mouhib et al. “Exploring solute behavior and texture selection in magnesium alloys at the atomistic level”. In Acta Materialia 266 (2024),
   DOI: https://doi.org/10.1016/j.actamat.2024.119677.

5. J. Guénolé et al. ”Basal slip in laves phases: The synchroshear dislocation” In: Scripta Materialia 166 (2019), DOI: 10.1016/j.scriptamat.2019.03.016.

Table of Contents

Acknowledgement i

Abstract i

Zusammenfassung ii

Abbreviations and Symbols vi

Liste of Figures x

Liste of Tables xi

Declaration on Publications xii

1 Motivation and Objectives 3

2 Materials and Methods 6
- 2.1 Materials . . . 6
- 2.2 Experimental Methods . . . 7
- 2.3 Computational methods (publication 5) . . . 8

3 Fundamentals 9
- 3.1 Deformation of Magnesium and its Alloys . . . 9
- 3.2 Recovery and Recrystallization . . . 11
- 3.3 Grain Growth . . . 14
- 3.4 Solute Segregation and Drag Effects . . . 16
- 3.5 The Crystallographic Texture . . . 18
- 3.6 Molecular Dynamics . . . 19
- 3.7 Ab-initio Calculations . . . 20

4 State of the Art **22**
4.1 State of the Art and current Gap of Knowledge 22

5 Key Insights and Scientific Contribution **25**
5.1 Key Insights 25
5.2 Scientific Contribution 30

6 Outlook **32**

References **32**

7 Publications **43**
7.1 Texture Selection Mechanisms during Recrystallization and Grain Growth of a Magnesium-Erbium-Zinc Alloy. 43
7.2 Synergistic Effects of Solutes on Active Deformation Modes, Grain Boundary Segregation and Texture Evolution in Mg-Gd-Zn Alloys. 58
7.3 On the role of selective nucleation and growth to recrystallization texture development in a Mg-Gd-Zn alloy 73
7.4 Exploring solute behavior and texture selection in magnesium alloys at the atomistic leve 86
7.5 Basal Slip in laves Phases: The synchroshear dislocation 95

Chapter 1

Motivation and Objectives

A growing demand for highly efficient materials, leads to the necessity of a deep knowledge of the mechanisms underlying microstructural alterations. Especially the role of solutes, their combined effects and interaction with deformation modes and intrinsic boundaries need to be rendered predictable. This knowledge would enable an advanced control over alloying concentrations and the resulting properties and is key to informed alloy design. Despite enhanced research efforts, the complexity of industrial alloy systems, as well as the multitude of physical mechanisms involving solute interactions impede a precise prediction of solute effects to the date [51, 52, 61, 74, 76].

Dilute magnesium alloys have the capacity for significant modifications of their properties depending on the chosen alloying system. Although magnesium alloys hold the potential to meet industrial requirements for weight and energy efficiency, the limited low-temperature formability of conventional magnesium alloys impedes their broad application. Amongst the common alloying elements, rare-earth elements have proven to trigger unique sheet texture alterations, as well as enable the activation of non basal slip and enhance superior mechanical properties [4, 11, 12, 16, 30, 33, 51, 58, 65, 69, 71]. However, the effective solute concentrations and their ratios necessary to enhance RE-specific material properties are yet to be determined and synergistic effects of RE and Zn are far from being fully understood. A main concern to the use of RE additions is their limited occurrence and high cost. Extensive research towards identifying viable alternatives deemed Ca a prominent candidate, given its similar atomic size, which is suspected to trigger comparable segregation behavior [20, 85]. However, given the sensitivity of distinct texture components to the solute type, further research is required.

Besides solute effects, the influence of precipitates impacts the mechanical properties. Notably, laves phases are important precipitates in Mg-Ca alloys. Within these phases, a unique basal slip mechanism, ”synchroshear”, was observed and suspected to be the main mechanism for dislocation motion on the basal plane [22, 46, 79].

This dissertation will extend the current state of knowledge by examining synergies between multiple solute species, namely Er/Gd/Ca and Zn, their interactions with defects and influence on the formation of RE induced texture components in dilute Mg-RE-Zn alloys, by using a multi-scale approach connecting solute segregation revealed by atom probe tomography (APT) to microstructural observations and the resulting macroscopic properties. Additionally, this work briefly explores the synchro shear mechanism by means of classical atomistic simulation and ab initio calculations.

The main research objectives are outlined below, with corresponding publications referenced in parentheses.

1. Estimating the potential of Er/Gd in modifying the sheet texture upon rolling and annealing (publication 1 + 2).
2. Unraveling the mechanisms for texture selection during recrystallization and grain growth and how it is connected to grain boundary motion and stability (publication 1 + 2 + 3).
3. Quantifying solute effects by estimating the required solute ratio and concentration to trigger RE induced alterations of the alloy properties (publication 2).
4. Identifying the influence of different solute species (RE and non -RE) on texture and solute segregation to clarify the texture modification potential of Ca, compared to RE additions (publication 4).
5. Establishing a basic understanding of the impact of solutes on the active slip mechanisms and the resulting mechanical properties (publication 1 + 2 + 5).

Fig. 1.1 depicts the employed research strategy for the objectives described above, showcasing the key findings and the interplay between macroscopic observations, their microscopic origin, and underlying atomic-scale mechanisms.

.

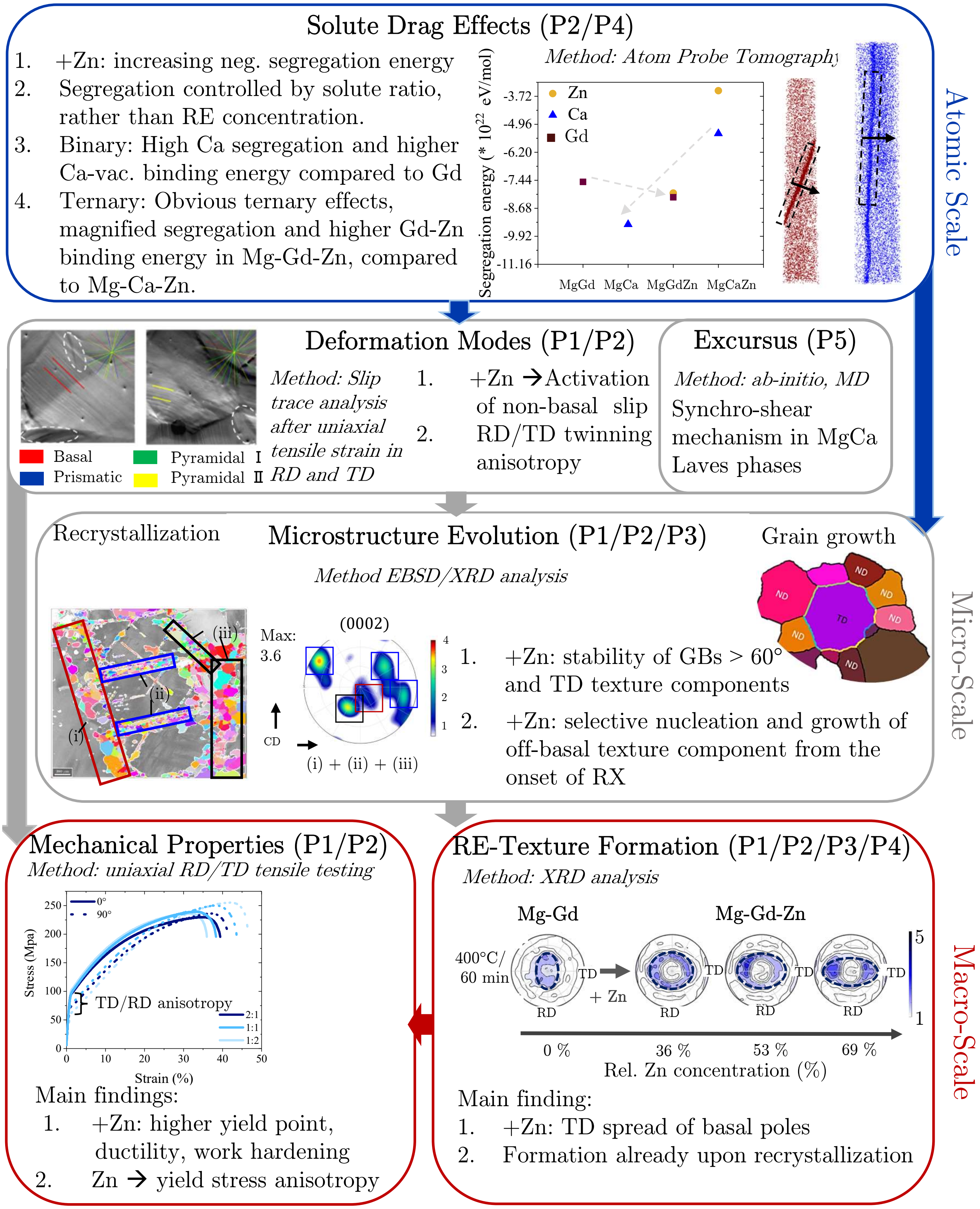

Figure 1.1: Schematic research strategy including a brief summary of used methods and findings.

Chapter 2

Materials and Methods

This chapter includes a brief overview of experimental details and investigated the materials. It includes sample preparation, electron microscopy, X-Ray diffraction, atom probe tomography, mechanical testing and computational methods.

2.1 Materials

Tab. 4.1 gives an overview of the solute concentration in atom percent of all investigated binary and ternary Mg-RE/Ca-(Zn) alloys. For a general comparison of microstructure evolution and mechanical properties of binary and ternary Mg-RE-(Zn) alloys, Mg-Er-(Zn) was used (see [57]). The influence of the atomic RE:Zn ratio was studied at the example of Mg-Gd-(Zn) 2:1, 1:1 and 1:2 (see [56]). Additionally, the segregation potential and synergistic effects of RE-Zn additions, compared to non-RE solutes was estimated by an investigation of segregation in Mg-Gd-(Zn) compared to Mg-Ca-(Zn) (see [55]).

Table 2.1: Investigated binary and ternary alloys with the corresponding solute concentration in atom percentage and peer review publications 1 [57], 2 [56], 3 [54] and 4 [55].

	Ga (at %)	Dy (at %)	Er (at %)	Ca (at %)	Zn (at %)	Paper
MgGd	0.142	-	-	-	-	2&4
MgEr	-	-	0.140	-	-	1
MgCa	-	-	-	0.152	-	4
MgGdZn 2:1	0.150	-	-	-	0.086	2
MgGdZn 1:1	0.148	-	-	-	0.165	2
MgGdZn 1:2	0.073	-	-	-	0.165	2,3&4
MgErZn	-	-	0.140	-	0.400	1
MgCaZn	-	-	-	0.152	0.400	4

The cast material was melted in an induction furnace under an Ar/CO_2 gas atmosphere and homogenized at 460° up to 960 min, subsequently the composition was measured by ICP/OES. Rolling sheets of a dimension of 60x40x40 mm^3 were hot rolled at 400° for 10 rolling passes and one additional rolling pass was performed at 200° to increase the stored deformation energy.

2.2 Experimental Methods

Samples of the dimension of 10x12x1 mm^3 were cut from the rolling sheet and annealed in an Heraeus RL200E air furnace for long annealing times and in a sand bath furnace for all annealing treatments shorter than 5 minutes. All samples were mechanically ground to the sample mid-plane and subsequently polished with diamond suspension to 0.25 μm. Samples assorted for EBSD measurements or light microscopy were additionally electro-polished. For EBSD, a Struers AC-2 solution was used at -20 C and 20 V for 120 s. In the case of light microscopy, the samples were electro-polished for 40 min in 5:3 ethanol H_3PO_3 at 2 V and etched in an acetic picral solution. XRD measurements for the characterization of the macro texture were done using a Brukers D8 advance diffractometer. Six incomplete pole figures were measured, $\{10\bar{1}0\}$, $\{0002\}$, $\{10\bar{1}1\}$, $\{10\bar{1}1\}$, $\{10\bar{1}2\}$, $\{10\bar{1}3\}$ and $\{11\bar{1}0\}$, from those, full pole figures and orientation distribution functions (ODFs) were calculated using the texture analyses toolbox MTEX [35]. EBSD measurements were done with a step size depending on the grain size and varying from 0.5 to 1.5 μm using a HKL-Nordlys II EBSD detector and a focused ion beam Helios 600i operating at 20 V. The analysis of the EBSD raw data was done using the MTEX toolbox [35]. The recrystallization kinetics was calculated from measurements of the Vickers hardness during interrupted annealing treatments at 370 °C up to 5000 s.

Atom probe tomography (APT) was performed to analyse the spatial distribution of solute elements in the vicinity of a grain boundary (see Fig. 2.1 d). For this purpose, atom probe tips were prepared by Transmission Kikuchi diffraction (TKD)-assisted tip milling. A site specific wedge-shaped region containing a grain boundary, previously marked and protected from contamination by platinum deposition, was cut free and lifted out using an Ga+ ion beam. The region of interest was sliced and mounted on Si posts and subsequently multi-step milling was performed under decreasing ion beam currents (0.43 nA to 40 pA) and tip radii (1.5 to 0.1 μm) (see Fig. 2.1 a, b). To insure the presence of grain boundary before subsequent APT measurements and to characterise the grain orientations milling was assisted by TKD (see Fig. 2.1 c). For the APT measurements, a LEAP 4000X HR Cameca Instrument equipped with an ultraviolet laser with a wavelength of 355 nm operating at -30°C was used at a constant evaporation rate of 0.5 %.

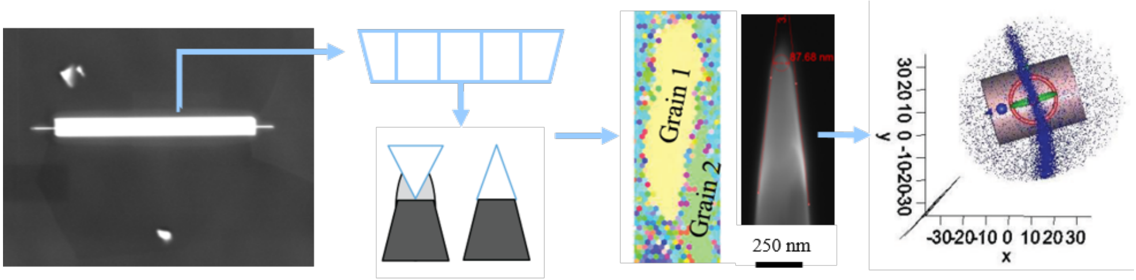

(a) (b) (c) (d)

Figure 2.1: Scheme of APT-tip preparation. (a) SE image of a selected grain boundary marked by a protective platinum layer. (b) Schematic image of a wedge-shaped lift out with marked slices and a side view of the Si posts with mounted and milled tips. (c) Exemplary, IPF map from TKD measurements of the APT tip during milling and SE image of a final APT tip. (d) Top view of Gd solute (marked in blue) segregation at a grain boundary measured by APT

Uniaxial stress-strain curves were obtained from tensile tests in rolling (RD) and transverse direction (TD) of dog-bone-shaped samples with gauge dimensions of 5 x 1.5 x 0.8 mm^3 annealed at 400°C for 3600 s using a ZWICK tension compression machine under a constant strain rate of 2x10^{-}4. Each test was done three times to ensure repeatability. The active deformation modes were determined by slip trace analysis of interrupted tensile samples strained up to 5 %. Slip lines were observed on high resolution SE images and the corresponding slip plane was determined by a comparison to the grains orientation from IPF-EBSD maps using a semi-automatic Matlab code [26].

2.3 Computational methods (publication 5)

The Vienna Ab-initio Simulation Package (VASP) with the projector augmented wave method (PAW), was used for first-principle calculations [15, 43, 44]. The electron configurations employed were 3s3p4s for Ca and 6p2s(2s1p) for Mg(Al). To determine an appropriate energy cut-off and k-mesh, a convergence analysis was carried out. A cut-off energy of 550 eV and a k-mesh of 21x21x21 were selected. For molecular dynamics calculations, the quickmin algorithm [14, 72] as implemented in LAMMPS was used. The interatomic forces were approximated using the MEAM potential developed by Kim et al. [41].

Chapter 3

Fundamentals

The following chapter serves as an overview of the relevant concepts of materials physics for the research presented in this work. It covers basic deformation modes and textures of hexagonal materials, annealing phenomena, e.g. recrystallization and grain growth, and fundamental concepts of solute boundary interactions.

3.1 Deformation of Magnesium and its Alloys

The mechanisms acting during deformation, namely the active slip systems, are crucial for the potential stress accommodation and the resulting stress state, hence the mechanical response of the material during further processing. Additionally, the deformed state is fundamental to the development of the microstructure formed during subsequent annealing, as it determines location, orientation and growth potential of the formed recrystallization nuclei. In hexagonal metals, such as Magnesium (Mg), dislocation slip occurs mainly on four slip planes, basal (0002), prismatic $(10\bar{1}0)$, pyramidal I $(10\bar{1}1)$ and pyramidal II $(11\bar{2}2)$. Except for pyramidal II, the common slip direction lies in the basal plane along the a direction $\langle 11\bar{2}0\rangle$. Contrary to slip systems along $\langle a\rangle$ direction, pyramidal II slip, $\langle 11\bar{2}3\rangle$ ($\langle c+a\rangle$), has a component in c direction [47]. These slip systems are depicted in Fig. 3.1 a.

Table 3.1: Typical slip systems in hexagonal crystals depending on the c/a ratio at the example of Zinc, Magnesium and Titanium [82].

	c/a	Principle slip system	Secondary slip system	Other slip systems
Zn	1.856	Basal	Pyramidal II	Prismatic
Mg	1.624	Basal	Prismatic	Pyramidal II + I
Ti	1.588	Prismatic	Basal	Pyramidal II + I

However, due to its low critical resolved shear stress only basal slip is activated in conventional

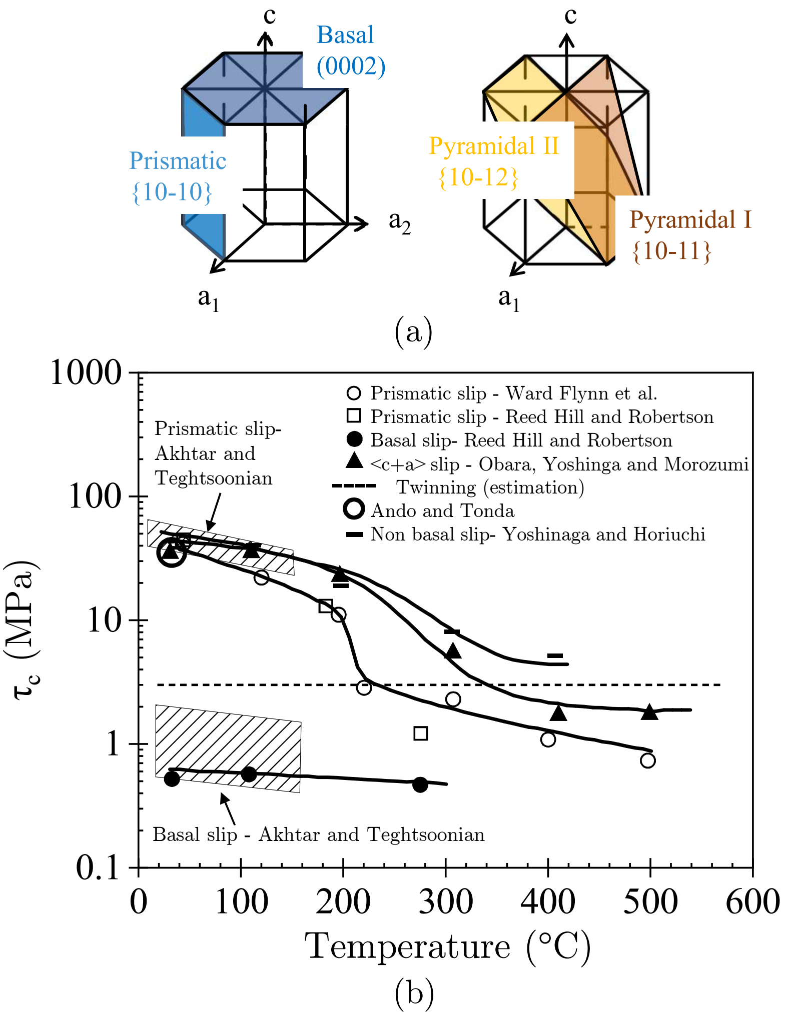

(a)

(b)

Figure 3.1: (a) Typical slip planes in hexagonal crystals, e. g. Magnesium. (b) Dependence of the critical resolved shear stress τ_c from the temperature for the slip systems shown in (a) and tensile twinning, reprinted from [4].

Magnesium and its alloys at low temperature (see Fig. 3.1 b). For hexagonal materials with a c/a ratio smaller than 1.63 non-basal slip mechanisms can be activated more easily compared to ideal hexagonal closed packed hcp material. Tab. 3.1 shows typical slip systems in hexagonal materials depending on the c/a ratio [82].

Next to basal slip, $\{10\bar{1}2\}$ $\langle\bar{1}011\rangle$, tensile twinning is one of the main deformation mechanisms in pure Mg and its alloys, due to its low critical resolved shear stress, compared to non-basal slip or compression twinning. Tensile twinning leads to a 86° rotation and compression twinning to a 56° rotation around the $\langle 10\bar{1}2\rangle$ axis. As twinning leads to a shape change, the external force direction and the crystal structure need to favour this shape change for twinning to occur. Is the c/a ratio larger than 1.73 compression, and for a c/a $<$ 1.73 tension twinning is favoured. During rolling, a common processing technique, basal slip leads to an alignment of the c- axis with the compression direction. As the available slip mechanisms at ambient temperatures are mainly limited to basal slip, a accommodation of stress along the c-axis is not possible. This causes a brittle behaviour of common magnesium alloys during forming.

Additional to classical slip systems and twinning a novel basal slip mechanism was observed in Laves phases and suspected to be the main deformation mechanism on the basal plane [22, 46, 79]. The so called ”synchroshear” is a simultaneous motion of two partial dislocations on the basal plan with burgers vectors along 1/3 $\langle 10\bar{1}0 \rangle$ resulting in a total burgers vector (b) of 1/3 $\langle 11\bar{2}0 \rangle$ [17, 32, 45].

3.2 Recovery and Recrystallization

During annealing of the deformed microstructure, two main mechanisms will determine the resulting microstructure, recovery and recrystallization. While recovery retains and restores properties of the preexisting microstructure, recrystallization describes the formation of a new microstructure. Recovery consists of the annihilation of dislocations and their arrangement into structures of lower energies. Fig. 3.2 shows a schematic illustration of the stages involved. During annealing of the deformed dislocation rich microstructure, a cell structure will be formed out of cell walls of tangled dislocations. Annihilation and ordering of dislocations into small angle grain boundaries will subsequently result in the formation of subgrains [27, 40].

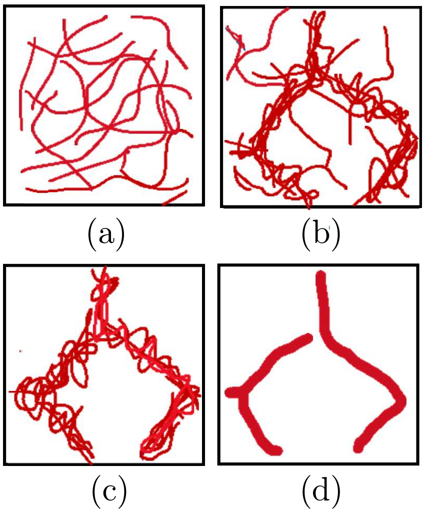

Figure 3.2: Scheme of recovery and its stages: (a) tangled dislocations; (b) Cell formation; (c) dislocation annihilation; (d) subgrain formation. Adapted from [40].

The term recrystallisation, more precisely primary recrystallisation, refers to the formation of a new microstructure by nucleation and growth of newly formed microstructural units called recrystallisation nuclei possessing high angle grain boundaries and a significantly lower elastic energy compared to the surrounding matrix. The resulting gradient in elastic energy between the nuclei and the surrounding deformed microstructure leads to a driving force (P) expressed in Eq. 3.1 enabling the growth of the recrystallised nuclei, thereby consuming the remaining deformation matrix and reducing the overall elastic energy of the microstructure. In Eq. 3.1 b represents the burgers vector of the dislocations, ρ their density and G the shear modulus.

$$P = \frac{1}{2}\rho G b^2 \tag{3.1}$$

For nucleation to occur three main criteria have to be met. The elastic energy from deformation needs to be high enough to allow a sufficient driving force for the recrystallization nuclei to grow. This is called the mechanical criterion. As the high curvature and surface energy of the nuclei will favor their shrinkage, next to a sufficient driving force they will need a minimum size allowing growth. This is referred to as the thermodynamic instability criterion. Nuclei of a viable size are expected to be preexisting in the deformed microstructure, exemplary as subgrains, contrary to classical nuclei formation by thermal fluctuations as it occurs during phase transformation. This is assumed due to the relatively low activation energy for recrystallisation and the high surface energy of high angle grain boundaries (HAGBs) [40]. Finally, the kinetic instability criterion states that, the boundaries of the nuclei have to be mobile which is only the case for high angle grain boundaries.

Nucleation at existing HAGBs, inhomogenities or particles is therefore favorable [27]. After the current state of the art, it is evident that the nuclei orientations are already existent in the deformed matrix. They depend on the nucleation sites, which are crucial for the subsequent annealing texture. Preexisting subgrains at grain boundaries may arise from strain induced grain boundary migration (SIBM), during which grain boundary bulging leads to a region with reduced dislocation density behind the grain boundary. At other nucleation sites HAGBs are formed by rapid recovery. This process requires orientation gradients in the deformed matrix making areas around particles or deformation inhomogenities, such as shear bands, ideal nucleation sites [40].

The recrystallization kinetics can be approximated by a theory developed by Johnson, Mehl, Avrami and Kolmogorov [2, 3, 27, 40] assuming randomly distributed nucleation sites. After the Jonson-Mehl-Avrami-Kolmogorov (JMAK) equation, where $\dot{\text{N}}$ represents the nucleation and $\dot{\text{G}}$ the growth rate, q represents a time constant and t_R the recrystallization time, the recrystallized volume fraction as a function of time t can be expressed (see Eq. 3.2). At t_R, X is defined to be equal to 0.63.

$$X_t = 1 - exp\left(-\frac{\pi}{3}\dot{N}\dot{G}^3 t^n\right) = 1 - exp\left[-\left(\frac{t}{t_R}\right)^q\right] \tag{3.2}$$

Under the assumption that grains grow isotropic into the matrix without contact to each other and nucleation occurs homogeneously, the Avrami exponent n is expected to be 4. In the case of site saturated nucleation, during which nucleation occurs rapidly at the start of recrystallization, the Avrami exponent will be 3.

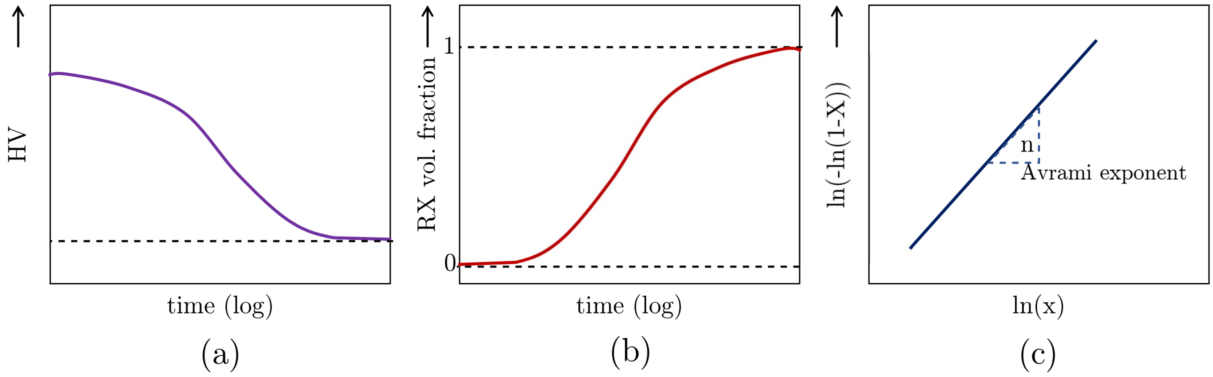

Figure 3.3: Shematic curves of (a) hardness and (b) recrystallized volume fraction during recrystallization. (c) ln(-ln(1-X)) over ln(t) plot for the determination of the Avrami exponent n.

Experimentally, the recrystallized volume fraction can be determined from interrupted hardness measurements during annealing, since due to the decreasing dislocation density the hardness is gradually decreasing until a fully recrystallized state it reached. Fig. 3.3 (a) shows a schematic development of hardness and (b) of the recrystallized volume fraction with proceeding annealing time. The slope of an ln(-ln(1-X)) over ln(t) plot, schematically shown in Fig. 3.3 (c), represents the Avrami exponent n, and can be used to compare the experimental results to theoretical expectations. The expected value of 4 or even 3 are rarely met, as the model assumptions do not fully mimic the conditions in real materials, such as anisotropic growth and site specific nucleation [27, 40].

Although recrystallization nuclei originate probably from subgrains formed during recovery, recovery will reduce the driving force for recrystallization as it lowers the overall stored elastic energy. Recrystallization and recovery are therefore competing mechanisms and their extend depends on the materials properties, e. g. the stacking fault energy, as well as processing parameters such as the annealing temperature [40]. As recrystallization requires prior nucleation it needs an incubation time, while recovery occurs thermally activated and spontaneous. Hence the extent of initial and ongoing recovery can hinder recrystallization, but once recrystallization proceeds recovery will be limited.

3.3 Grain Growth

Grain size evolution will impact the resulting texture and the mechanical properties, exemplary by anisotropic growth of specific orientations. Additionally grain boundaries act as important obstacle for dislocations. Grain growth occurs via the motion of grain boundaries, which depends on the processing temperature and time, as well as diverse intrinsic influences, such as dislocation densities, solute segregation and grain boundary characteristics [39, 40].

A simplified definition of the velocity v of a grain boundary states, that it is proportional to the total pressure on the boundary from its driving forces by its mobility m, which is considered to be a temperature dependant constant [39]. In the corresponding equation (Eq. 3.3), $\sum_{i=0}^{n} P_i$ denotes the sum of all acting driving forces.

$$v = m \cdot \sum_{i=0}^{n} P_i \tag{3.3}$$

The most important driving force is the capillary driving force (P_c), after which a boundary will move towards the center of its curvature. This is expressed in Eq. 3.4, where R is the radius of curvature and γ the specific surface energy. Statistical observations show that large grains surrounded by smaller neighbors will mostly have concave boundaries, while small grains will have a limited number of neighbors and accordingly convex boundaries. Therefore the capillary driving force will lead to a growth advantage of large grains [37, 39].

$$P = \frac{2\gamma}{R} \tag{3.4}$$

An additional driving force results from an uneven distribution of retained elastic energy from deformation(P_{el}), which will lead to a motion of the boundary towards regions with higher dislocation densities (see Eq. 3.1). Thereby, grains with a lower dislocation density consume their neighbors and the overall elastic energy is reduced. Next to curvature and elastic energy gradients, other factors can influence grain growth. Exemplary, precipitates or solute atoms inhibit grain growth and exert a force opposed to the boundaries motion. Fig. 3.4 shows four exemplary growth conditions illustrating the interaction of different driving forces and the resulting force on the boundary. The dislocation densities ρ_1, ρ_3, ρ_4 and ρ_5 are equal. Hence, the corresponding sample cases will not be effected by a gradient of the elastic energy. Case (i) shows uniquely the capillary driving force, (ii) shows both capillary and elastic energy driving force acting in the same direction and therefore accelerating the shrinkage of the small convex grain and case (iii) and (iv) include a solute drag force (P_s) counteracting to the capillary driving force. However in (iii) the solute drag force has the same magnitude as the capillary driving force preventing the boundaries motion, while in (iv) the solute drag force is smaller and will therefore only reduce the resulting driving force, but not alter its direction.

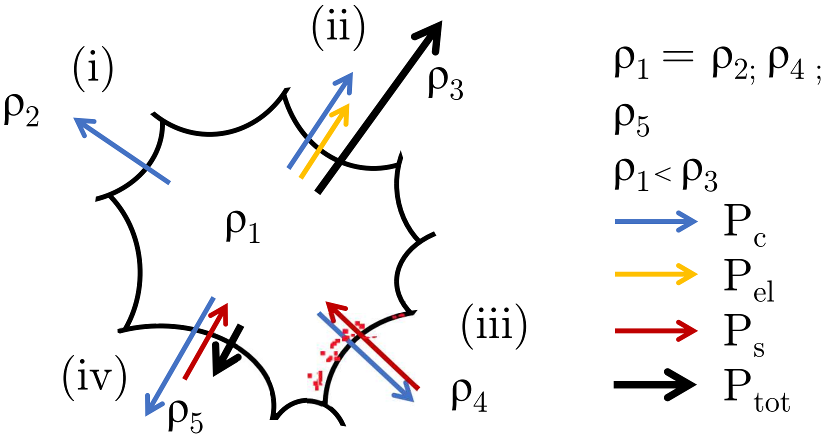

Figure 3.4: Illustration of the main acting driving forces during grain growth at the example of four different growth conditions. As ρ_1 is equal to ρ_3, ρ_4 and ρ_5 the force of the elastic energy gradient plays only a role in chase 2. (i) Capillary driving force (P_c). (ii) P_c and elastic energy driving force (P_{el}) acting in the same direction and the resulting driving force (P_{tot}). (iii) P_c and equally strong counteracting solute drag force (P_s). (iv) P_c and weaker counteracting P_s and the resulting P_{tot} in favor of P_c.

In general grain growth occurs during annealing as the involved mechanisms require thermal activation. The evolution of the mean grain diameter D can be expressed by Eq. 3.5. Here, D_0 denotes the initial grain diameter and D_t the mean diameter at a given time t. The kinetic growth constant K is temperature dependent and can be described by a simple Arrhenius expression,where Q is the activation energy for grain growth, k the Boltzmann constant, T the temperature and K_0 the kinetic growth constant at 0 K. (see Eq. 3.6).

$$D_0^2 - D_t^2 = Kt \tag{3.5}$$

$$K = K_0 \cdot exp\left(\frac{Q}{kT}\right) \tag{3.6}$$

Next to a continuous increase of the mean grain diameter, grain growth can proceed discontinuously. This phenomena is called abnormal grain growth or secondary recrystallization and is characterized by the excessive growth of a few grains possessing a growth advantage over there neighbors. Previous works, amongst others by Hillert [37] show that abnormal grain growth will occur when normal grain growth is inhibited or selective grains show a substantial growth advantage. A simple size advantage will not lead to effective abnormal growth, as the capillary driving force decreases continuously while the diameter increases.

Typically abnormal grain growth can occur in the presence of particles inhibiting normal grain growth. However, normal grain growth can also be inhibited by a strong texture annealed at high temperatures, as several works on the cube texture in various materials show [21, 62]. A strong texture leads to homogeneous orientations and low misorientations between neighboring grains, hence lower grain boundary energies and mobility. In this environment few grains with a different orientation would have grain boundaries with a high misorientation and mobility. Accordingly, a growth advantage over there neighbors.

As the impact of solute atoms on the evolution of the microstructure is a central part of this dissertation, solute segregation and the resulting drag force will be discussed detailed in the following.

3.4 Solute Segregation and Drag Effects

The effect of solutes on grain boundary migration depends on several influence factors, such as temperature, solubility, diffusivity and the grain boundary character. Solute atoms are expected to have a different energy in the vicinity of a grain boundary compared to solutes within the matrix, as the free volume and degree of order changes significantly at the grain boundary. Solute atoms larger than the matrix atoms are therefore expected to segregate to the grain boundary as they create a positive misfit energy within the matrix. Hence, by segregation of those solutes to the grain boundary the total energy is reduced. The tendency to segregate can be quantified by an empiric approach shown in Eq. 3.7 [53]. Where X_{GB} and X_M represent the solute concentrations at the grain boundary and in the matrix, respectively, R the ideal gas constant, T the temperature and ΔG_{seg} the segregation energy.

$$\frac{X_{GB}}{1-X_{GB}} = \left(\frac{X_M}{1-X_M}\right) \cdot exp\left(\frac{\Delta G_{seg}}{RT}\right) \tag{3.7}$$

A simplified but well established theory to describe solute boundary interactions is the Chan-Lücke-Stüwe model [48]. In general it can be noted that, there is a force between the solutes and the boundary, leading to an increase or decrease of the solute concentration at the boundary compared to the matrix. Eq. 3.8 shows the dependence of the solute concentration c at the grain boundary for a static boundary from the interaction energy U and the temperature T, while k is the Boltzmann constant and c_0 the solute concentration of the alloy [36, 40].

$$c = c_0 \cdot exp\left(-\frac{U}{kT}\right) \tag{3.8}$$

A moving grain boundary will leave the solute atoms behind creating an asymmetric concentration profile and a drag force between the solutes and the grain boundary, inhibiting the boundaries motion. Fig. 3.5 (a) shows the interaction force around the grain boundary as well as the resulting concentration profile for a static, as well as a moving grain boundary. At low velocities the drag force will have a strong impact on the boundaries motion, while at high velocities the grain boundary is able to break free from its solute atmosphere and moves with a mobility nearly unaffected by solutes. Eq. 3.9 shows the driving pressure P at the velocity regimes describes above. Where v denotes the velocity, m the mobility of a solute free grain boundary and c_0 the solute concentration in the alloy, while α and α' are model constants. It has to be noted that due to the simplifications made, the model is quantitatively not reliable. Exemplary, the diffusivity at the grain boundary and inside the matrix is assumed to be equal, which leads to an over estimation of the drag force. Additionally the solute-boundary interactions at intermediate velocities are not predictable due to the complexity of influence factors.

$$\begin{aligned} \text{low v regime (i)} : P &= \frac{v}{m} + \alpha c_0 v \\ \text{high v regime (i)} : P &= \frac{v}{m} + \frac{c_0}{\alpha' v} \\ \text{(i) + (ii)} : P &= \frac{v}{m} + \frac{\alpha' c_0 v}{1 + \alpha\alpha' v^2} \end{aligned} \tag{3.9}$$

However, the presented approach can be used to describe the behaviour of a boundary effected by solutes. The models predictions are illustrated in Fig. 3.5 (b). For a solute free grain boundary the velocity and the driving pressure are expected to be proportional (see Ch. 3.3), at low solute concentration this is only mildly changed towards lower velocities at higher driving pressures. In the low velocity regime, driving pressure and velocity remain proportional but the motion is inhibited. But, in an intermediate velocity range, a solute concentration large enough for a significant drag force will lead to discontinuous velocity jumps, caused by a break free of the boundary from its solute atmosphere. Accordingly, at a high velocity the boundary moves free from its solute atmosphere showing the same proportionality as a grain boundary in a pure system.

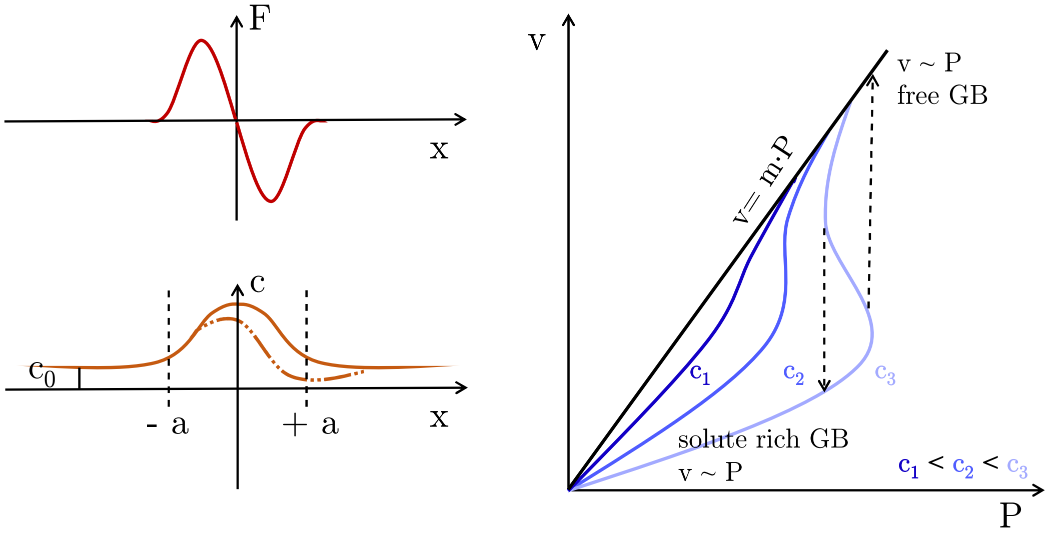

(a) (b)

Figure 3.5: a) top: Interaction force between solutes and the grain boundary in the vicinity of the boundary. bottom: Concentration profile near the grain boundary in the case of a static and a moving boundary (dotted line). b) Evolution of the velocity with the driving pressure for different solute concentrations after the Chan-Lücke-Stüwe model. Adapted from [39].

The concepts presented above approximate the behaviour of a solute loaded grain boundary. However, to grasp the complexity of the problem multiple factors have to be considered, such as ordering effects at the boundary and in its vicinity, different binding energies between solvent and solutes, varying solubility at the grain boundary and in the matrix, as well as ternary effects of multiple solute species.

3.5 The Crystallographic Texture

Most materials, including Mg, develop preferential orientations in the deformed matrix depending on the active slip mechanisms. The sum of all occurring orientations is called texture. The resulting deformation texture will influence the orientation of nuclei and therefore the final texture of the material subsequent to annealing. A strong texture can lead to anisotropic material properties, e. g. electric, magnetic and mechanical properties [1]. Texture is mostly represented by pole figures, which show an orientation density distribution of all orientations on the area of interest. A pole figure is equal to a sum of stereographic projections of multiple grains, but only one crystal plane. It relates the crystal coordinate system to global sample coordinates, such as the rolling, transverse direction and the sheet normal. The density of a specific orientation on the pole figure is usually expressed by an intensity on a scale from 1, where 1 expresses a random occurrence of the orientation.

In hexagonal materials the deformation texture depends strongly on the activated slip system which will depend on the c/a ratio of the material. Fig. 3.6 shows schematic 0002-pole figures of hexagonal materials depending on the c/a ratio.

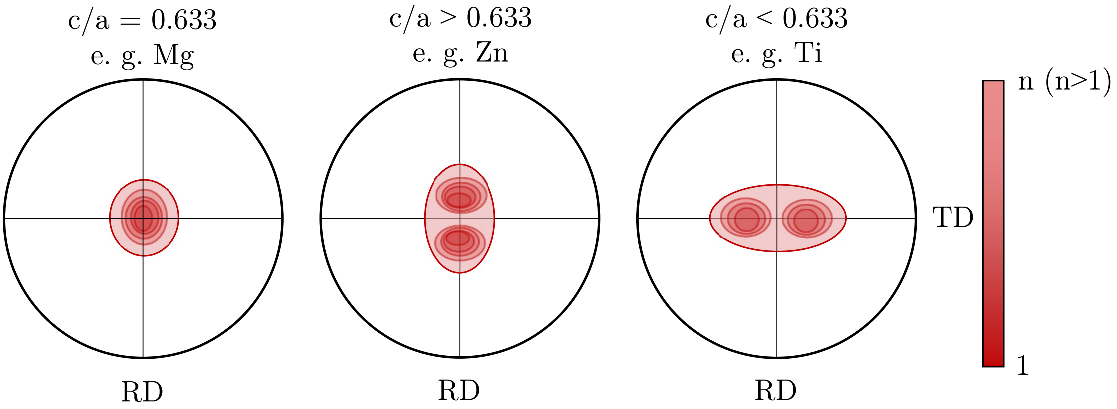

Figure 3.6: Typical textures of hexagonal materials depending on their c/a ratio.

As mentioned above in the case of Magnesium, as well as all hexagonal metals with a c/a ratio close to the ideal of the hexagonal close-packed (hcp) structure of 1.633, basal slip is the main slip mechanism. This leads to an alignment of the basal poles with the sheet normal. For smaller values of c/a, as in titanium, the basal poles will be rotated towards the transverse direction (TD) and in the case of a larger c/a ratio, as in zinc, the basal poles will be rotated towards the rolling direction (RD). The latter is a result of a combined occurrence of basal slip and twinning [78, 82]. Subsequent annealing will lead to a recrystallization texture linked to the one formed during deformation. As discussed in Ch. 3.2, the orientation of the recrystallization nuclei will depend on the deformation texture. The nucleation texture will therefore depend on the orientation of prominent nucleation sites and there expansion into the deformed matrix. However, several other influence factors effecting nuclei growth can lead to a change in texture during recrystallization. Selective growth of specific texture components by an uneven distribution of stored elastic energy, grain boundary mobility or solute and particle drag effects, can lead to significant changes of the recrystallization texture compared to the deformation texture [82].

3.6 Molecular Dynamics

Molecular dynamics (MD) uses classical mechanics to calculate the motion of particles in a system, obtaining atom positions and velocities by numerically solving Newton's laws of motion. Here, the forces between particles are the gradient of the potential energy function. An appropriate potential is chosen according to the bond type. For metallic systems mostly the embedded atom potentials (EAM) and the modified EAM (MEAM) are used. The EAM potential considers an embedding energy next to a pairwise interaction energy [18, 73]. MEAM potentials additionally include angular forces [9]. To obtain the total energy of one atom all neighbors in a certain cutt-off are considered and stored in a neighbor list. To reduce computational efforts, this list is only renewed once the atom exceeds a predefined distance of motion. To solve Newtons law of motion, implicit methods, the Verlet or the Velocity Algorithm are used [80]. While the Verlet Algortim has a lower error compared to the Velocity Verlet Algorithm, it does not provide velocities.

3.7 Ab-initio Calculations

First principles calculations are employed to derive material properties based on interactions between electrons and atom cores. These calculations are rooted in the principles of quantum mechanics, which acknowledge the wave-particle duality of quantum-scale particles. Due to this wave character, the exact position of the particles cannot be determined, but their position probabilities can be known. The states of quantum mechanical systems are described by the time-independent Schrödinger equation (see Eq. 2.3) [70], where the Hamilton operator $\hat{H}$ represents all possible energy states of the system, ψ the wave function and E the the energy.

$$\hat{H}\psi = E\psi \tag{3.10}$$

To simplify the Schrödinger equation, the Born-Oppenheimer approximation is employed [60]. In this approximation, the nuclei move much slower than the electrons, allowing their kinetics to be decoupled. The numerical cost of solving the Schrödinger equation, even with the Born-Oppenheimer approximation, scales with $(n^3)^{Ne}$, where n represents the number of mesh points, and Ne the number of electrons. Consequently, for complex or large systems directly solving the Schrödinger equation is infeasible due to the substantial computational demands. To address this limitation, Density Functional Theorem DFT is used. It replaces the wave functions with an electron density, significantly reducing the computational complexity. DFT considers only the ground state energy, which results from minimizing the Schrödinger equation. The only unknown variable is the Hohnberg-Kohn functional, which describes the quantum mechanical correlation between electrons. This functional is estimate by the iterative Kohn-Sham approach [42]. Still calculations including all electrons would demand unreasonably high computational efforts. Therefore, the electron density of electrons near the core is approximated by pseudo-potentials [38]. Common tools to perform quantum mechanical calculations are exemplary the Vienna Ab-Initio Package (VASP) [43, 44] or Quantum ESPRESSO [24, 25], they use pseudopotential obtained by the projector augmented wave (PAW) method [15].

Chapter 4

State of the Art

This chapter will clarify the current gap of knowledge and summarize the state of research on magnesium rare earth alloys relevant to the main research questions of this dissertation.

4.1 State of the Art and current Gap of Knowledge

As of late, tailoring materials properties by controlled solute additions has become crucial for a broad application of light weight materials, such as Magnesium. A prediction of the impact of solutes on deformation modes and microstructure evolution is the key to informed design of next generation magnesium alloys. In this regard, increasing research efforts have been employed to deepen the understanding of solute-defect interactions [52, 61, 76].

Currently, the application of Magnesium alloys in lightweighting is hindered by a lack of formability. This is caused by the limited activation of non-basal slip systems at room temperature and the resulting formation of a strong basal texture [23, 77]. As an increase of the processing temperature would lead to high production costs, research aims at developing materials with a weak texture and/or multiple active slip systems at lower temperatures. Although modern processing routes can lead to more prominent properties [59], the most promising approach to texture modification was found to be micro-alloying [30, 31, 65]. Common Magnesium alloys, such as AZ31, have fare superior properties compared to pure Magnesium and are therefore suitable for certain applications. However, they still develop a strong basal texture, as well as a generally low formability [5, 75]. In this context, the addition of RE elements to industrial Mg alloys, e.g. AZWX, was found to lead to enhanced texture softening and superior mechanical properties [30, 65].

Although several alloy systems have been investigated, the fundamental physical mechanisms causing property alterations remain unclear. To the date research focused mainly on two aspects, the alteration of texture by combined solute effects and the influence of solutes on active deformation modes. There is evidence that RE solutes impact both, texture and deformation modes significantly and thereby modify the resulting alloy properties. A softer texture is already formed upon rolling and enhanced during subsequent annealing. At the completion of recrystallization the texture has a clear off-basal trend and a low intensity [10, 12, 30, 57, 65, 84]. Various mechanisms triggering random nucleation, such as particle stimulated nucleation (PSN), shear band nucleation (SBN) and deformation twin nucleation (DTN) have been suspected to be the source of the RE-texture [63]. Although, those mechanisms were partially observed in RE containing alloys, texture softening was also found to occur in dilute alloys and to occur independent of any specific nucleation mechanism [10, 12, 57]. Furthermore, many RE free alloys benefit from random nucleation caused by the mentioned mechanisms without developing RE texture components [5, 50].

It is well known that RE solutes will segregate to grain boundaries due to there large size misfit within the Mg matrix. Accordingly, RE-solutes will significantly influence grain boundary mobility and energy during recrystallization and grain growth and thereby alter texture and microstructure evolution. Barrett et al. suggested that a homogenization of the grain boundary energy caused by solute segregation, leads to a reduction of the mobility of highly mobile grain boundaries, thereby annihilating the growth advantage of basal texture components. This may enable the growth of off-basal texture components weakening the typical basal texture in Mg-RE alloys [7, 8]. A specific feature of the RE-texture is a basal pole spread towards TD upon annealing, this was found to be significantly enhanced by the addition of Zn [33, 56, 71].

It is suspected that the negative size misfit of Zn in the Mg matrix will lead to clustering with RE atoms and subsequent co-segregation [8, 34, 64, 74]. Here, the magnified total solute concentration could be more efficient in terms of hindering the grain boundary motion. Synergistic effects in Mg-Gd-Zn alloys and thereby the resulting solute segregation were found to depend not only on the amount but also on the relative ratio of solutes in the material [56]. Additionally, it was proposed that synergistic effects could alter the grain boundary energy and or structure and thereby favor the observed texture formation [51, 56, 58]. In this regard, a recent ab-initio study by Mahjoub at. al showed a dependence of the binding energy between RE solutes and Mg atoms from the grain boundary character [51]. The observed anisotropic binning energy may lead to anisotropic mobility and thereby influence the growth of specific texture components. Next to anisotropic solute boundary interactions, segregation itself might be anisotropic. This was recently observed in Mg-Mn-Nd [61] and other material systems (e. g. (Pt-Au) [6]). Accordingly, a growth advantage of specific grain boundaries and thereby TD-texture components, is currently assumed to be caused by complex solute-boundary interactions possibly modifying the grain boundary energy and mobility.

Additionally, RE elements were found to impact the mechanical properties significantly. A higher yield and ultimate tensile strength are observed, as well as an enhanced formability [11, 57, 63]. The current literature attributes this to a combination of the texture modifications described above and immediate solute effects on the active deformation modes. The activation of non-basal slip, including pyramidal II $< c+a >$ slip, was frequently observed in Mg-RE alloys [20–23] and in combination with Zn the activation of non-basal slip was further enhanced [17,24]. In Mg-Y, the activation of $< c+a >$ slip was explained by changes in the stacking fault energies after small additions of Y [68, 86]. Several studies attribute enhanced non-basal slip to basal slip strengthening caused by the inhibition of basal slip by solute pinning in Mg-RE alloys [66, 67, 83].

The addition of Zn further enhances the observed RE effects on the mechanical response [4, 11, 65, 71]. The activation of non basal slip modes was also promoted by Zn additions, indicating the importance of synergistic effects on mobile dislocations and thereby on slip activation [56]. Additionally, Zn in combination with RE solutes, leads to a yield stress anisotropy in rolling sheets depending on the testing direction exhibiting lower yield stresses under strain in transverse direction (TD) [19, 29, 56]. Several studies observed not only an anisotropy of the mechanical properties but additionally an anisotropy in tensile twin activation [19, 29, 56]. The properties and stability of tensile twins, a mechanism crucial for local strain accommodation in Mg alloys, were also found to be effected by combined RE and Zn segregation to twin boundaries [13, 49, 58, 81]. Namely, an enhanced activation of tensile twinning in ternary Mg-RE-Zn alloys was observed (e. g. by Luo et. al [49]). Nie et al. showed that the Gd and Zn solutes at twin boundaries alter their properties effecting twin activation and stability [58].

Nevertheless, a significant obstacle to the industrial application of RE solutes is their limited availability and high cost. Extensive research efforts have been employed to find viable alternatives, considering both texture and properties. Calcium (Ca) emerges as a prominent candidate due to its similar atomic size, suggesting potential parallels in solute segregation and resulting microstructural alterations. Indeed, comparable texture components and enhanced mechanical performance have been observed [20, 85]. However, despite these observations, the topic remains ambiguous, particularly in ternary alloys containing Zn, as texture trends show a high sensitivity to the solute type.

The available literature reveals the importance of synergistic solute effects on the activation of non-basal deformation modes, including twinning, as well as solute segregation to grain boundaries, texture selection and the resulting materials properties.

Chapter 5

Key Insights and Scientific Contribution

The following will summarize the main investigations and findings of this dissertation, and elaborate its scientific contribution to the ongoing research in the field.

5.1 Key Insights

As solute effects were proven crucial to the development of high performance magnesium alloys, attaining a deep understanding of solute interactions is the key to targeted alloy design. Undertaking this pursuit, this dissertation aimed at unraveling the origin of specific texture components and mechanical properties in ternary Mg-RE-Zn alloys, with regard to solute-grain boundary interactions and resulting synergistic solute effects. A multi-scale approach featuring classical EBSD analysis, mechanical testing, atom probe tomography and ab initio calculations was employed to trace back microstructural features to the effect of solutes on grain boundaries and slip activation.

Texture selection during recrystallization and following grain growth was investigated for Mg-Gd-(Zn) and Mg-Gd-(Zn) alloy systems (publication 1+2). To assess their dependence on solute ratios, three Mg-Gd-Zn alloys with varying Gd:Zn ratios of 2:1, 1;1 and 1:2 were examined (publication 2). The investigation of texture selection during recrystallization was performed by uniaxial compression, subsequent heat treatments and quasi-in-situ EBSD analysis, proving both selective growth of off-basal texture components and the importance of specific nucleation sites to the final texture (publication 3). Unique synergistic solute effects were identified between Zn and RE compared to none RE solutes, by a combined approach of atom probe tomography and ab initio calculations of Mg-Ca-(Zn) and Mg-Gd-(Zn) (publication 4). Synchro shear in C14 and C15 Mg_2Ca laves phases was investigated by classical atomistic simulation and ab initio calculations (publication 5).

The main findings of these investigations reveal a significant impact of solute-solute and solute-boundary interactions on texture formation and mechanical properties. They are summarized in 5 research articles, that effectively fulfill the set research objectives.

1. Estimating the potential of Er/Gd in modifying the sheet texture upon rolling and annealing (publication 1+2).

The synergy of Zn and RE within dilute Mg-RE-Zn alloys was proven to be effective for sheet texture modifications during annealing. A distinctive texture characterized by pronounced basal pole peaks around ±40° TD was observed in both, ternary Mg-Gd-Zn and Mg-Er-Zn, while the corresponding binary alloys maintained a predominant RD spread from their rolling texture. Both Mg-Gd-Zn and Mg-Er-Zn, exhibited selective growth during recrystallization and subsequent grain growth favoring, TD-tilted texture components. Synergistic effects were found to be crucial in terms of providing TD orientated recrystallization nuclei, as binary alloys lacked distinct TD texture tendencies (see Fig. 5.1 and 5.3) [56, 57].

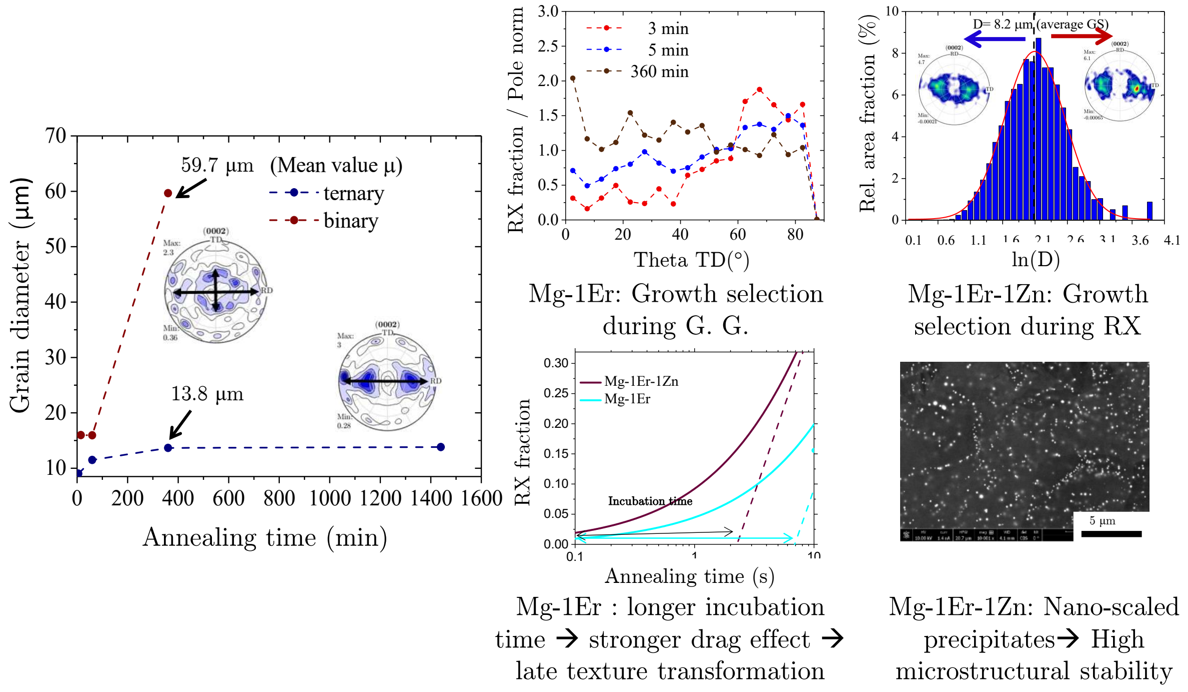

Mg-1Er: Growth selection during G. G.

Mg-1Er-1Zn: Growth selection during RX

Mg-1Er : longer incubation time → stronger drag effect → late texture transformation

Mg-1Er-1Zn: Nano-scaled precipitates→ High microstructural stability

Figure 5.1: Graphical abstract showing the main findings on texture selection in Mg-Er-(Zn) [57].

2. Unraveling the mechanisms for texture selection during recrystallization and grain growth and how it is connected to grain boundary motion and stability (publication 1 + 2 + 3).

In both investigated ternary alloy systems, Mg-Er-Zn and Mg-Gd-Zn, recrystallization nuclei demonstrated selective growth behavior favoring TD-tilted texture components. This phenomena likely originates from anisotropic solute-boundary interactions affecting the mobility during the early stages of nuclei growth. The addition of Zn led to a notable transition in grain boundary misorientation angle distribution, shifting from predominant angles of 40° in binary alloys to angles exceeding 60° in ternary alloys. Hence, synergistic effects were proven evident in Mg-RE-Zn alloys (see Fig. 5.1 and 5.3) [56, 57]. A comparative EBSD study of two halves of one sample subjected to compression, one as deformed and the other post-annealing, revealed that static recrystallization was closely linked to specific nucleation sites within the deformation microstructure. In that respect, double twins were found to be important nucleation sites providing viable orientation components for the resulting recrystallization texture. Quasi-insitu observations provided insights into growth selection of off-basal nuclei while neighboring basal nuclei diminished, leading to an off-basal recrystallization texture (see Fig. 5.2) [54].

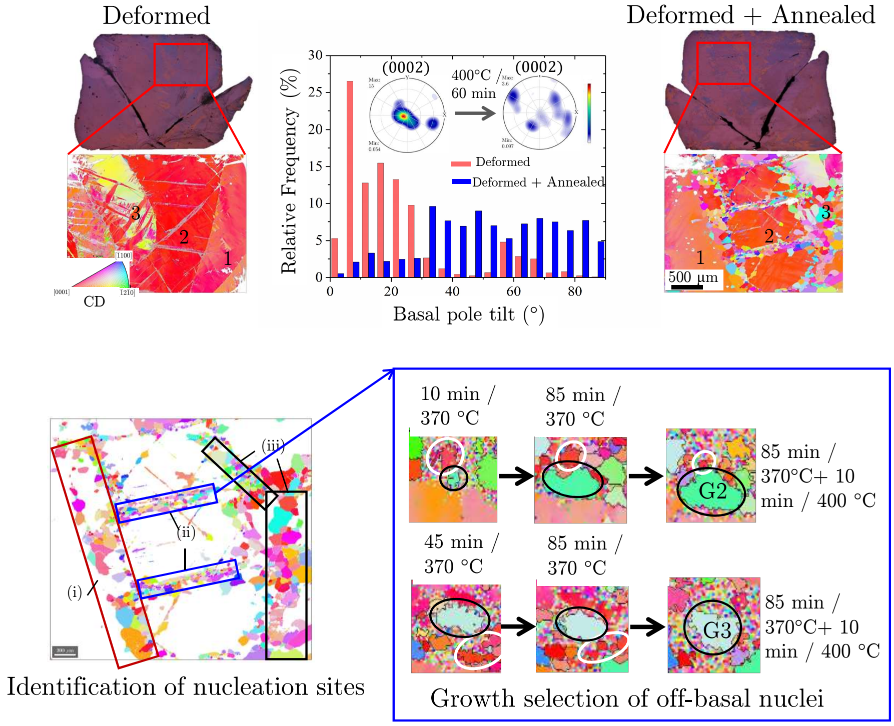

Figure 5.2: Graphical abstract showing the main findings on selective nucleation and growth in Mg-Gd-Zn [54].

3. Quantifying solute effects by estimating the required solute ratio and concentration to trigger RE induced alterations of the alloy properties (publication 2)

Classical EBSD and atom probe tomography were applied to three Mg-Gd-Zn alloys with distinct Gd:Zn ratios (2:1, 1:1, and 1:2), exploring the sensitivity of synergistic effects to alloy composition variations. In Mg-Gd-Zn, notable trends were observed: As the Gd:Zn ratio decreased the basal pole spread towards the transverse direction became more pronounced. Additionally, the negative segregation energy, as well as the peak concentration at the grain boundary increased. Thus, alterations of the solute ratio rather than the absolute solute concentration were found to govern solute segregation and synergistic effects. Identified solute clusters in the matrix consistently exhibited a Gd:Zn ratio of approximately 0.33, irrespective of the Gd:Zn ratios in the original alloy compositions. Hence, the formation of stable clusters effective for grain boundary co-segregation is likely to be linked to a high Zn concentration, potentially explaining augmented segregation in alloys with a lower Gd:Zn ratio (see Fig. 5.3) [56].

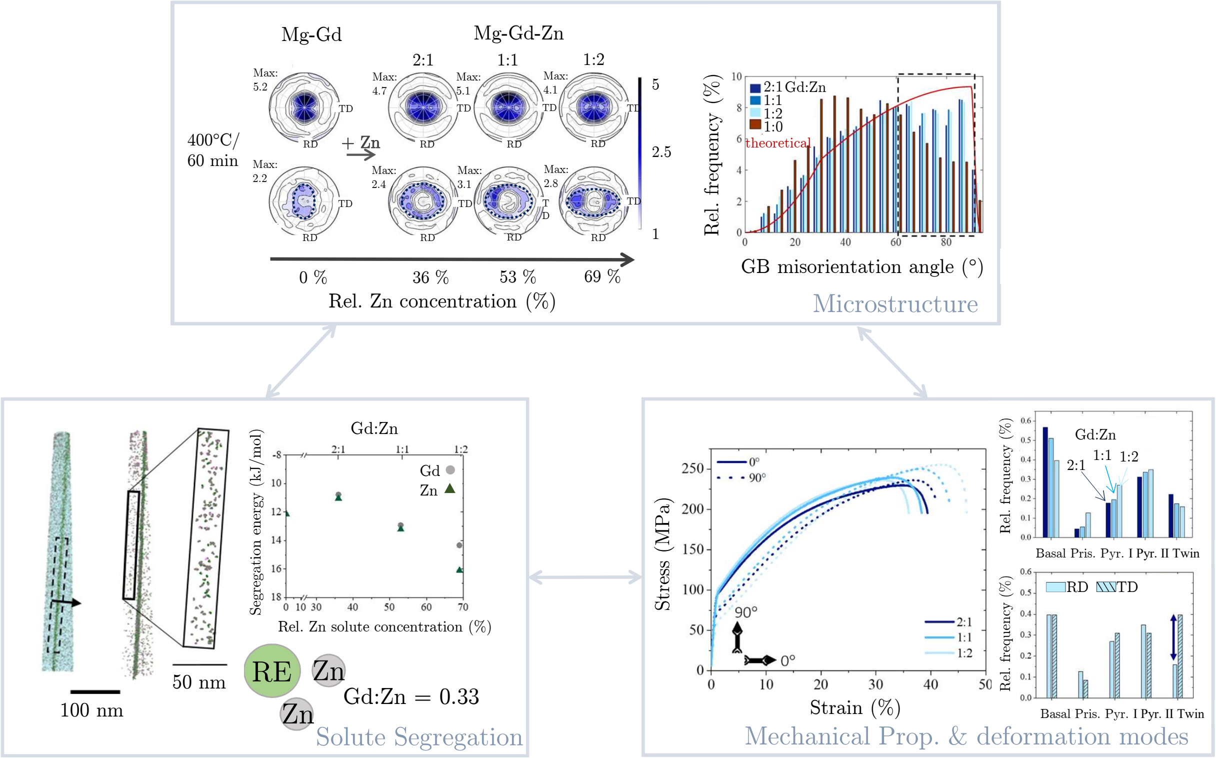

Figure 5.3: Graphical abstract showing the main findings on synergistic effects in Mg-Gd-Zn [56].

4. Identifying the influence of different solute species (RE and non RE) on texture and solute segregation to clarify the texture modification potential of Ca, compared to RE additions (publication 4).

The texture of binary Mg-Ca displayed a pole spread in both RD and TD, in contrast to Mg-Gd, where a pronounced RD split was evident, but no significant TD texture component was observed. Furthermore, ternary Mg-Gd-Zn exhibited a significant TD pole spread, while in the corresponding Ca ternary alloy, Zn additions only led to small texture alterations. Atom probe tomography revealed complementary trends in segregation. Within the binary systems, Ca segregation exceeded that of Gd. The addition of Zn did not notably affect the segregation of Ca, and Zn itself exhibited week segregation tendencies. However, in ternary Gd based alloys, Zn significantly enhanced the segregation of Gd, alongside an intensified Zn segregation. Ab initio calculations revealed higher binding energies between Ca and vacancies compared to Gd, indicating a preference for Ca rather than Gd segregation to defect-rich regions, e.g., grain boundaries, in binary alloys. Nevertheless, significant ternary effects were observed in Mg-Gd-Zn compared to Mg-Ca-Zn, attributed to more favorable Gd-Zn binding compared to Ca-Zn binding. Furthermore, X-vacancy binding, especially Gd-vacancy binding, exhibited sensitivity to the volumetric strain state, favoring compressive strains and suggesting an inhomogeneous segregation behavior (see Fig. 5.4) [55].

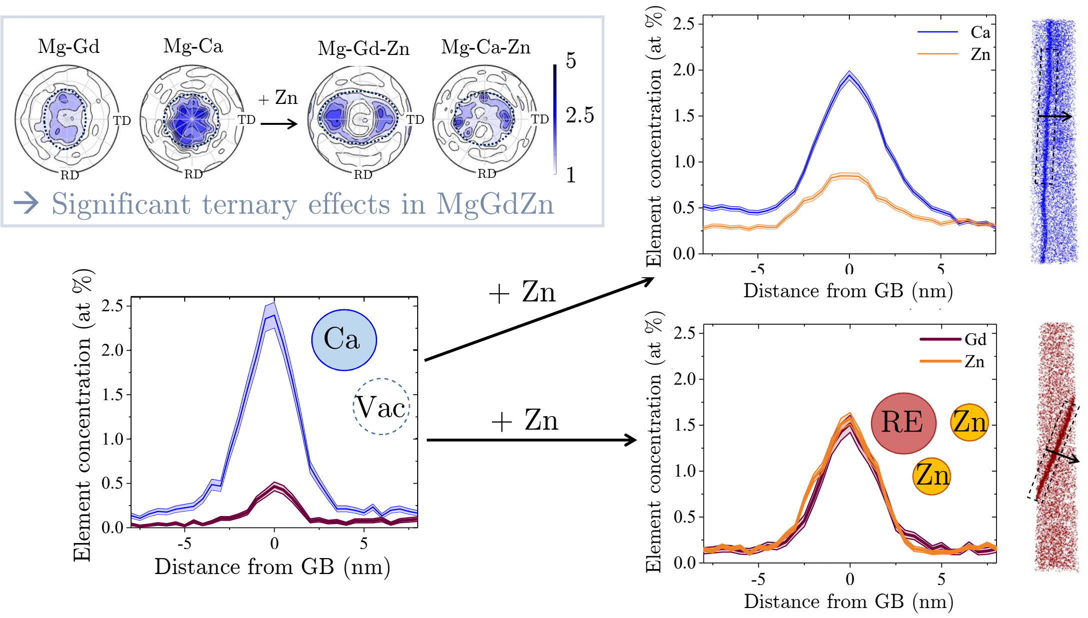

Higher Ca-vac. binding energy compared to Gd vs. higher Gd-Zn binding compared to Ca-Zn

Figure 5.4: Graphical abstract showing the main findings on solute effects on binding, segregation and texture [55].

5. Establishing a basic understanding of the impact of solutes on the active slip mechanisms and the resulting mechanical properties (publication 1 + 2 + 5).

Regarding mechanical properties, the addition of Zn induced an enhancement in the yield strength, strain hardening capability, and failure ductility compared to corresponding Mg-RE binary alloys. EBSD-assisted slip trace analysis at 5% strain for Mg-Er and Mg-Er-Zn unraveled promoted non-basal slip behavior in both binary and ternary alloys compared to classical magnesium alloys. However, Zn additions further enhanced the activation of non-basal slip while concurrently reducing the occurrence of basal slip [57]. Mg-Gd-Zn alloys with varying Gd:Zn solute ratios, revealed that the magnitude of non basal relative to basal slip events increased with a decreasing Gd:Zn solute ratio. Tensile testing of ternary Mg-Gd-Zn alloys in both RD and TD revealed a planar anisotropy in yield stress, which increased for lower Gd:Zn solute ratios. This RD/TD anisotropy was suspected to be correlated to texture dependant twin activation. A comparative assessment of slip activation under strain in RD and TD for the same alloy composition revealed a similar activation of common slip systems, but enhanced twinning under strain in TD (see Fig. 5.3) [56]. In the chase of Mg_2Ca laves phases, classical atomistic simulation and ab-initio calculations proved that synchro-shear is energetically favorable, establishing it as the predominant deformation mechanism on the basal plane [28].

5.2 Scientific Contribution

The present dissertation confirmed the unique ±40° transverse direction (TD) recrystallization texture in Mg-Gd-Zn and, for the first time, in Mg-Er-Zn. This distinct texture transition was attributed to the early stages of recrystallization (publication 1). An exploration of nucleation vs. selective growth, proved the importance of both, distinct nucleation sites providing off-basal nuclei and their selective growth, to the survival of off-basal texture components in the final texture (publication 1+2+3). In this regard double twins were identified as effective nucleation sites (publication 3). New insights on the role of the alloy composition in ternary Mg-RE-Zn alloys, e.g. solute ratios, reveal that the solute ratio rather than the absolute solute concentrations governs segregation and deformation modes. This research underscores the importance of synergistic effects to the final material properties and reveals the possibility to control these effects through solute ratios, offering a pathway towards tailored texture design (publication 2). Addressing the topic of RE substitution by Ca, beneficial texture alterations in Mg-Ca alloys were shown. However, synergistic solute effects were found predominantly effective in RE containing alloys, compared to Mg-Ca-Zn. The underlying mechanisms were explored on the atomic scale by atom probe tomography and ab initio calculations, identifying significant differences in segregation behavior and binding energies of Ca and Gd (publication 4).

The findings of this dissertation collectively emphasize the role of alloy composition and synergistic effects in shaping recrystallization textures and mechanical properties, encouraging further research towards targeted texture design and alloy development.

Chapter 6

Outlook

This thesis is a step towards understanding the connection between alloy composition, microstructure and resulting properties. However, the complexity of possible solute-defect interactions demands further atomic scale investigations.

Solute additions have proven to alter texture greatly, by means of selective growth of specific texture components favoring the activation of easy basal slip and hence enhance sheet formability. This is likely governed by solute-boundary interactions affecting the grain boundary mobility during annealing treatments. Selective growth would require an anisotropic behaviour of these interactions for different grain boundaries. Possible anisotropic segregation, as well as anisotropic effects on the grain boundary mobility have to be studied systematically.

Although this study provides promising atom probe insights suitable to explore microstructure development, extensive atomic scale studies of isolated solute-defect interactions are still needed.

It was shown that the magnitude of solute-boundary interactions depends strongly on synergistic properties resulting from different alloying concentrations of rare earth and transition elements. However, while synergistic effects can be presumed to have a strong influence on solute-defect interactions and thereby on microstructure evolution, a comprehensive understanding of the underlying mechanisms is yet to be achieved. As there are indications for the importance of the electronic properties of the elements, further ab-initio studies are crucial.

In summery, there is a great need for experimental and computational atomic-scale studies of solute-solute and solute-defect interactions to explore effective solute-combinations and their effect on different grain boundaries and dislocations. Unless these mechanisms are not fully understood, targeted alloy design will lack vital information.

References

[1] M. Arul Kumar, I. J. Beyerlein, and C. N. Tomé. “A measure of plastic anisotropy for hexagonal close packed metals: Application to alloying effects on the formability of Mg”. In: *Journal of Alloys and Compounds* 695 (2017), pp. 1488–1497. ISSN: 09258388. DOI: `10.1016/j.jallcom.2016.10.287`.

[2] Melvin Avrami. “Kinetics of Phase Change. I General Theory”. In: *The Journal of Chemical Physics* 7.12 (1939), pp. 1103–1112. DOI: `10.1063/1.1750380`. eprint: `https://doi.org/10.1063/1.1750380`. URL: `https://doi.org/10.1063/1.1750380`.

[3] Melvin Avrami. “Kinetics of Phase Change. II Transformation-Time Relations for Random Distribution of Nuclei”. In: *The Journal of Chemical Physics* 8.2 (1940), pp. 212–224. DOI: `10.1063/1.1750631`. eprint: `https://doi.org/10.1063/1.1750631`. URL: `https://doi.org/10.1063/1.1750631`.

[4] M. R. Barnett. “A Taylor Model Based Description of the Proof Stress of Magnesium AZ31 during Hot Working”. In: *METALLURGICAL AND MATERIALS TRANSACTIONS A* 34 (2003).

[5] M.R. Barnett, M.D. Nave, and C.J. Bettles. “Deformation microstructures and textures of some cold rolled Mg alloys”. In: *Materials Science and Engineering: A* 386.1 (2004), pp. 205–211. ISSN: 0921-5093. DOI: `https://doi.org/10.1016/j.msea.2004.07.030`. URL: `https://www.sciencedirect.com/science/article/pii/S0921509304009426`.

[6] C. M. Barr et al. “The role of grain boundary character in solute segregation and thermal stability of nanocrystalline Pt-Au”. In: *Nanoscale* 13.6 (2021), pp. 3552–3563. ISSN: 2040-3372 (Electronic) 2040-3364 (Linking). DOI: `10.1039/d0nr07180c`. URL: `https://www.ncbi.nlm.nih.gov/pubmed/33491721`.

[7] Christopher D. Barrett, Haitham El Kadiri, and Robert Moser. “Generalized interfacial fault energies”. In: *International Journal of Solids and Structures* 110-111 (2017), pp. 106–112. ISSN: 00207683. DOI: `10.1016/j.ijsolstr.2017.01.036`.

[8] Christopher D. Barrett, Aidin Imandoust, and Haitham El Kadiri. "The effect of rare earth element segregation on grain boundary energy and mobility in magnesium and ensuing texture weakening". In: *Scripta Materialia* 146 (2018), pp. 46–50. ISSN: 13596462. DOI: `10.1016/j.scriptamat.2017.11.004`.

[9] MI Baskes. "Modified embedded-atom potentials for cubic materials and impurities". In: *Physical Review B* 46 (1992), pp. 2727–2742. DOI: `10.1103/PhysRevB.46.2727`.

[10] I. Basu and T. Al-Samman. "Triggering rare earth texture modification in magnesium alloys by addition of zinc and zirconium". In: *Acta Materialia* 67 (2014), pp. 116–133. ISSN: 13596454. DOI: `10.1016/j.actamat.2013.12.015`.

[11] I. Basu et al. "The role of atomic scale segregation in designing highly ductile magnesium alloys". In: *Acta Materialia* 116 (2016), pp. 77–94. ISSN: 13596454. DOI: `10.1016/j.actamat.2016.06.024`.

[12] Indranil Basu, Talal Al Samman, and Günter Gottstein. "Recrystallization and Grain Growth Related Texture and Microstructure Evolution in Two Rolled Magnesium Rare-Earth Alloys". In: *Materials Science Forum* 765 (2013), pp. 527–531. ISSN: 1662-9752. DOI: `10.4028/www.scientific.net/MSF.765.527`.

[13] Indranil Basu and Talal Al-Samman. "Hierarchical Twinning Induced Texture Weakening in Lean Magnesium Alloys". In: *Frontiers in Materials* 6 (2019). ISSN: 2296-8016. DOI: `10.3389/fmats.2019.00187`.

[14] BJ Berne, G Cicootti, and DF Coker. *Classical and Quantum Dynamics in condensed Phase Simulations*. World Scientific, 1998.

[15] Peter E Blöchl. "Projector augmented-wave method". In: *Physical review B* 50.24 (1994), p. 17953.

[16] Yasumasa Chino, Motohisa Kado, and Mamoru Mabuchi. "Enhancement of tensile ductility and stretch formability of magnesium by addition of 0.2wt%(0.035at%)Ce". In: *Materials Science and Engineering: A* 494.1 (2008), pp. 343–349. ISSN: 0921-5093. DOI: `10.1016/j.msea.2008.04.059`. URL: `https://www.sciencedirect.com/science/article/pii/S092150930800508X`.

[17] MF Chisholm, S Kumar, and P Hazzledine. "Dislocations in Complex Materials". In: *Science* 307 (2005), pp. 701–703. DOI: `10.1126/science.1107703`.

[18] MS Daw and MI Baskes. "Embedded-atom method: Derivation and application to impurities, surfaces, and other defects in metals". In: *Physical Review B* 29 (1984), pp. 6443–6453. DOI: `10.1103/PhysRevB.29.6443`.

[19] Patrik Dobroň et al. “A study of mechanical anisotropy of Mg–Zn–Rare earth alloy sheet”. In: *Journal of Alloys and Compounds* 588 (2014), pp. 628–632. ISSN: 0925-8388. DOI: `https://doi.org/10.1016/j.jallcom.2013.11.142`. URL: `https://www.sciencedirect.com/science/article/pii/S0925838813028831`.

[20] Y.Z. Du et al. “Effect of microalloying with Ca on the microstructure and mechanical properties of Mg-6 mass%Zn alloys”. In: *Materials & Design* 98 (2016), pp. 285–293. ISSN: 0264-1275. DOI: `10.1016/j.matdes.2016.03.025`. URL: `https://www.sciencedirect.com/science/article/pii/S0264127516303070`.

[21] B.J. Duggan et al. “On the origin of cube texture in copper”. In: *Acta Metallurgica et Materialia* 41.6 (1993), pp. 1921–1927. ISSN: 0956-7151. DOI: `https://doi.org/10.1016/0956-7151(93)90211-A`. URL: `https://www.sciencedirect.com/science/article/pii/095671519390211A`.

[22] Martina Freund et al. “Plastic deformation of the CaMg2 C14-Laves phase from 50 - 250°C”. In: *Materialia* (2021). URL: `https://api.semanticscholar.org/CorpusID:244192495`.

[23] Robert Gehrmann, Matthias M. Frommert, and Günter Gottstein. “Texture effects on plastic deformation of magnesium”. In: *Materials Science and Engineering: A* 395.1 (2005), pp. 338–349. ISSN: 0921-5093. DOI: `https://doi.org/10.1016/j.msea.2005.01.002`. URL: `https://www.sciencedirect.com/science/article/pii/S0921509305000377`.

[24] P Giannozzi et al. “Advanced capabilities for materials modelling with Quantum ESPRESSO”. In: *Journal of Physics: Condensed Matter* 29.46 (Oct. 2017), p. 465901. DOI: `10.1088/1361-648X/aa8f79`. URL: `https://dx.doi.org/10.1088/1361-648X/aa8f79`.

[25] Paolo Giannozzi et al. “QUANTUM ESPRESSO: a modular and open-source software project for quantum simulations of materials”. In: *Journal of Physics: Condensed Matter* 21.39 (Sept. 2009), p. 395502. DOI: `10.1088/0953-8984/21/39/395502`. URL: `https://dx.doi.org/10.1088/0953-8984/21/39/395502`.

[26] J. S. K. Gibson et al. “Finding and Characterising Active Slip Systems: A Short Review and Tutorial with Automation Tools”. In: *Materials (Basel)* 14.2 (2021). ISSN: 1996-1944 (Print) 1996-1944 (Linking). DOI: `10.3390/ma14020407`. URL: `https://www.ncbi.nlm.nih.gov/pubmed/33467559`.

[27] Günter Gottstein. “Recovery, Recrystallization, Grain Growth”. In: *Physical Foundations of Materials Science*. Berlin, Heidelberg: Springer Berlin Heidelberg, 2004, pp. 303–356. ISBN: 978-3-662-09291-0. DOI: `10.1007/978-3-662-09291-0_8`. URL: `https://doi.org/10.1007/978-3-662-09291-0_8`.

[28] Julien Guénolé et al. “Basal slip in Laves phases: The synchroshear dislocation”. In: *Scripta Materialia* 166 (2019), pp. 134–138. ISSN: 13596462. DOI: `10.1016/j.scriptamat.2019.03.016`.

[29] Saadi A. Habib et al. “Anisotropy, tension-compression asymmetry and texture evolution of a rare-earth-containing magnesium alloy sheet, ZEK100, at different strain rates and temperatures: Experiments and modeling”. In: *International Journal of Plasticity* 95 (2017), pp. 163–190. ISSN: 0749-6419. DOI: `https://doi.org/10.1016/j.ijplas.2017.04.006`. URL: `https://www.sciencedirect.com/science/article/pii/S0749641916302224`.

[30] Jason P. Hadorn et al. “Role of Solute in the Texture Modification During Hot Deformation of Mg-Rare Earth Alloys”. In: *Metallurgical and Materials Transactions A* 43.4 (2011), pp. 1347–1362. ISSN: 1073-5623 1543-1940. DOI: `10.1007/s11661-011-0923-5`.

[31] K. Hantzsche et al. “Effect of rare earth additions on microstructure and texture development of magnesium alloy sheets”. In: *Scripta Materialia* 63.7 (2010), pp. 725–730. ISSN: 13596462. DOI: `10.1016/j.scriptamat.2009.12.033`.

[32] PM Hazzledine and P Pirouz. “Synchroshear transformation in laves phases”. In: *Scripta Metallurgica et Materialia* 28 (1993), pp. 1277–1282. DOI: `10.1016/0956-716X(93)90178-2`.

[33] C. He et al. “Unusual solute segregation phenomenon in coherent twin boundaries”. In: *Nat Commun* 12.1 (2021), p. 722. ISSN: 2041-1723 (Electronic) 2041-1723 (Linking). DOI: `10.1038/s41467-021-21104-8`. URL: `https://www.ncbi.nlm.nih.gov/pubmed/33526770`.

[34] Emmanuel Hersent, Knut Marthinsen, and Erik Nes. “The Effect of Solute Atoms on Grain Boundary Migration: A Solute Pinning Approach”. In: *Metallurgical and Materials Transactions A* 44.7 (2013), pp. 3364–3375. ISSN: 1073-5623 1543-1940. DOI: `10.1007/s11661-013-1690-2`.

[35] R. Hielscher and H. Schaeben. “A novel pole figure inversion method: specification of theMTEXalgorithm”. In: *Journal of Applied Crystallography* 41.6 (2008), pp. 1024–1037. ISSN: 0021-8898. DOI: `10.1107/s0021889808030112`.

[36] M. Hillert. "On the theory of normal and abnormal grain growth". In: *Acta Metallurgica* 13 (1965), pp. 227–238.

[37] M. Hillert. "SOLUTE DRAG, SOLUTE TRAPPING AND DIFFUSIONAL DISSIPATION OF GIBBS ENERGY". In: *Acta Materialia* 47 (1999), pp. 4481–4505.

[38] P Hohenberg and W Kohn. "Inhomogeneous Electron Gas". In: *Physical Review* 136 (1964), B864–B871. DOI: `10.1103/PhysRev.136.B864`.

[39] F.J. Humphreys and M. Hatherly. "Chapter 5 - The Mobility and Migration of Boundaries". In: *Recrystallization and Related Annealing Phenomena (Second Edition)*. Ed. by F.J. Humphreys and M. Hatherly. Second Edition. Oxford: Elsevier, 2004, pp. 121–167. ISBN: 978-0-08-044164-1. DOI: `https://doi.org/10.1016/B978-008044164-1/50009-8`. URL: `https://www.sciencedirect.com/science/article/pii/B9780080441641500098`.

[40] F.J. Humphreys and M. Hatherly. "Chapter 7 - Recrystallization of Single-Phase Alloys". In: *Recrystallization and Related Annealing Phenomena (Second Edition)*. Ed. by F.J. Humphreys and M. Hatherly. Second Edition. Oxford: Elsevier, 2004, pp. 215–IV. ISBN: 978-0-08-044164-1. DOI: `https://doi.org/10.1016/B978-008044164-1/50011-6`. URL: `https://www.sciencedirect.com/science/article/pii/B9780080441641500116`.

[41] Ki-Hyun Kim, Jong Bae Jeon, and Byeong-Joo Lee. "Modified embedded-atom method interatomic potentials for Mg–X (X=Y, Sn, Ca) binary systems". In: *Calphad* 48 (2015), pp. 27–34. DOI: `10.1016/j.calphad.2014.12.001`.

[42] W Kohn and LJ Sham. "Self-Consistent Equations Including Exchange and Correlation Effects". In: *Physical Review* 140 (1965), A1133–A1138. DOI: `10.1103/PhysRev.140.A1133`.

[43] Georg Kresse and Jürgen Furthmüller. "Efficiency of ab-initio total energy calculations for metals and semiconductors using a plane-wave basis set". In: *Computational materials science* 6.1 (1996), pp. 15–50.

[44] Georg Kresse and Daniel Joubert. "From ultrasoft pseudopotentials to the projector augmented-wave method". In: *Physical review b* 59.3 (1999), p. 1758.

[45] ML Kronberg. "Plastic deformation of single crystals of sapphire: Basal slip and twinning". In: *Acta Metallurgica* 5 (1957), pp. 507–523. DOI: `10.1016/0001-6160(57)90139-6`.

[46] KS Kumar and P Hazzledine. "Polytype transformation in Laves phases". In: *Intermetallics* 22 (2004), pp. 764–770. DOI: `10.1016/j.intermet.2004.01.003`.

[47] M. R. Li, D. W. Deng, and K. H. Kuo. “Crystal structure of the hexagonal (Zn, Mg)4Ho and (Zn, Mg)4Er”. In: *Journal of Alloys and Compounds* 414.1-2 (2006), pp. 66–72. ISSN: 09258388. DOI: `10.1016/j.jallcom.2005.07.008`.

[48] K. Lücke and K. Detert. “A quantitative theory of grain-boundary motion and recrystallization in metals in the presence of impurities”. In: *Acta Metallurgica* 5 (1956).

[49] J. Luo et al. “Cold rollability improvement by twinning and twin–slip synergy in an Mg–Zn–Gd alloy with rare earth texture”. In: *Journal of Alloys and Compounds* 883 (2021), p. 160813. ISSN: 0925-8388. DOI: `https://doi.org/10.1016/j.jallcom.2021.160813`. URL: `https://www.sciencedirect.com/science/article/pii/S0925838821022222`.

[50] L. Mackenzie and M. Pekguleryuz. “The recrystallization and texture of magnesium–zinc–cerium alloys”. In: *Scripta Materialia* 59.6 (2008), pp. 665–668. ISSN: 13596462. DOI: `10.1016/j.scriptamat.2008.05.021`.

[51] Reza Mahjoub and Nikki Stanford. “The electronic origins of the “rare earth” texture effect in magnesium alloys”. In: *Scientific Reports* 11.1 (2021). Cited by: 7; All Open Access, Gold Open Access, Green Open Access. DOI: `10.1038/s41598-021-93703-w`. URL: `https://www.scopus.com/inward/record.uri?eid=2-s2.0-85109416255&doi=10.1038%2fs41598-021-93703-w&partnerID=40&md5=ebcb23ffe4f7e526590a885b1a30ae89`.

[52] Alireza Maldar et al. “Activation of ¡c¿ dislocations in Mg with solute Y”. In: *Journal of Magnesium and Alloys* (2021). ISSN: 2213-9567. DOI: `https://doi.org/10.1016/j.jma.2021.11.004`. URL: `https://www.sciencedirect.com/science/article/pii/S2213956721002711`.

[53] D. McLean and A. Maradudin. “Grain Boundaries in Metals”. In: *Physics Today* 11.7 (1958), pp. 35–36. ISSN: 0031-9228 1945-0699. DOI: `10.1063/1.3062658`.

[54] F. Mouhib, B. Gao, and T. Al-Samman. “On the role of selective nucleation and growth to recrystallization texture development in a Mg-Gd-Zn alloy”. In: *Journal of Materials Science* 59 (2023). DOI: `https://doi.org/10.1007/s10853-023-09243-3`. URL: `https://link.springer.com/article/10.1007/s10853-023-09243-3#citeas`.

[55] F. Mouhib et al. “Exploring solute behavior and texture selection in magnesium alloys at the atomistic level”. In: *Acta Metaterialia* 266 (2024). DOI: `https://doi.org/10.1016/j.actamat.2024.119677`. URL: `https://www.sciencedirect.com/science/article/pii/S1359645424000302`.

[56] F. Z. Mouhib et al. "Synergistic effects of solutes on active deformation modes, grain boundary segregation and texture evolution in Mg-Gd-Zn alloys". In: *Materials Science and Engineering: A* 847 (2022), p. 143348. ISSN: 0921-5093. DOI: `https://doi.org/10.1016/j.msea.2022.143348`. URL: `https://www.sciencedirect.com/science/article/pii/S0921509322007456`.

[57] F. Z. Mouhib et al. "Texture Selection Mechanisms during Recrystallization and Grain Growth of a Magnesium-Erbium-Zinc Alloy". In: *Metals* 11.1 (2021). ISSN: 2075-4701. DOI: `10.3390/met11010171`. URL: `https://www.mdpi.com/2075-4701/11/1/171`.

[58] J. F. Nie et al. "Periodic segregation of solute atoms in fully coherent twin boundaries". In: *Science* 340.6135 (2013), pp. 957–60. ISSN: 1095-9203 (Electronic) 0036-8075 (Linking). DOI: `10.1126/science.1229369`. URL: `https://www.ncbi.nlm.nih.gov/pubmed/23704567`.

[59] Maria Nienaber et al. "Processing Effects on the Formability of Extruded Flat Products of Magnesium Alloys". In: *Frontiers in Materials* 6 (2019). ISSN: 2296-8016. DOI: `10.3389/fmats.2019.00253`. URL: `https://www.frontiersin.org/articles/10.3389/fmats.2019.00253`.

[60] R Oppenheimer and M Born. "Quantisierung als Eigenwertproblem". In: *Annalen der Physik* 84 (1927), pp. 457–484. DOI: `10.1002/andp.19273892002`.

[61] Risheng Pei et al. "Atomistic insights into the inhomogeneous nature of solute segregation to grain boundaries in magnesium". In: *Scripta Materialia* 230 (2023), p. 115432. ISSN: 1359-6462. DOI: `https://doi.org/10.1016/j.scriptamat.2023.115432`. URL: `https://www.sciencedirect.com/science/article/pii/S1359646223001562`.

[62] "Recrystallisation mechanisms and the origin of cube texture in copper". In: *Acta Metallurgica* 30.10 (1982), pp. 1929–1939. ISSN: 0001-6160. DOI: `https://doi.org/10.1016/0001-6160(82)90033-5`. URL: `https://www.sciencedirect.com/science/article/pii/0001616082900335`.

[63] Joseph D. Robson. "Effect of Rare-Earth Additions on the Texture of Wrought Magnesium Alloys: The Role of Grain Boundary Segregation". In: *Metallurgical and Materials Transactions A* 45.8 (2013), pp. 3205–3212. ISSN: 1073-5623 1543-1940. DOI: `10.1007/s11661-013-1950-1`.

[64] Joseph D. Robson et al. "Grain Boundary Segregation of Rare-Earth Elements in Magnesium Alloys". In: *Metallurgical and Materials Transactions A* 47 (2016). ISSN: 1543-1940. DOI: `10.1007/s11661-015-3199-3`.

[65] T. Al-Samman and X. Li. “Sheet texture modification in magnesium-based alloys by selective rare earth alloying”. In: *Materials Science and Engineering: A* 528.10 (2011), pp. 3809–3822. ISSN: 0921-5093. DOI: `10.1016/j.msea.2011.01.080`. URL: `https://www.sciencedirect.com/science/article/pii/S092150931100102X`.

[66] S. Sandlöbes et al. “Ductility improvement of Mg alloys by solid solution: Ab initio modeling, synthesis and mechanical properties”. In: *Acta Materialia* 70 (2014), pp. 92–104. ISSN: 13596454. DOI: `10.1016/j.actamat.2014.02.011`.

[67] S. Sandlöbes et al. “On the role of non-basal deformation mechanisms for the ductility of Mg and Mg–Y alloys”. In: *Acta Materialia* 59.2 (2011), pp. 429–439. ISSN: 13596454. DOI: `10.1016/j.actamat.2010.08.031`.

[68] S. Sandlöbes et al. “The relation between ductility and stacking fault energies in Mg and Mg–Y alloys”. In: *Acta Materialia* 60.6-7 (2012), pp. 3011–3021. ISSN: 13596454. DOI: `10.1016/j.actamat.2012.02.006`.

[69] Stefanie Sandlöbes et al. “Basal and non-basal dislocation slip in Mg–Y”. In: *Materials Science and Engineering: A* 576 (2013), pp. 61–68. ISSN: 09215093. DOI: `10.1016/j.msea.2013.03.006`.

[70] E Schrödinger. “Quantisierung als Eigenwertproblem”. In: *Annalen der Physik* 384 (1926), pp. 361–376. DOI: `10.1002/andp.19263840704`.

[71] X.H. Shao et al. “Atomic-scale segregations at the deformation-induced symmetrical boundary in an Mg-Zn-Y alloy”. In: *Acta Materialia* 118 (2016), pp. 177–186. ISSN: 1359-6454. DOI: `https://doi.org/10.1016/j.actamat.2016.07.054`. URL: `https://www.sciencedirect.com/science/article/pii/S1359645416305626`.

[72] Daniel Sheppard, Rye Terrell, and Graeme Henkelman. “A generalized solid-state nudged elastic band method”. In: *The Journal of Chemical Physics* 136 (2012). DOI: `10.1063/1.3671284`.

[73] JE Sinclair and MW Finnis. “A simple empirical N-body potential for transition metals”. In: *Philosophical magazine A* 50 (1984), pp. 45–55. DOI: `10.1080/01418618408244210`.

[74] N. Stanford et al. “Solute segregation and texture modification in an extruded magnesium alloy containing gadolinium”. In: *Scripta Materialia* 65.10 (2011), pp. 919–921. ISSN: 13596462. DOI: `10.1016/j.scriptamat.2011.08.012`.

[75] A. Styczynski et al. “Cold rolling textures in AZ31 wrought magnesium alloy”. In: *Scripta Materialia* 50.7 (2004), pp. 943–947. ISSN: 13596462. DOI: `10.1016/j.scriptamat.2004.01.010`.

[76] Masanori Takenaka et al. "Unique effect of carbon addition on development of deformation texture through changes in slip activation and twin deformation in heavily cold-rolled Fe-3% Si alloys". In: *Acta Materialia* 157 (Sept. 2018), pp. 196–208. DOI: `10.1016/j.actamat.2018.07.019`.

[77] "Technology of Magnesium and Magnesium Alloys". In: *Magnesium Technology: Metallurgy, Design Data, Applications*. Berlin, Heidelberg: Springer Berlin Heidelberg, 2006, pp. 219–430. ISBN: 978-3-540-30812-6. DOI: `10.1007/3-540-30812-1_6`. URL: `https://doi.org/10.1007/3-540-30812-1_6`.

[78] Erich Tenckhoff. "Deformation mechanisms, texture, and anisotropy in zirconium and Zircaloy". In: 1988. URL: `https://api.semanticscholar.org/CorpusID:136756480`.

[79] Olena Vedmedenko, Frohmut Rösch, and Christian Elsässer. "First-principles density functional theory study of phase transformations in NbCr2 and TaCr2". In: *Acta Materialia* 56.18 (2008), pp. 4984–4992. DOI: `10.1016/j.actamat.2008.06.018`.

[80] Loup Verlet. "Computer "Experiments" on Classical Fluids. I. Thermodynamical Properties of Lennard-Jones Molecules". In: *Physical Review* 159 (1967), pp. 98–103. DOI: `10.1103/PhysRev.159.98`.

[81] F. Wang et al. "In situ observation of collective grain-scale mechanics in Mg and Mg–rare earth alloys". In: *Acta Materialia* 80 (2014), pp. 77–93. ISSN: 13596454. DOI: `10.1016/j.actamat.2014.07.048`.

[82] Y. N. Wang and J. C. Huang. "Texture analysis in hexagonal materials". In: *Materials Chemistry and Physics* 81.1 (2003), pp. 11–26. ISSN: 02540584. DOI: `10.1016/s0254-0584(03)00168-8`.

[83] Jing Wu et al. "Study of basal $< a >$ and pyramidal $< c+a >$ slips in Mg-Y alloys using micro-pillar compression". In: *Philosophical Magazine* 100.11 (2020), pp. 1454–1475. DOI: `10.1080/14786435.2020.1725250`. URL: `https://doi.org/10.1080/14786435.2020.1725250`.

[84] Z. R. Zeng et al. "Texture evolution during static recrystallization of cold-rolled magnesium alloys". In: *Acta Materialia* 105 (2016), pp. 479–494. ISSN: 13596454. DOI: `10.1016/j.actamat.2015.12.045`.

[85] Z.R. Zeng et al. "Effects of dilute additions of Zn and Ca on ductility of magnesium alloy sheet". In: *Materials Science and Engineering: A* 674 (2016), pp. 459–471. ISSN: 0921-5093. DOI: `10.1016/j.msea.2016.07.049`. URL: `https://www.sciencedirect.com/science/article/pii/S0921509316308115`.

[86] Quan Zhang et al. “Ab-initio study of the effect of rare-earth elements on the stacking faults of Mg solid solutions”. In: *Intermetallics* 29 (2012), pp. 21–26. ISSN: 09669795. DOI: `10.1016/j.intermet.2012.04.015`.

Chapter 7

Publications

7.1 Texture Selection Mechanisms during Recrystallization and Grain Growth of a Magnesium-Erbium-Zinc Alloy.

F. Z. Mouhib[1], F. Sheng[1], R. Mandia[1], R. Pei[1],S. Korte-Kerzel[1] and T. Al-Samman[1].
[1]Institute of Physical Metallurgy and Materials Physics, RWTH Aachen University, Germany

Metals 11.1 (2021) issn: 2075-4701

The candidate carried out the conceptualisation, participated in the experimental work, guided and performed data analysis and did writing and editing of the manuscript.

Online availability: https://doi.org/10.3390/met11010171.

metals

MDPI

Article

Texture Selection Mechanisms during Recrystallization and Grain Growth of a Magnesium-Erbium-Zinc Alloy

Fatim-Zahra Mouhib *, Fengyang Sheng, Ramandeep Mandia, Risheng Pei, Sandra Korte-Kerzel and Talal Al-Samman

Institute for Physical Metallurgy and Materials Physics, RWTH Aachen, 52056 Aachen, Germany; fengyang.sheng@rwth-aachen.de (F.S.); rmandia@asu.edu (R.M.); pei@imm.rwth-aachen.de (R.P.); korte-kerzel@imm.rwth-aachen.de (S.K.-K.); alsamman@imm.rwth-aachen.de (T.A.-S.)

* Correspondence: mouhib@imm.rwth-aachen.de

Abstract: Binary and ternary Mg-1%Er/Mg-1%Er-1%Zn alloys were rolled and subsequently subjected to various heat treatments to study texture selection during recrystallization and following grain growth. The results revealed favorable texture alterations in both alloys and the formation of a unique ±40° transvers direction (TD) recrystallization texture in the ternary alloy. While the binary alloy underwent a continuous alteration of its texture and grain size throughout recrystallization and grain growth, the ternary alloy showed a rapid rolling (RD) to transvers direction (TD) texture transition occurring during early stages of recrystallization. Targeted electron back scatter diffraction (EBSD) analysis of the recrystallized fraction unraveled a selective growth behavior of recrystallization nuclei with TD tilted orientations that is likely attributed to solute drag effect on the mobility of specific grain boundaries. Mg-1%Er-1%Zn additionally exhibited a stunning microstructural stability during grain growth annealing. This was attributed to a fine dispersion of dense nanosized particles in the matrix that impeded grain growth by Zener drag. The mechanical properties of both alloys were determined by uniaxial tensile tests combined with EBSD assisted slip trace analysis at 5% tensile strain to investigate non-basal slip behavior. Owing to synergic alloying effects on solid solution strengthening and slip activation, as well as precipitation hardening, the ternary Mg-1%Er-1%Zn alloy demonstrated a remarkable enhancement in the yield strength, strain hardening capability, and failure ductility, compared with the Mg-1%Er alloy.

Keywords: magnesium-rare earth alloy; recrystallization; selective grain growth; texture

check for updates

Citation: Mouhib, F.-Z.; Sheng, F.; Mandia, R.; Pei, R.; Korte-Kerzel, S.; Al-Samman, T. Texture Selection Mechanisms during Recrystallization and Grain Growth of a Magnesium-Erbium-Zinc Alloy. *Metals* **2021**, *11*, 171. https://doi.org/10.3390/met11010171

Received: 29 December 2020
Accepted: 15 January 2021
Published: 19 January 2021

1. Introduction

As of late, there is an increasing trend for using magnesium alloys in the automotive and aerospace industries owing to their excellent specific strength properties and light-weighting potential. However, a broad technical application of wrought magnesium alloy products still struggles with the difficulty to form at temperatures below 150 °C caused by the formation of a sharp basal texture and limited activation of deformation modes outside of the basal plane [1,2]. Great research efforts have been explored to not only alter the sharp sheet texture but also to control its strength and evolution [2–4]. Magnesium rare earth (RE) alloys have proven very useful in enhancing the cold formability and the work hardening capability of conventional magnesium alloys. This has been attributed to the development of a unique sheet annealing texture characterized by an off-basal pole spread away from the normal direction of the sheet plane [4–7]. Numerous recrystallization and growth mechanisms were explored in an attempt to unravel the underlying mechanisms for the favorable texture development in magnesium rare earth alloys. These included particle stimulated nucleation, deformation twin nucleation, and shear band nucleation mechanisms, which are known to promote random orientations or off-basal orientations of recrystallization nuclei [8]. However, since these mechanisms can also occur in magnesium alloys containing no RE elements [9–11], the research on the origin of the specific texture selection in Mg-RE alloys is still ongoing.

Recent studies in that context looked into a connection between RE solutes and oriented nucleation/growth during recrystallization, given that specific RE-textures have been observed in dilute alloys in which the RE elements were mostly in solid solution. It was also shown that the addition of zinc to Mg-RE alloys has proven to further weaken the texture and augment its off-basal nature [12]. Hence, more studies are needed to investigate the interaction of multiple solute species, particularly ones with largely different atomic radii [12,13]. Additionally, it is essential to examine how different RE and non-RE solute-boundary interactions impact the growth selection during texture evolution in Mg-RE and Mg-RE-Zn alloys.

This study aims at understanding the formation of unique sheet textures and the ensuing selection mechanisms in Er-containing magnesium alloys with and without the presence of Zn. Reports on this alloy system with respect to deformation and recrystallization textures are scarce in the literature. It is therefore important to illustrate the great texture modification potential the present alloys have to offer. In particular, the formation of a double-peak split texture in the transverse direction, similar to what is common for hexagonal metals with c/a < 1.633, is a unique feature that is hardly seen in Mg alloys subjected to rolling and annealing treatments. The discussion addresses the texture development in both binary and ternary versions of the alloy during recrystallization and grain growth under the influence of solutes and second phase precipitates.

2. Materials and Methods

Binary and ternary Mg-1%Er-(1%Zn) (wt %) alloys were melted in an induction furnace under an Ar/CO_2 gas atmosphere and subsequently casted and homogenized at 420 °C for 960 min. The resulting microstructure is shown in Figure 1. Table 1 shows the chemical composition measured by ICP/OES (IME RWTH University, Aachen, Germany). Sheets of the dimension 60 × 40 × 4 mm^3 were hot rolled at 400 °C with multiple rolling passes (eleven) and a final thickness reduction of 80%.

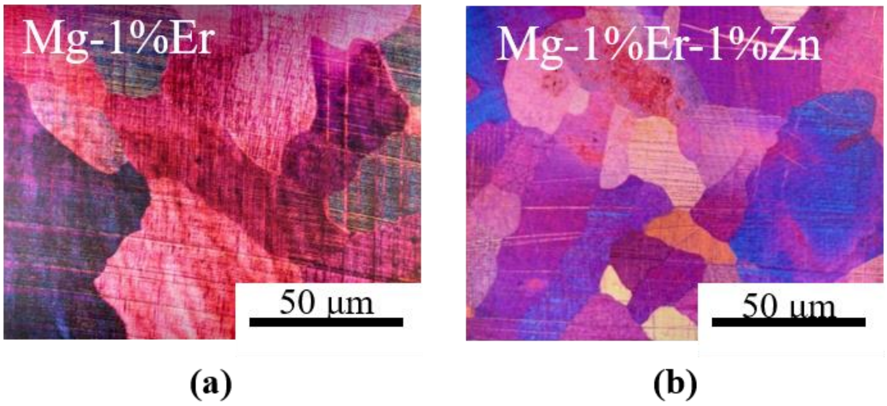

Figure 1. Micrographs of Mg-1%Er (**a**) and Mg-1%Er-1%Zn (**b**) after casting.

Table 1. Chemical composition in atomic and weight percentage of Mg-1%Er and Mg-1%Er-1%Zn.

Alloys	Mg (wt %/at %)		Er (wt %/at %)		Zn (wt %/at %)	
Mg-Er	99.04	99.86	0.96	0.14	/	
Mg-Er-Zn	98.01	99.46	0.93	0.14	1.06	0.40

Annealing treatments at 350 °C and 400 °C were conducted in a Heraeus RL200E air furnace (Heraeus Group, Hanau, Germany) for annealing times ranging from 5 to 1440 min and in a sand bath furnace for annealing times smaller than 5 min.

All samples were mechanically ground to the specimen mid-plane and polished with a diamond suspension up to 0.25 µm. For optical light microscopy (Leica microsystems, Wetzlar, Germany), the samples were electro-polished for 40 min in a 5:3 ethanol H_3PO_3 solution at 2 V and etched in an acetic picral solution. Grain size measurements from light microscopy images were performed by means of the linear intercept method. Texture measurements were conducted using a Bruker D8 advance diffractometer (Bruker, Billerica, MA, USA) operating at 30 V and 25 mA. Six incomplete pole figures [$\{10\bar{1}0\}$, $\{0002\}$, $\{10\bar{1}1\}$, $\{10\bar{1}2\}$, $\{11\bar{1}0\}$, $\{10\bar{1}3\}$] were measured, from which full pole figures and orientation distribution functions (ODFs) were calculated with the texture analysis toolbox MTEX (MTEX 5.3, Chemnitz, Germany) [14]. For selected samples intended for electron backscatter diffraction (EBSD) analysis under the electron beam an alternative electro-polishing procedure was employed using Lectro-Pol 5 in a Struers AC-2 solution at a voltage of 25 V and −20 °C for 120 s. Microstructure analysis via EBSD was performed using a LEO-1530 scanning electron microscope (Carl Zeiss Microscopy GmbH, Jena, Germany) operating at 20 kV, equipped with a HKL-Nordlys II EBSD detector. The detection step size varied according to the grain size in a range from 0.5 to 1.5 µm. EBSD and X-Ray diffraction (XRD) raw data were analyzed using the MTEX toolbox [14].

For the characterization of precipitates panorama back scatter electron (BSE)imaging (50 images per specimen) was conducted under a magnification of 10,000× with a focused ion beam Helios 600i (Thermo Fisher Scientific, Waltham, MA, USA) equipped with a field emission electron gun operating at 5 kV.

Recrystallization (RX) kinetics for both alloys were obtained by Vickers micro-hardness measurements (HMV, Shimadzu, Nakagyo-ku, Kyōto, Japan) (load of 1 N) of specimens subjected to interrupted annealing at 350 °C for durations up to 1000 s. For each annealing condition, 15 indentations were used to determine the average hardness HV_t at time step t. The recrystallized fraction was calculated by the common Equation (1), where $HV_{initial}$ and HV_{final} denote the initial and final hardness values, respectively [15].

$$X = \frac{HV_{initial} - HV_t}{HV_{initial} - HV_{final}} \quad (1)$$

The mechanical properties were determined by uniaxial tensile tests at room temperature conducted along the rolling direction on fully recrystallized samples of both alloys. The tensile samples were carefully chosen to have a similar grain size in order to exclude grain size effects on the yield strength response of the material. Dog-bone-shaped samples with gauge dimensions of $5 \times 1.5 \times 0.8$ mm^3 were cut out of the rolling sheets and subsequently annealed at 400 °C for 15 and 60 min for the binary and ternary alloys, respectively. Tensile tests were conducted using a ZWICK tension-compression testing machine. Specimens were strained under a constant strain rate of 2×10^{-4} to failure. Each tensile test was performed three times to ensure reproducibility and the average flow curve was considered for the analysis. In order to determine the operating slip systems during uniaxial tension, interrupted tensile tests were performed up to 5% strain on samples annealed at 400 °C for 60 min of both alloys. Subsequently, the slip systems were determined by comparison of slip lines from secondary electron (SE) images obtained at 20 kV and the grain orientations determined by EBSD of at least 120 grains each.

3. Results

3.1. Microstructure Evolution

Figure 2 shows the optical microstructures of rolled and annealed samples of the binary and ternary Mg-1%Er-(1%Zn) alloys. The annealing temperature was 400 °C and the annealing times were 15 and 360 min, respectively. The corresponding XRD textures, presented in terms of (0002) pole figures, as well as the evolution of the average grain size as a function of the annealing time are given in Figure 3. As it can be seen, both alloys exhibited a common deformation microstructure characterized by deformed grains and numerous deformation twins. The rolling texture of the binary alloy showed a typical basal component with a pole spread towards the rolling direction (RD) and moderate intensity. On the other hand, the ternary alloy exhibited a weaker and much softer rolling texture characterized by two off-basal components at ±20° RD that bare a significant pole spread in the transverse direction TD.

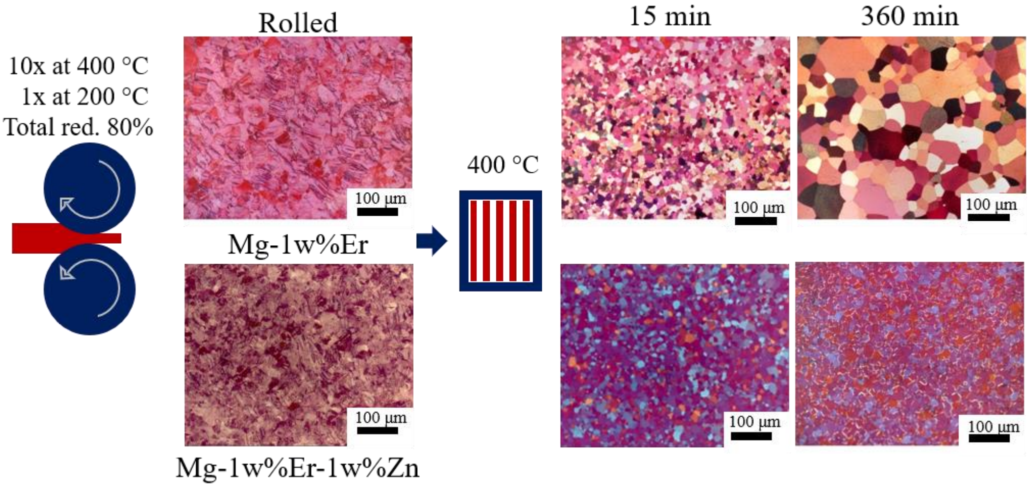

Figure 2. Micrographs of Mg-1%Er and Mg-1%Er-1%Zn in the as-rolled state and upon annealing at 400 °C for 15 and 360 min. The images are taken from the rolling plane (mid-thickness).

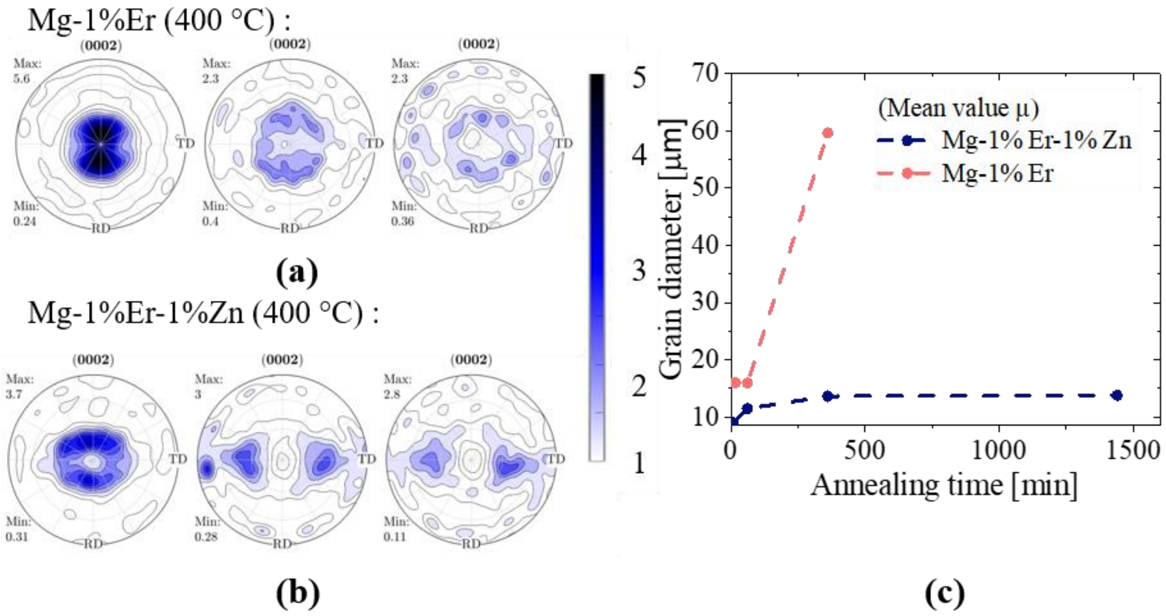

Figure 3. Texture evolution of binary and ternary (**a**,**b**) Mg-1%Er-(1%Zn) in the as rolled state and after annealing at 400 °C for 15 and 360 min, as well as the corresponding evolution of the mean grain diameter over time (**c**).

During a subsequent heat treatment at 400 °C, the ternary alloy seemed to develop a fine-grained annealing microstructure with a stable grain size (14 µm) that was not liable to additional grain growth at increased annealing durations (Figure 2). The corresponding annealing texture witnessed a unique transition demonstrated by new off-basal components appearing at ±40° TD. This type of annealing texture after rolling is only common for hcp metals like titanium [16], that have a lower c/a ratio than the ideal ratio of 1.633 for close-packed structures, and can thus easily activate prismatic and pyramidal slip. As to the binary alloy, it exhibited an initially stable grain size (16 µm) up to an annealing time of 60 min but underwent significant grain growth (60 µm) after 360 min of annealing

(Figure 3c). The texture of the binary Mg-1%Er alloy during early annealing conserved the dominant pole split in RD seen in the deformation texture but was also significantly weakened as a result of recrystallization (5.6 MRD → 2.3 MRD). With prolonged annealing up to 360 min, the texture spread around the normal direction ND seemed to increase during grain growth and the basal component in the center of the pole figure has vanished.

Given the interesting nature of the texture transition seen upon annealing of the Mg-1%Zn-1%Er alloy, additional annealing experiments were carried out at a lower temperature of 350 °C. The annealing durations were kept short—i.e., up to 15 min—in order to capture the effect of early recrystallization stages on the texture transition. The results are shown in Figure 4, which demonstrates how the ±20° RD deformation texture transforms into a ±40° TD annealing texture accompanied by full recrystallization of the specimen. Figure 5 shows the distribution of the basal poles (or c-axes) with respect to the rolling and transvers directions for the ternary (bottom) and binary alloy (top) along with their inverse pole figure (IPF) maps at 400 °C/360 min. Based on the annealing durations, the data clearly reveals that the texture established during recrystallization in the ternary alloy is preserved during subsequent grain growth, as the orientation distribution relative to the TD and RD remains virtually unchanged (Figure 5c). In case of the binary alloy, the total area fraction of grains with a large TD pole spread increases significantly with the annealing duration, whereas the area distribution of the RD spread remains almost constant (Figure 5b).

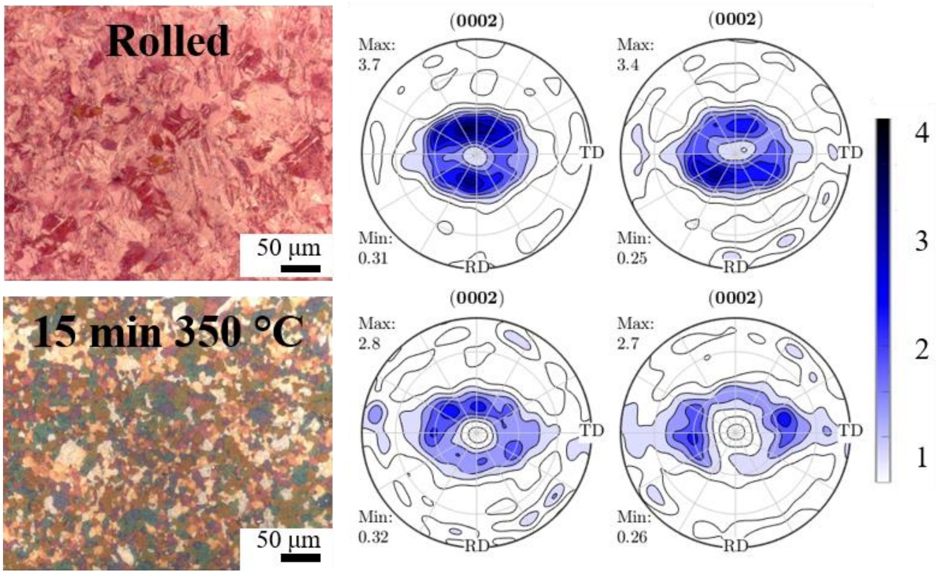

Figure 4. Texture evolution during recrystallization of Mg-1%Er-1%Zn annealed at 350 °C for 0, 5, 7, and 15 min.

With respect to second phase precipitates in the microstructure, the ternary alloy was found to exhibit a fine distribution of nano-scale precipitates and also larger ones that were sometimes clustered together, as shown in Figure 6. Energy dispersive X-ray spectroscopy (EDS) point analysis and elemental mapping were employed to investigate the chemical composition of these large precipitates. The results revealed a particle composition with a magnesium to zinc to erbium ratio of approximately 5:5:1. A similar zinc to erbium ratio was previously reported for several hexagonal and icosahedral quasi-crystalline $(\mathrm{Mg}, \mathrm{Zn})_x Er$ compounds [17,18].

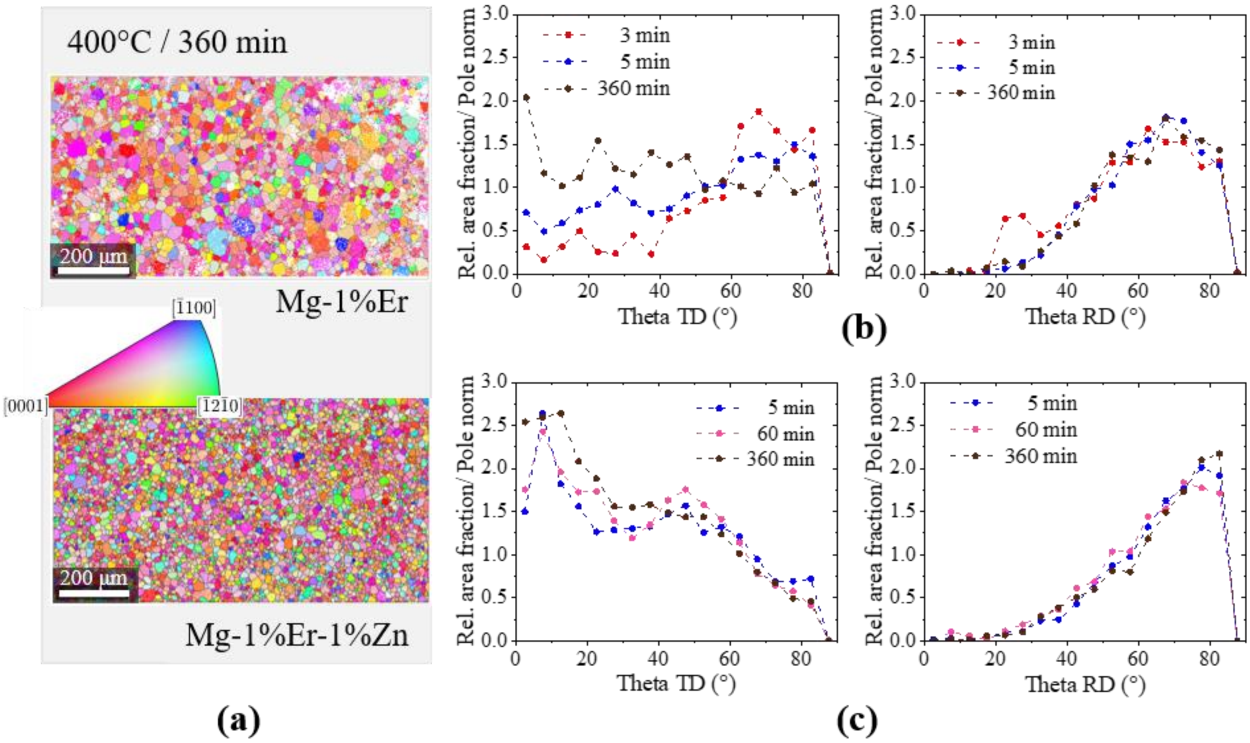

Figure 5. (**a**) EBSD ND-IPF maps of binary (top) and ternary Mg-1%Er-(1%Zn) (bottom) alloys annealed at 400 °C for 360 min; (**b**,**c**) angle distribution profiles between the c-axis and the transverse and rolling directions for different annealing durations.

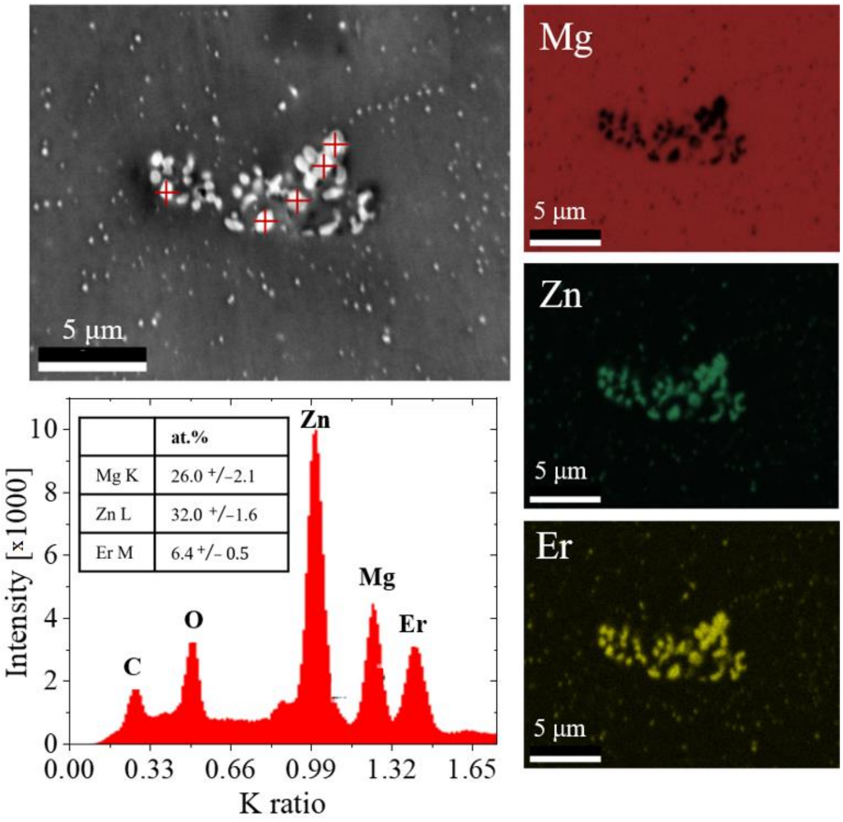

	at.%
Mg K	26.0 +/−2.1
Zn L	32.0 +/−1.6
Er M	6.4 +/− 0.5

Figure 6. EDS analysis of the Er-containing precipitates observed in the Mg-1%Er-1%Zn alloy.

3.2. *Mechanical Properties*

Figure 7a shows the true stress-strain curves of the uniaxial tensile tests in RD, 45° and TD for the investigated alloys annealed at 400 °C for 15 and 60 min, respectively. The samples of both alloys exhibited a similar annealing grain size (hence the different times) but a drastically different texture (Figure 7b). As evident from the flow curves, the addition of zinc leads to higher ductility, as well as an increase of the ultimate tensile strength, which are indicative of an enhanced work hardening capability.

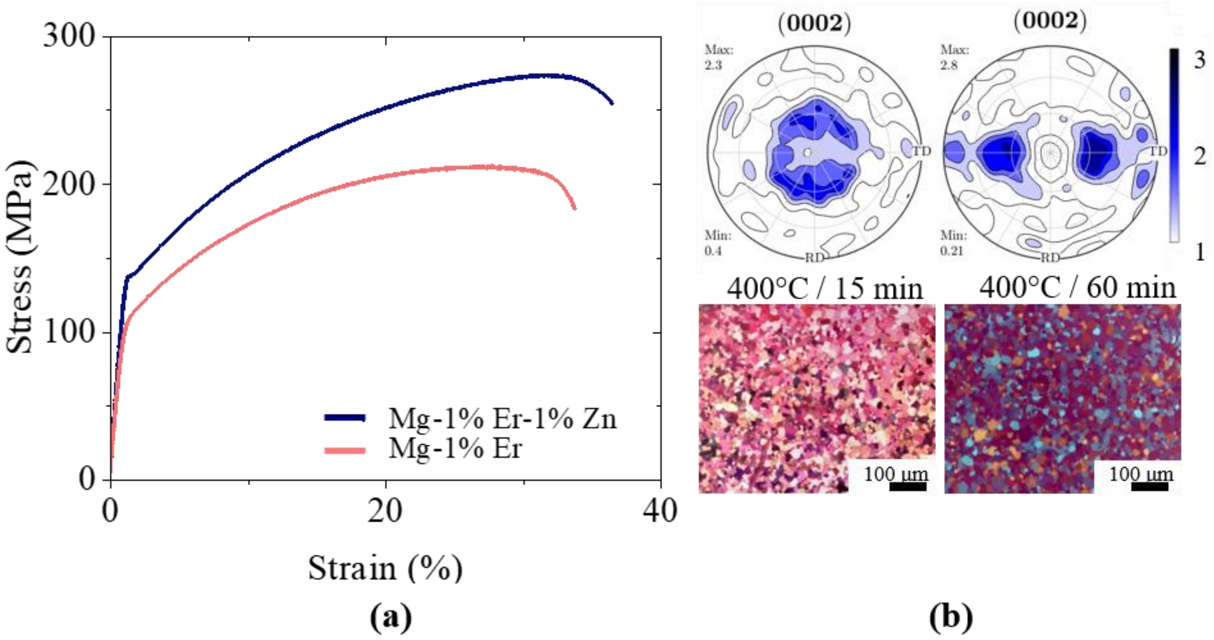

Figure 7. Uniaxial stress–strain response (**a**), optical micrographs and (0002) pole figures of Mg-1%Er annealed for 15 min and Mg-1%Er-1%Zn annealed for 60 min at 400 °C (**b**). The grain size prior to the tensile test was in the range of 14 to 16 µm for both samples.

4. Discussion

The present study revealed distinct differences in the microstructure evolution and mechanical properties between a dilute Mg-1%Er alloy with and without the addition of Zn. During annealing, both alloys developed a significant basal pole spread away from the ND. For the ternary alloy, a titanium rolling texture with off-basal components at ±40° TD developed during recrystallization, and was retained during subsequent grain growth. By contrast, the recrystallization texture of the binary alloy with off-basal peaks at ±20° RD was further modified with longer annealing resulting in a much larger grain size and increased texture scatter. The stable grain size in the Mg-1%Er-1%Zn alloy in contrary to the excessive growth in Mg-1%Er can be explained by the presence of a fine particle dispersion and the resulting drag force (Zener drag). This is known to have a significant impeding effect on the grain boundary motion and can therefore lead to a stable grain size [19,20]. Figure 8 shows a BSE image of the observed precipitates in Mg-1%Er-1%Zn after 60 min of annealing at 400 °C and the corresponding particle size distribution. The precipitate characteristics including particle size, volume fraction, and number density are listed in Table 1.

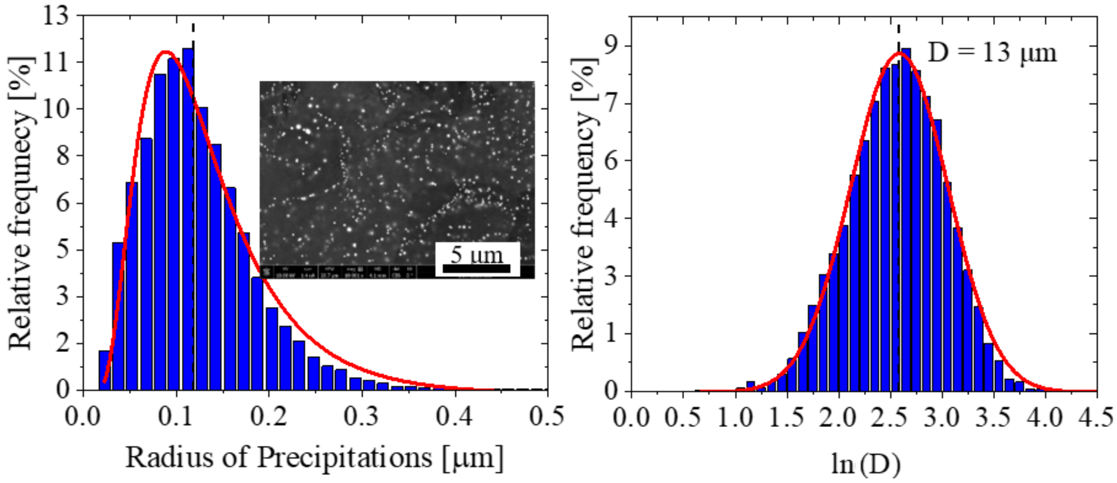

(a) **(b)**

Figure 8. Particle size distribution after 60 min of annealing at 400°C visualized using a histogram with linear *x*-axis (**a**) and the corresponding grain size distribution obtained by optical microscopy (**b**).

The critical grain size according to classical Zener theory is given by Equation (2), assuming that the radius of curvature equals the critical grain diameter [20].

$$D_c = \frac{4r}{3f} \tag{2}$$

The calculated critical grain size of 12 µm, obtained by using the values in Table 2, is similar to the measured grain size (13.28 µm) under the same annealing conditions (cf. Figure 8b). This supports the assumption made earlier that the fine precipitates stabilize the recrystallization microstructure during annealing. Similarly, the absence of precipitates in the binary alloy (Mg-1%Er) could explain the excessive growth rate observed after an initial slow growth stage during the first 15 min of annealing (cf. Figure 3). The drag force during this short stage is believed to be caused by solutes inhibiting the motion of grain boundaries [21–23], which were obviously able to break free after 15 min annealing time. Theoretical studies revealed that accelerated grain growth in a system under the influence of solute pinning will occur when the average grain size becomes close to the critical grain size for which the solute drag force and the capillary driving force are equal. Such state allows the pinned boundaries with a slightly higher curvature than the average to break free from their solute atmosphere, while the other boundaries remain pinned [24]. This seems to be in accordance with the observed growth behavior of the Mg-1%Er alloy and the resulting growth of non-basal texture components (cf. Figure 5b) after a critical grain size has been reached.

Table 2. Characteristics of the Er and Zn-containing precipitates in Mg-1%Er-1%Zn obtained by means of statistical analysis of BSE images

Volume Fraction f:	0.0131
Average Particle Size r:	0.122 µm (from dist. 0.1178)
Number density:	0.2246 $1/\mu m^2$

In the ternary alloy, the process of recrystallization was responsible for the RD → TD transition of the basal pole spread seen in Figure 4, which can be contributed to either oriented nucleation or selective nucleus growth. Selective growth of texture components can be caused by anisotropic segregation behavior and/or an equalization of different grain boundary mobilities annihilating a prior growth advantage of certain orientations, e.g., of basal oriented grains as suggested by Barrett et al. [25]. Figure 9 presents EBSD maps (ND-IPF) of the microstructure of the ternary alloy at 5 and 10 min annealing at 350 °C. The orientation of recrystallized grains was evaluated separately from the orientation of the overall microstructure in order to discern the effect of recrystallization on the development of the ±40° TD texture. For this, the common criterion of grain orientation spread (GOS) was used, where recrystallized grains typically depicted GOS < 1°. The overall texture revealed that the RD-tilted components were a feature of the deformation microstructure. They did not exist in the recrystallization texture that was solely composed of the TD-tilted components, readily after 5 min of annealing (Figure 9a). After completion of recrystallization at 10 min of annealing, the RD-tilted components were no longer a feature of the overall texture that was only dictated by the TD- recrystallization texture (cf. Figure 9b).

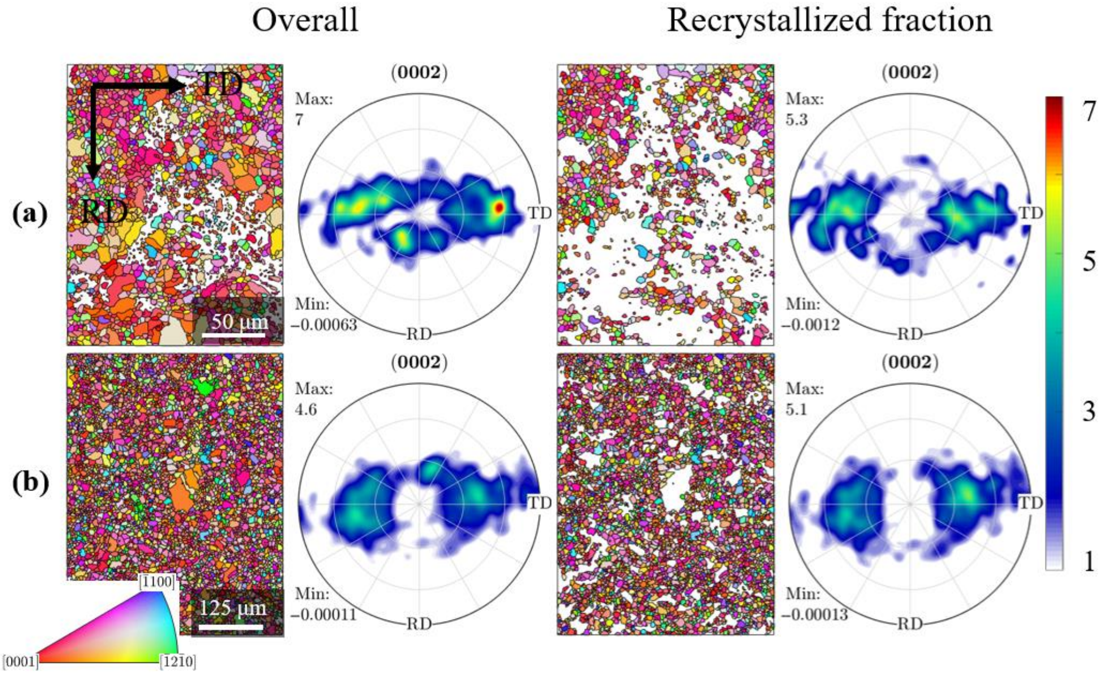

Figure 9. EBSD IPF maps (with respect to ND) and their (0002) pole figures of Mg-1%Er-1%Zn annealed at 350 °C for 5 min (**a**) and 10 min (**b**). The left column features the overall map data, and the right column only the recrystallized fraction with GOS < 1°.

Additional grain size vs. texture analysis of the recrystallized structure in Figure 9b (400 °C/10 min) revealed that the ±40° TD texture in the ternary alloy intensifies during recrystallization growth of the nuclei. A similar effect was not observed in the binary system (Figure 10b), as no significant size dependence of texture during recrystallization was found. While there was a progressive texture change in the binary alloy during annealing, which involved both recrystallization and grain growth, the texture change in the counterpart ternary alloy was much more rapid, and in that regard, limited to recrystallization. As the drag force exerted by particles of a given size and volume fraction is too small to match the capillary driving force of grains significantly smaller than the critical grain size D_c, particle pinning should only play a minor role during recrystallization and early grain growth. Accordingly, selective growth at the recrystallization stage is likely to be governed by solutes. In comparison to the binary alloy, specific boundaries in the ternary alloy seem to break free from their solute atmosphere much sooner enabling texture selection readily during recrystallization. This may be a result of a lower solute content due to the large amount of fine Er/Zn-rich precipitates, whereas in the binary alloy the Er content is fully dissolved in the matrix.

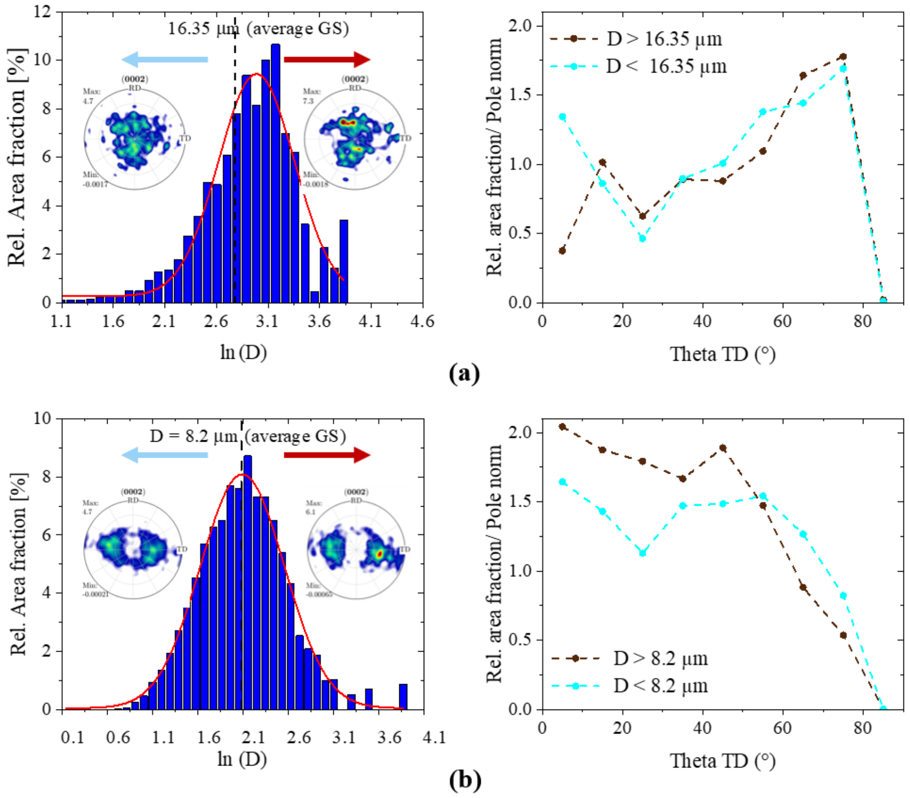

Figure 10. Grain size distributions from EBSD measurements of Mg-1%Er annealed at 400 °C for 4 min (**a**) and Mg-1%Er-1%Zn annealed at 350 °C for 10 min (**b**) along with the orientation distribution of the c-axis with respect to TD for small and large recrystallized grains. The threshold used in each case was the average grain size obtained from EBSD.

The observed recrystallization kinetics of the two alloys further indicates a difference in the drag force during recrystallization. Figure 11 shows the recrystallized volume fraction as a function of annealing time and the corresponding JMAK (Johnson-Mehl-Avrami-Kolmogorow) fit for both Mg-1%Er and Mg-1%Er-1%Zn alloys. A Comparison of the recrystallization curves reveals a quicker recrystallization in the ternary alloy (~210 s) compared to the counterpart binary alloy (~500 s). Additionally, the initial stage (linear portion of the curve) until the onset of stable nuclei growth is extended in Mg-1%Er compared to the other alloy, indicating a longer incubation time in the first. As the incubation time is related to reduced boundary mobility, a stronger solute drag effect in Mg-1%Er may cause a longer incubation period.

Mg-1%Er-1%Zn exhibited an elevated yield strength, strain hardening capability, and failure ductility. The elevated yield stress is partially caused by precipitation hardening, which contributed by approximately 5 MPa to the 20 MPa offset (approximation by Orowan). Furthermore, the addition of zinc might have magnified the impact of solid solution strengthening by means of synergetic solute effects. To investigate the role of texture and microstructure in the activation of deformation modes during tension, EBSD-assisted slip trace analysis of at least 120 grains per strained sample was employed in the current study. A slip trace appears as a straight line as a result of the intersection of an active slip plane with the free surface. Figure 12 shows the frequency of slip traces corresponding to the active slip systems during 5% tension in RD, for the binary and ternary alloys. Additionally, the frequency of twinning was evaluated by a visual investigation of each grain. Basal, pyramidal I and <c + a> pyramidal II, as well as $\{10\bar{1}2\}$ tensile twining were detected with almost equal shares of approximately 22% in the ternary system. In the binary alloy, basal slip prevailed with about 64%, while all other slip systems accounted for less than 20% of the overall observed slip traces. A large contribution of basal slip to deformation could justify the lower yield point in the flow curve of the Mg-1%Er alloy.

This is because basal slip, even in rare-earth containing Mg alloys, requires a much lower critical resolved shear stress (CRSS) than non-basal slip [26]. The observed enhanced slip activity on non-basal slip planes in the strained Mg-1%Er-1%Zn sample can be attributed to both a favorable texture and a change of the CRSS ratio between basal and non-basal slip, evoked by the present Zn and Er solutes. The relatively low contribution of prismatic slip to deformation might be attributed to the investigated low strain of 5% being insufficient to activate cross-slip of basal screw dislocations onto the prismatic plane [27,28].

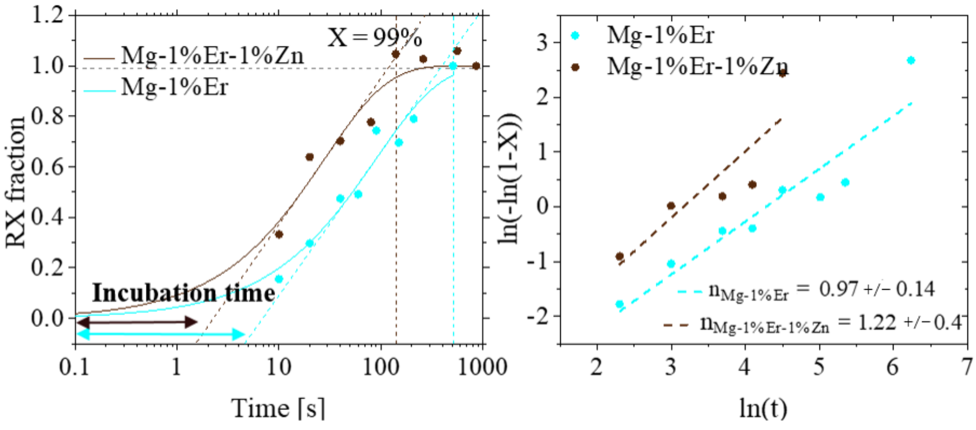

(a) **(b)**

Figure 11. (**a**) Recrystallization kinetics of binary and ternary Mg-1%Er-(1%Zn) annealed at 350 °C and the corresponding Avrami exponents (**b**).

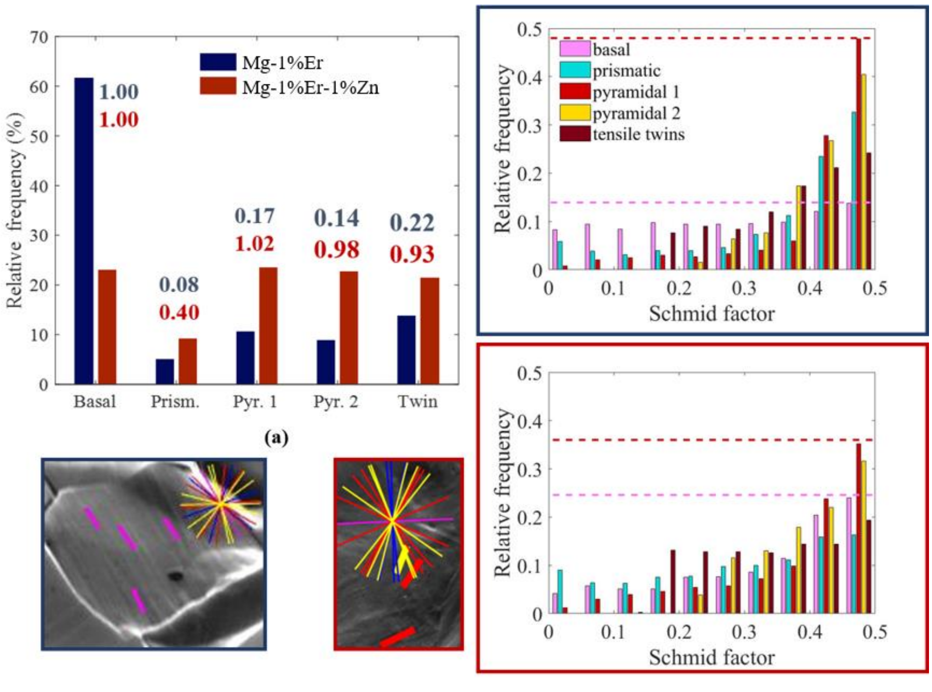

(a)

(b) **(c)**

Figure 12. (**a**) Distribution of slip traces corresponding to the active slip systems in Mg-1%Er and Mg-1%Er-1%Zn during tension to 5% strain. The initial condition of the sample corresponded to annealing at 400 °C for 60 min. (**b**) Exemplary SE images of one grain exhibiting the morphology of slip traces with overlaid possible slip systems obtained from EBSD for the determination of the active slip system. (**c**) Schmid factor distribution calculated from the initial texture of the grains, in which the slip traces were detected in both alloys.

Figure 12 also shows the distribution of Schmid factors (SF) of both alloys with respect to the applied external stress corresponding to different slip traces detected. Generally, non-basal slip (particularly pyramidal) seems to be the main plasticity carrier in both alloys. It also seems to comply principally well with the Schmid law, i.e., corresponding slip traces are preferentially detected in grains with the highest SF, and their frequency drops consecutively with decreasing SF. In the binary alloy, it is evident that the activation of basal slip in grains with a very low SF deviates from the Schmid behavior. This is likely due to the naturally low CRSS of basal slip but also to local stress concentrations at grain boundaries that could cause non-Schmid activation of different slip modes. Another important finding from the SF distribution in Figure 12 is the large difference in the contribution of basal vs. non-basal slip to deformation between the two alloys. In the Mg-Er sample at SF = 0.5, non-basal slip (including prismatic and both <a> and <c + a> pyramidal slip) was ~2–3 times more active than basal slip. In contrast, the level of contribution of these slip modes to deformation at SF = 0.5 in the Mg-1%Er-1%Zn sample was more comparable. Both types of pyramidal slip were still preferential with a frequency ratio of ~1.2–1.5 to basal slip. Prismatic slip was no longer favorable compared to basal slip (frequency ratio of ~0.7).

The present findings certainly highlight the effect of solutes on the deformation behavior, particularly the non-basal slip behavior. There are also indications of solute-induced basal slip strengthening in the current alloys in accordance with previous experimental and computational reports [29–31]. The addition of Zn that alters the substitutional solute chemistry of the Mg-1%Er alloy would obviously lead to complex interaction of solute species within the matrix. From energetic perspectives, Zn and Er can cluster in the lattice to relieve the misfit strains arising from the solute size mismatch. They would also cosegregate to defects in the microstructure, and can be hence expected to have a stronger interaction with grain boundaries and dislocations leading to strikingly different slip system activation during deformation and boundary migration characteristics during annealing. This is indeed demonstrated in the current work by the unique texture development upon rolling and upon annealing of the Mg-1%Er-1%Zn alloy.

5. Conclusions

1. The combination of Zn and Er in a dilute substitutional Mg-1%Er-1%Zn alloy (wt %) led to unique sheet texture development upon rolling and subsequent annealing characterized by pronounced basal pole peaks at ±40° TD. This type of sheet texture is only common for hcp metals with $c/a < 1.633$, such as titanium but was nevertheless observed in the current study.
2. The same texture was not observed in a binary version of the alloy, i.e., Mg-1%Er subjected to similar processing, which suggests that synergetic effects of multiple solute species, in this case Zn/Er, are crucial in terms of providing the ±40°TD orientations for recrystallization nuclei during deformation and their selective growth during subsequent annealing.
3. Mg-1%Er-1%Zn alloy obtained a stable final texture (±40° TD) and grain size (<20 µm) upon completion of static recrystallization. By contrast, the binary Mg-1%Er alloy revealed a continuous modification of its microstructure throughout the annealing process suggesting an important role of grain growth following recrystallization.
4. The microstructural stability of the ternary alloy during longer annealing durations originates from a fine dispersion of dense nanosized particles in the matrix that were found to impede grain growth by Zener drag.
5. Recrystallization nuclei demonstrated selective growth behavior favoring TD-tilted texture components, which was the main mechanism for the ±20° RD → ±40° TD texture transition taking place during recrystallization of the deformed Mg-1%Er-1%Zn alloy. This was likely influenced by solute drag on specific boundaries during early recrystallization.

6. With respect to the mechanical properties in tension, the addition of zinc, the present precipitates, solute strengthening effects and a favorable soft texture led to a remarkable enhancement in the yield strength, strain hardening capability, and failure ductility as compared with the binary Mg-1%Er alloy.
7. EBSD-assisted slip trace analysis at 5% strain unraveled promoted non-basal slip behavior and obvious basal slip strengthening owing to solute/dislocation interaction that requires extended advanced experimental and computational efforts to better understand the interaction of multiple solute species and solute strengthening.

Author Contributions: Conceptualization, F.-Z.M. and T.A.-S.; Methodology, F.-Z.M. and R.P.; Software, R.P.; Validation, F.-Z.M. and F.S.; Formal analysis, F.-Z.M. and F.S.; Investigation, F.S., R.M., and F.-Z.M.; Resources, S.K.-K. and T.A.-S.; Data curation, F.-Z.M. and T.A.-S.; Writing—original draft preparation, F.-Z.M.; Writing—review and editing, T.A.-S.; Visualization, F.-Z.M.; Supervision, S.K.-K. and T.A.-S.; Project administration, T.A.-S. and S.K.-K.; Funding acquisition, T.A.-S. All authors have read and agreed to the published version of the manuscript.

Funding: This research was funded by Deutsche Forschungsgemeinschaft (DFG), grant number grant no. AL 1343/7-1.

Institutional Review Board Statement: Not applicable.

Informed Consent Statement: Not applicable.

Acknowledgments: The financial support of the Deutsche Forschungsgemeinschaft (DFG) under grant no. AL 1343/7-1 is gratefully acknowledged. We also thank Burak Erol for his assistance during the experimental work.

Conflicts of Interest: The authors declare no conflict of interest. The funders had no role in the design of the study; in the collection, analyses, or interpretation of data; in the writing of the manuscript, or in the decision to publish the results.

References

1. Friedrich, H.E.; Mordike, B.L. Technology of Magnesium and Magnesium Alloys. In *Magnesium Technology: Metallurgy, Design Data, Applications*; Springer: Berlin/Heidelberg, Germany, 2006.
2. Gehrmann, R.; Frommert, M.M.; Gottstein, G. Texture effects on plastic deformation of magnesium. *Mater. Sci. Eng. A* **2005**, *395*, 338–349. [CrossRef]
3. Hirsch, J.; Al-Samman, T. Superior light metals by texture engineering: Optimized aluminum and magnesium alloys for automotive applications. *Acta Mater.* **2013**, *61*, 818–843. [CrossRef]
4. Imandoust, A.; Barrett, C.D.; Al-Samman, T.; Inal, K.A.; El Kadiri, H. A review on the effect of rare-earth elements on texture evolution during processing of magnesium alloys. *J. Mater. Sci.* **2016**, *52*, 1–29. [CrossRef]
5. Hadorn, J.P.; Hantzsche, K.; Yi, S.; Bohlen, J.; Letzig, D.; Wollmershauser, J.A.; Agnew, S.R. Role of Solute in the Texture Modification During Hot Deformation of Mg-Rare Earth Alloys. *Metall. Mater. Trans. A* **2011**, *43*, 1347–1362. [CrossRef]
6. Hantzsche, K.; Bohlen, J.; Wendt, J.; Kainer, K.U.; Yi, S.B.; Letzig, D. Effect of rare earth additions on microstructure and texture development of magnesium alloy sheets. *Scr. Mater.* **2010**, *63*, 725–730. [CrossRef]
7. Al-Samman, T.; Li, X. Sheet texture modification in magnesium-based alloys by selective rare earth alloying. *Mater. Sci. Eng. A* **2011**, *528*, 3809–3822. [CrossRef]
8. Robson, J.D. Effect of Rare-Earth Additions on the Texture of Wrought Magnesium Alloys: The Role of Grain Boundary Segregation. *Metall. Mater. Trans. A* **2013**, *45*, 3205–3212. [CrossRef]
9. Barnett, M.R.; Nave, M.D.; Bettles, C.J. Deformation microstructures and textures of some cold rolled Mg alloys. *Mater. Sci. Eng. A* **2004**, *386*, 205–211. [CrossRef]
10. Ball, E.A.; Prangnell, P.B. Tensile-compressive yield asymmetries in high strength wrought magnesium alloys. *Scr. Metall. Mater.* **1994**, 31. [CrossRef]
11. Mackenzie, L.; Pekguleryuz, M. The recrystallization and texture of magnesium–zinc–cerium alloys. *Scr. Mater.* **2008**, *59*, 665–668. [CrossRef]
12. Basu, I.; Al-Samman, T. Triggering rare earth texture modification in magnesium alloys by addition of zinc and zirconium. *Acta Mater.* **2014**, *67*, 116–133. [CrossRef]
13. Jiang, M.G.; Xu, C.; Yan, H.; Lu, S.H.; Nakata, T.; Lao, C.S.; Chen, R.S.; Kamado, S.; Han, E.H. Correlation between dynamic recrystallization and formation of rare earth texture in a Mg-Zn-Gd magnesium alloy during extrusion. *Sci. Rep.* **2018**, *8*, 16800. [CrossRef] [PubMed]

14. Hielscher, R.; Schaeben, H. A novel pole figure inversion method: Specification of theMTEXalgorithm. *J. Appl. Crystallogr.* **2008**, *41*, 1024–1037. [CrossRef]
15. Humphreys, F.J.; Hatherly, M. Recrystallization and Related Annealing Phenomena. In *Recrystallization and Related Annealing Phenomena*; Chapter 9; Elsevier: Amsterdam, The Netherlands, 2004; pp. 285–319. [CrossRef]
16. Lee, H.P.; Esling, C.; Bunge, H.J. Development of the Rolling Texture in Titanium. *Textures Microstruct.* **1988**, *7*, 317–337. [CrossRef]
17. Li, M.R.; Deng, D.W.; Kuo, K.H. Crystal structure of the hexagonal (Zn, Mg)4Ho and (Zn, Mg)4Er. *J. Alloy. Compd.* **2006**, *414*, 66–72. [CrossRef]
18. Fisher, I.R.; Islam, Z.; Panchula, A.F.; Cheon, K.O.; Kramer, M.J.; Canfield, P.C.; Goldman, A.I. Growth of large-grain R-Mg-Zn quasicrystals from the ternary melt (R = Y, Er, Ho, Dy and Tb). *Philos. Mag. B* **2009**, *77*, 1601–1615. [CrossRef]
19. Hadorn, J.P.; Hantzsche, K.; Yi, S.; Bohlen, J.; Letzig, D.; Agnew, S.R. Effects of Solute and Second-Phase Particles on the Texture of Nd-Containing Mg Alloys. *Metall. Mater. Trans. A* **2012**, *43*, 1363–1375. [CrossRef]
20. Humphreys, F.J.; Hatherly, M. Grain Growth Following Recrystallization. In *Recrystallization and Related Annealing Phenomena*; Chapter 11; Elsevier: Amsterdam, The Netherlands, 2004; pp. 333–378. [CrossRef]
21. Lücke, K.; Detert, K. A quantitative theory of grain-boundary motion and recrystallization in metals in the presence of impurities. *Acta Metall.* **1956**, *5*, 628–637. [CrossRef]
22. Hillert, M. Solute drag, solute trapping and diffusional dissipation of gibbs energy. *Acta Mater.* **1999**, *47*, 4481–4505. [CrossRef]
23. Hutchinson, C.R.; Brechet, Y. Solute Drag: A review of the 'Force' and 'Dissipation' approaches to the efffect of solute on grain and interphase boundary motion. In *Termodynamic, Microstructures and Plasticity, Alphonse Finel, Dominique Maziere, Muriel Veron*; Springer: Berlin/Heidelberg, Germany, 2003.
24. Kim, S.G.; Park, Y.B. Grain boundary segregation, solute drag and abnormal grain growth. *Acta Mater.* **2008**, *56*, 3739–3753. [CrossRef]
25. Barrett, C.D.; Imandoust, A.; El Kadiri, H. The effect of rare earth element segregation on grain boundary energy and mobility in magnesium and ensuing texture weakening. *Scr. Mater.* **2018**, *146*, 46–50. [CrossRef]
26. Barnett, M.R. A Taylor Model Based Description of the Proof Stress of Magnesium AZ31 during Hot Working. *Metall. Mater. Trans. A* **2003**, *34*, 1799–1806. [CrossRef]
27. Chino, Y.; Kado, M.; Mabuchi, M. Enhancement of tensile ductility and stretch formability of magnesium by addition of 0.2wt%(0.035at%)Ce. *Mater. Sci. Eng. A* **2008**, *494*, 343–349. [CrossRef]
28. Sandlöbes, S.; Friák, M.; Neugebauer, J.; Raabe, D. Basal and non-basal dislocation slip in Mg–Y. *Mater. Sci. Eng. A* **2013**, *576*, 61–68. [CrossRef]
29. Wang, L.; Huang, Z.; Wang, H.; Maldar, A.; Yi, S.; Park, J.-S.; Kenesei, P.; Lilleodden, E.; Zeng, X. Study of slip activity in a Mg-Y alloy by in situ high energy X-ray diffraction microscopy and elastic viscoplastic self-consistent modeling. *Acta Mater.* **2018**, *155*, 138–152. [CrossRef]
30. Wu, J.; Si, S.; Takagi, K.; Li, T.; Mine, Y.; Takashima, K.; Chiu, Y.L. Study of basal <a> and pyramidal <c + a> slips in Mg-Y alloys using micro-pillar compression. *Philos. Mag.* **2020**, *100*, 1–22. [CrossRef]
31. Tehranchi, A.; Yin, B.; Curtin, W.A. Solute strengthening of basal slip in Mg alloys. *Acta Mater.* **2018**, *151*, 56–66. [CrossRef]

7.2 Synergistic Effects of Solutes on Active Deformation Modes, Grain Boundary Segregation and Texture Evolution in Mg-Gd-Zn Alloys.

F. Z. Mouhib[1], R. Pei[1], B. Erol[1], F. Sheng[1], S. Korte-Kerzel[1] and T. Al-Samman[1].
[1]Institute of Physical Metallurgy and Materials Physics, RWTH Aachen University, Germany

Materials Science and Engineering: A 847 (2022), p. 143348. issn: 0921-5093.

The candidate carried out the conceptualisation, participated in the experimental work, guided and performed data analysis and did writing and editing of the manuscript.

Online availability: https://doi.org/10.1016/j.msea.2022.143348

Materials Science & Engineering A 847 (2022) 143348

Contents lists available at ScienceDirect

Materials Science & Engineering A

journal homepage: www.elsevier.com/locate/msea

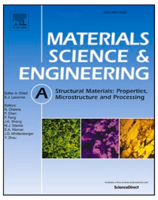

Synergistic effects of solutes on active deformation modes, grain boundary segregation and texture evolution in Mg-Gd-Zn alloys

F. Mouhib [*], R. Pei, B. Erol, F. Sheng, S. Korte-Kerzel, T. Al-Samman

Institute of Physical Metallurgy and Materials Physics, RWTH Aachen University, Aachen, 52056, Germany

ABSTRACT

Synergistic effects of rare earth elements (RE) and Zn have a major impact on the properties of ternary Mg-RE-Zn alloys. This study illuminates their dependence on the solute ratio by comparing texture evolution, solute segregation, and active deformation modes of three Mg-Gd-Zn alloys with a varying Gd:Zn ratio of 2:1, 1:1 and 1:2. A low Gd:Zn ratio led to a texture featuring a pronounced TD-tilted basal pole spread alongside a magnified solute segregation at grain boundaries, indicating a significant impact of solute-boundary interactions on RE-texture formation. Atom probe tomography revealed major alterations of the segregation energy of both Gd and Zn, depending mainly on the solute ratio rather than the absolute solute concentration. Additionally, the alloy with the smallest Gd:Zn ratio, i.e. Gd:Zn = 1:2, showed the highest direction dependent anisotropy of the yield stress under tensile strain, which was attributed to a magnified anisotropy of twinning depending on the Gd:Zn ratio. EBSD assisted slip trace analysis showed that the occurrence of non-basal slip systems could be increased by reducing the Gd:Zn ratio. Synergistic solute effects were found to be crucial for the activation of non-basal slip, solute segregation, as well as the formation of RE-texture components and proven to be highly sensitive to the solute ratio.

1. Introduction

Informed materials design relies on precise microstructural predictions, which require a deep understanding of texture formation and its underlying mechanism. As of late, increasing research efforts have been employed to tailor materials properties by influencing deformation modes and grain boundary properties [1–4]. Many material systems form specific texture components upon thermomechanical processing as a result of deformation, recrystallization and grain growth processes [5,6]. In the case of magnesium alloys, formation of sharp basal-type textures during primary fabrication processes limits the formability of magnesium sheets and extrusions at low temperatures, which leads to high production costs if processing is to be carried out at elevated temperatures. This is mainly attributed to limited activity of non-basal slip modes at low temperatures [7,8]. Additionally, anisotropic grain boundary (GB) energy and mobility are assumed to lead to an intensification of the basal texture [5]. For example, the low energy and high mobility of 30° 0001 grain boundaries were found to further sharpen the texture during recrystallization [5,9].

One of the most prominent methods to weaken the basal texture in magnesium alloys, and thereby enhance cold formability, is by intelligent micro-alloying [10–12]. In particular, alloys containing rare earth (RE) elements show remarkable alterations of the sheet texture, characterized by an off-basal pole spread, and superior mechanical properties [10,11]. Former research focused mainly on mechanisms able to promote randomly orientated recrystallization nuclei, such as deformation twinning, shear banding and particle stimulated nucleation [13]. However, those mechanisms were frequently observed in non-RE alloys [14–16] and RE-texture components already emerge in dilute alloys with very small solute concentrations [17–19]. This raises the interest in solute-defect interactions and their impact on deformation modes and grain boundary motion, as they may be the key to unravelling the origin of the RE-texture.

In terms of deformation mechanisms, RE elements were found to promote the activation of non-basal slip, including pyramidal II $c + a$ slip, possibly by basal slip strengthening [20–23]. This can be further enhanced by combined additions of RE and Zn [17,24] Additionally, a modified behavior in the activation of tensile twinning as a mechanism for local strain accommodation in Mg-RE-Zn alloys was observed frequently in prior research [25,26]. Results from Nie et al. show that solute segregation of Gd and Zn to twin boundaries will alter their properties affecting twin activation and stability in ternary Mg-RE-Zn alloys [27] What has been so far established is that RE-solutes preferentially segregate to grain boundaries due to their large size misfit within the Mg-matrix, and therefore influence the grain boundary mobility [13,28–31]. Prior studies explored a connection between RE-solute segregation and selective growth of specific orientations during recrystallization and subsequent grain growth [9,17,18]. The

---

* Corresponding author.
E-mail address: mouhib@imm.rwth-aachen.de (F. Mouhib).

https://doi.org/10.1016/j.msea.2022.143348
Received 24 February 2022; Received in revised form 19 May 2022; Accepted 24 May 2022

effects of RE solutes on grain boundaries discussed in the available literature include solute drag effects, as well as energetic and structural alteration of the grain boundary character by solutes [17,27,29,32,33].

The combination of RE-elements with other solute species, namely Zn, leads to further texture softening, which was attributed to co-segregation. Particularly, the prevalence of uncommon sheet texture components tilted towards the transvers direction was found to be specific for Mg-RE-Zn alloys compared to binary Mg-RE alloys [17,18,27,34,35]. However, the underlying synergistic effects are far from being sufficiently understood and the ideal solid solution composition to maximize their efficiency has not been yet systematically studied. A fundamental understanding of the joined impact of solutes of different species on grain boundary mobility is a key requirement to control the microstructure and texture and might therefore be the gateway to informed design of next generation Mg sheet alloys.

The importance of the active deformation modes alongside with the grain boundary properties for microstructural evolution is undeniable, yet the impact of combined solute effects on those is not sufficiently characterized in the current state of the art. This study aims at understanding the synergistic effects in lean Mg-Gd-Zn alloys on microstructure evolution and mechanical properties by performing a systematic comparison of texture evolution, solute segregation behavior, and the active deformation modes as a function of varying Gd:Zn ratios in the alloy composition.

2. Experimental

Binary Mg–Gd and three Mg-Gd-Zn alloys with varying Gd:Zn ratios of 2:1, 1:1 and 1:2 were chosen for the study. For future reference, the Zn fraction with respect to the total solute concentration calculated after Eq. (2.1)was used as a parameter for comparison and distinction (see Tab 1).

$$Zn_{frac} = \frac{c_{Zn}}{c_{Zn} + c_{Gd}}. \qquad \text{(Eq. 2.1)}$$

The chemical composition of the investigated alloys was measured by ICP/OES and summarized in Table 1. All alloys were melted under an Ar/CO_2 gas atmosphere in an induction furnace, casted into a pre-heated copper mold and homogenized at 460 °C for 960 min.

Sheets of the dimensions $60 \times 40 \times 4$ mm^3 were hot rolled at 400 °C up to a thickness reduction of 80% with multiple rolling passes. Only the final rolling pass was performed at 200 °C to refine the microstructure. Subsequently, rectangular samples (10 x 12 × 1 mm^3) were cut from the rolled sheets and subjected to annealing heat treatments at 400 °C in a Heraeus RL200E air furnace for prolonged annealing (60 and 1440 min), and in a sand bath furnace for recrystallization experiments at 370 °C of shorter times (10–5000 s). The initial sample preparation was done by mechanical grinding to the sample mid-plane and subsequent polishing with a diamond suspension up to 0.25 μm. Samples assorted for EBSD measurements were additionally electro-polished for 120 s at a voltage of 25 V and −20 °C using a Lectro-Pol 5 in a Struers AC-2 solution. For optical light microscopy, samples were electro-polished in a 5:3 ethanol H_3PO_3 solution for 40 min at 2 V and subsequently etched in an acetic picral solution. Texture characterization was conducted by XRD measurements of six incomplete pole figures [$\{10\bar{1}0\}$, $\{0002\}$, $\{10\bar{1}1\}$, $\{10\bar{1}2\}$, $\{11\bar{1}0\}$, $\{10\bar{1}3\}$] using a Bruker D8 advance diffractometer. Full pole figures and orientation distribution functions (ODFs) were calculated with the texture analysis toolbox MTEX [36]. EBSD measurement were performed using a focused ion beam Helios 600i operating at 20 kV equipped with an HKL-Nordlys II EBSD detector. The detection step size varied depending on the grain size in a range from 0.5 to 1.5 μm. The raw data from EBSD measurements were analyzed using the texture analysis toolbox MTEX [36].

Table 1
Chemical composition in atomic percentage of Mg–Gd and the three Mg-Gd-Zn alloys.

Alloys	Gd (at %)	Zn (at %)	Gd:Zn	Rel. Zn (%)
Mg-x%Gd	0.142	/	/	0
Mg-x%Gd-y%Zn	0.15	0.086	2:1 (1.74:1)	36
Mg-x%Gd-y%Zn	0.148	0.165	1:1 (1:1.15)	53
Mg-x%Gd-y%Zn	0.073	0.165	1:2 (1:2.26)	69

Recrystallization (RX) kinetics were determined by the measurement of the Vickers micro-hardness during interrupted annealing at 370 °C up to an annealing time of 5000 s. The average micro-hardness HV_t for a time step t was calculated from 15 indentations for each time step. Eq. (2.1) was used to calculate the recrystallized fraction from previously determined hardness values. $HV_{initial}$ and HV_{final} denote the initial and final hardness, respectively [37].

$$X = \frac{HV_{initial} - HV_t}{HV_{initial} - HV_{final}} \qquad \text{(Eq. 2.2)}$$

The evaluation of three-dimensional element distribution in the vicinity of grain boundaries was conducted by atom probe tomography using a LEAP 4000X HR Cameca Instrument operating at −30 °C equipped with an ultra-violet laser with a wavelength of 355 nm maintaining a constant evaporation rate of 0.5%. The applied pulse energy was 30 pJ and the repetition rate 125 kHz. Prior site-specific atom probe tip preparation, schematically shown in Fig. 1, was performed by Transmission Kikuchi diffraction (TKD)-assisted tip milling using a Ga + ion source. Grain boundaries were selected by SE/BSE-imaging and prior EBSD mapping and marked with a protective platinum layer (Fig. 1 a, b). A wedge-shaped lift out containing the grain boundary was sliced and mounted on silicon posts with a diameter of 2 μm. APT tips were subsequently milled in several steps with decreasing milling radii (from 1.5 to 0.1 μm) and beam currents (from 0.43 nA to 40 pA) assisted by TKD to ensure the presence of a boundary and confirm the orientation of the adjacent grains (Fig. 1 c, d). Samples assorted for APT were subjected to 60 min of annealing at 400 °C beforehand.

The mechanical properties of ternary Mg-Gd-Zn were determined by uniaxial tensile tests and EBSD-assisted slip trace analysis. Dog-bone-shaped samples with gauge dimensions of 5 mm × 1.5 mm x 0.8 mm were annealed at 400 °C for 3600 s for all three ternary alloys. Uniaxial tensile tests were conducted at room temperature up to failure using a ZWICK tension-compression testing machine under a constant strain rate of $2x10^{-4}$. Tensile tests for each alloy were performed along the rolling direction (RD) and in transvers direction (TD) on fully recrystallized samples. To ensure reproducibility, each tensile test was performed three times and the average flow curve was considered for the analysis. For the analysis of the active slip systems, interrupted tensile tests were performed up to 5% strain on all ternary alloys in RD as well as for Mg-Gd-Zn 1:2 in TD, as this alloy showed a pronounced RD-TD anisotropy. The slip systems were determined for each alloy by a comparison of slip lines from SE images of at least 80 grains and the corresponding grain orientation from EBSD IPF maps.

3. Results

3.1. Microstructure evolution

Fig. 2 shows optical micrographs of all three analyzed ternary Mg-Gd-Zn alloys in the as cast state, after rolling and subsequent annealing for 1440 min at 400 °C, respectively. Despite a different Gd:Zn ratio, the microstructure evolution as shown by the optical micrographs appeared to be alike. The rolling microstructures exhibited numerous deformation twins that could act as potential nucleation sites for recrystallization [38]. The final microstructures after 24 h of annealing were relatively homogeneous and the grain size was found to be 77.8 μm, 72.5 μm and 76.2 μm for Mg-Gd-Zn 2:1, 1; 1 and 1:2, respectively. Apart from a few irregularly distributed micro-scale precipitates, no

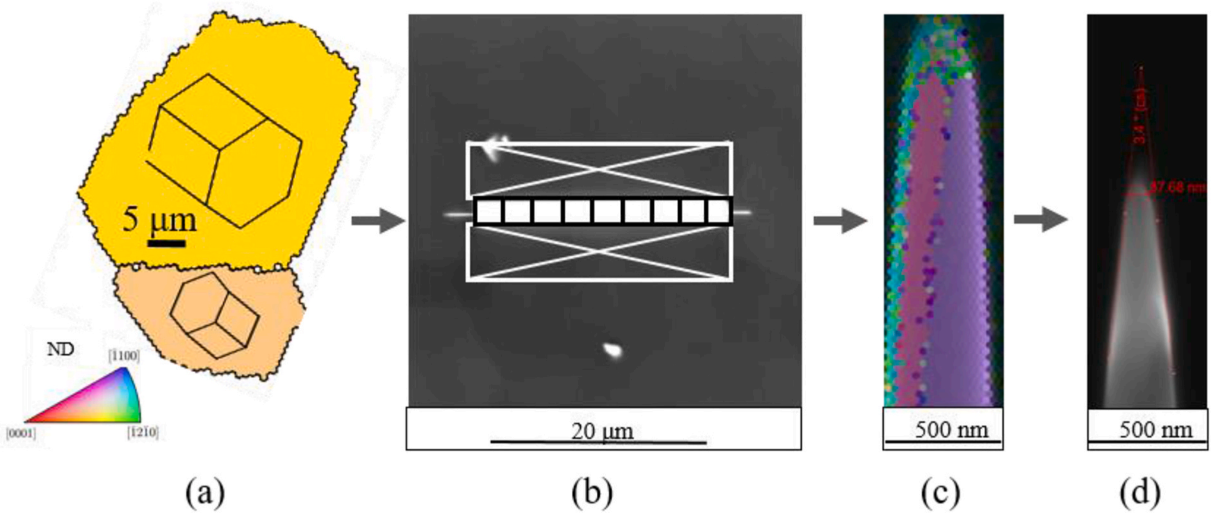

(a) (b) (c) (d)

Fig. 1. Schematic image of APT-tip preparation. (a) IPF image from EBSD of the grains adjacent to the selected grain boundary. (b) SE image of the grain boundary covered by a protective platinum layer. The white boxes mark the region for the Ga-ion beam cutting step. (c) IPF map from TKD measurements of the APT tip during milling. (d) SE image of the final APT tip.

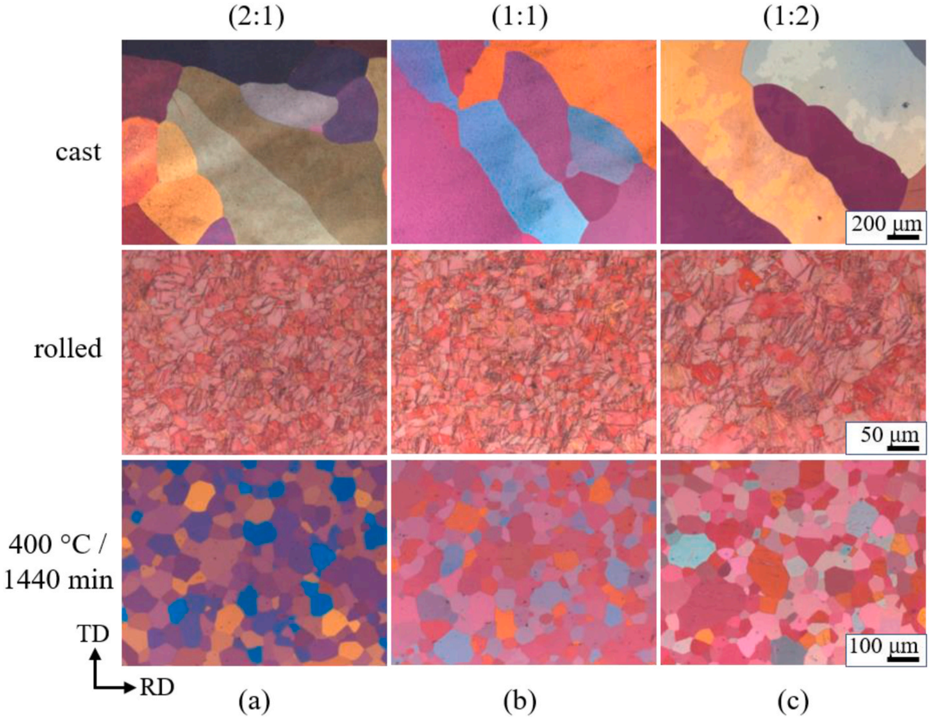

Fig. 2. Optical micrographs of Mg-x at. % Gd-y at. % Zn with a Gd:Zn ratio of 2:1 (a), 1:1 (b) and 1:2 (c) respectively. The as cast state (top row), rolled (middle row), and annealed at 400 °C for 1440 min (bottom row).

obvious precipitation was observed in all investigated alloys. Thus, the impact of precipitates on microstructure evolution could be neglected in the scope of this study.

The rolling texture of binary and all ternary Mg-Gd-Zn alloys shown in Fig. 3 exhibited a basal pole split towards the rolling direction. However, in addition to the predominant pole split in rolling direction, the ternary alloys showed a slight spread towards the transverse direction. During subsequent annealing for 60 min at 400 °C, the binary alloy underwent a significant texture weakening but maintained a pronounced spread of the basal poles towards RD, whereas the ternary Mg-Gd-Zn alloys with their different Gd:Zn ratios revealed a more significant qualitative alteration of the deformation texture. This can be characterized by an off-basal pole distribution about the normal direction. Depending on the alloy composition, this off-basal orientation distribution was seen to either form a ring of almost uniform pole densities (Gd:Zn ratio of 2:1) or a clear double peak texture with TD-tilted poles at approx. ±40° and almost no remaining RD tilted components (Gd:Zn ratio of 1:2). For the intermediate case with a Gd:Zn ratio of 1:1, the tendency of developing a TD split with increasing relative Zn amount was evident.

This unique TD-tilted annealing texture was formed already upon recrystallization. To analyze the recrystallization kinetics, the recrystallized volume fraction was calculated from the Vickers hardness as a function of the annealing time. The evolution of the Vickers hardness

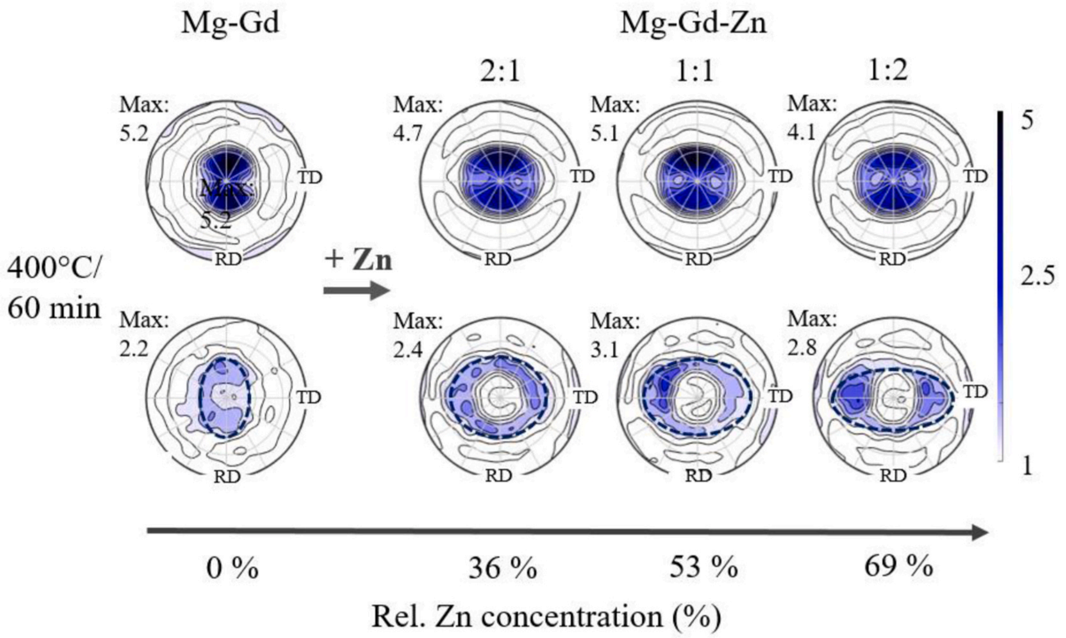

Fig. 3. Texture of binary Mg- 0.14 at. % Gd and Mg-x at. % Gd- y at. % Zn with a Gd: Zn ratio of 2:1, 1:2 and 2:1 respectively, after rolling (top) and upon 60 min of annealing at 400 °C (bottom). The marked area in each annealing pole guides the eye of how the texture character is changing as a function of the relative Zn fraction with respect to the overall solute concentration.

with the annealing time was similar for all alloys, however the absolute hardness values of the alloy with Gd:Zn = 1:1 were significantly larger in comparison to the other alloys. This is probably caused by the larger absolute solute concentration and the resulting solid solution strengthening effect [39].

Fig. 4 exhibits the recrystallized volume fraction as a function of the annealing time for all three ternary alloys annealed at 370 °C, along with the corresponding JMAK fit and (0002)-pole figures for a recrystallized volume fraction X of 0%, 50% and 100%. The texture of the partially recrystallized samples (at X = 50%) already shows an increasing TD spread depending on the alloy composition. The final textures corresponding to full recrystallization were similar to the ones shown in Fig. 3 for a longer annealing time. The incubation time, identified by the intersection between the x-axis and an extension of the linear fraction of the curve (here tangential lines), before the onset of stable nuclei growth was found to be at least 2 times larger in Mg-Gd-Zn 1:2 compared to the other two alloys. This indicates a stronger solute drag effect, as the incubation time is associated with the retardation of recrystallization by solute drag. Fig. 4 (a) additionally shows the linear fit of ln(-ln(1-X)) over the annealing time and the resulting Avrami-exponents. Mg-Gd-Zn 1:1 and 1:2 show two different growth regimes as they could be well fit by two lines.

To examine the influence of alloy composition on the grain size distribution, EBSD analysis of the investigated alloys was carried out after 60 min of annealing at 400 °C. The results are presented in Fig. 5 in terms of inverse pole figure (IPF) maps with respect to the sheet normal direction (ND) and log normal grain size distributions. Noteworthy is that the Zn-containing alloys have a broader spectrum of grain orientations and that the Mg-Gd-Zn 1:1 alloy shows the finest grain size. Correspondingly, its size distribution is characterized by the highest

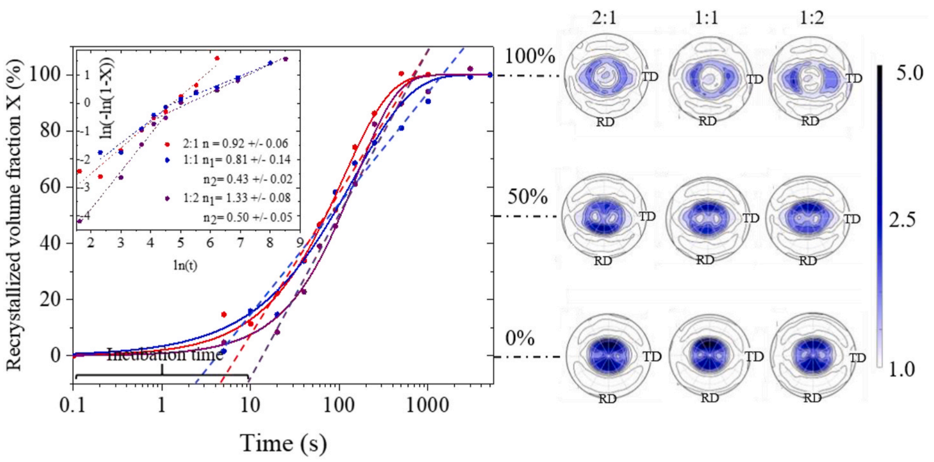

(a) (b)

Fig. 4. Texture evolution during recrystallization of Mg-x at. % Gd-y at. % Zn with a varying Gd:Zn ratio of 2:1 (red), 1:1 (blue) and 2:1 (violet), respectively and the corresponding Avrami exponents (top left corner) (a). The texture is represented by means of (0002)-pole figures obtained for 0, 50 and 100% recrystallized volume fraction (b). (For interpretation of the references to color in this figure legend, the reader is referred to the Web version of this article.)

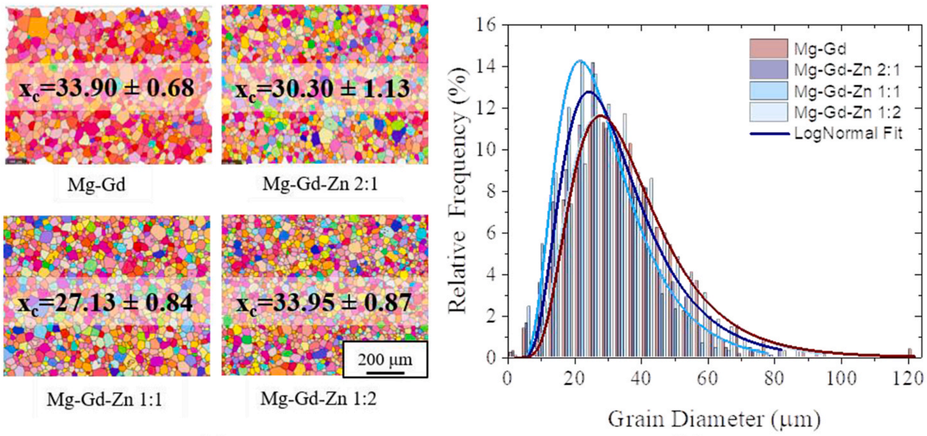

(a) (b)

Fig. 5. IPF-ND maps from EBSD data after 60 min of annealing at 400 C of Mg–Gd, Mg-Gd-Zn 2:1, 1:1 and 1:2 (a), as well as the corresponding grain size distributions fitted with log normal (b).

frequency peak at small grain diameter and the shortest tail at large grain diameter. This is possibly caused by the higher absolute solute content in that alloy.

Additionally, a significant difference in the character of grain boundary distribution caused by the addition of Zn. Fig. 6 shows the distribution of the grain boundary misorientation angle for the investigated alloys in comparison with the theoretical Mackenzie distribution for a perfectly random polycrystal.

The binary alloy exhibited a frequency peak around 30°–40°, which is a common feature in conventional Mg alloys without RE additions [5]. All of the ternary alloys, on the other hand, showed a broader angle distribution, featuring an obvious increase of grain boundaries with higher angles. Additionally, the grain boundary distribution in the ternary alloys was remarkably similar to the theoretical random distribution, which indicates that there were no preferences for particular misorientation relationships between neighboring crystals.

3.2. Solute segregation to grain boundaries

The observed large fraction of high angle grain boundaries at 60° and higher (cf. Fig. 6 (b)) is specific to the Zn containing alloys and therefore a further investigation to evaluate the influence of Zn additions on the microstructure is required. For this purpose, one high angle grain boundary with an angle between 80 and 90° for each alloy was analyzed regarding the chemical composition by means of atom probe tomography. A cylindrical volume with a z-axis perpendicular to the grain boundary plane was selected for each tip and the element concentration within the cylinder along its z-axis was evaluated. The results are presented in Fig. 7. The figure shows the spatial distribution of the present elements from a side view of the grain boundary plane, the corresponding grains and their orientation, as well as the elemental concentration of Mg (light blue), Gd (green) and Zn (grey) as a function of the distance from the grain boundary for each alloy, respectively. Binary Mg–Gd (Fig. 7 (a)) exhibits the smallest solute concentration at the boundary, approx. 0.5 at %, compared to the ternary alloys (Fig. 7 (b–d)). In the case of the ternary alloys the concentration of Zn increases with a decreasing Gd:Zn ratio, hence Mg-Gd-Zn 2:1 exhibits the smallest Zn concentration at the boundary and Mg-Gd-Zn 1:2 the largest. The Gd concentration at the boundary behaves similarly, i.e. it increases gradually for binary Mg–Gd, ternary Mg-Gd-Zn 2:1 and 1:1. Interestingly, the Mg-Gd-Zn 1:2 and Mg-Gd-Zn 1:1 boundaries had a very similar Gd content, which will be addressed in the discussion section.

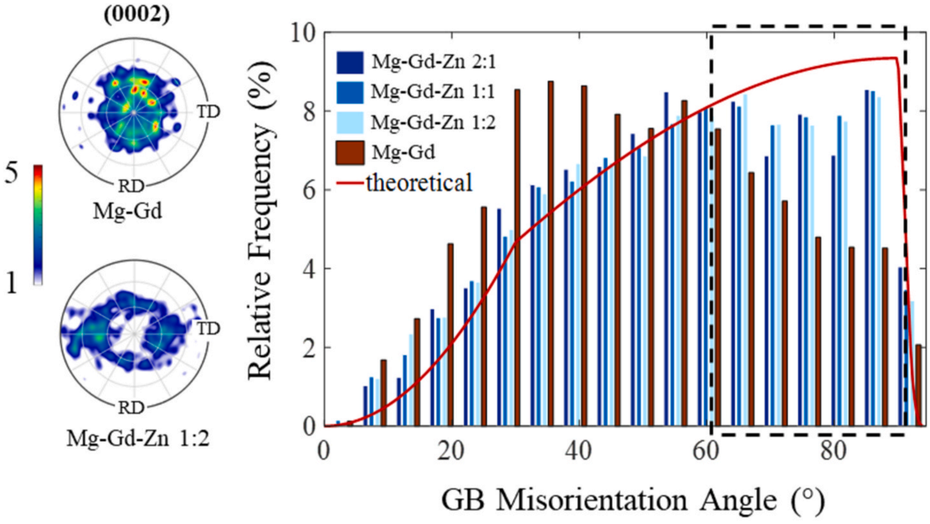

(a) (b)

Fig. 6. (0002) pole figures of binary Mg–Gd and ternary Mg-Gd-Zn with a Gd:Zn ratio of 2:1 (a) and the grain boundary misorientation distribution of Mg–Gd and three Mg-Gd-Zn alloys with varying Gd:Zn ratio (b) after 60 min of annealing at 400 °C obtained from EBSD.

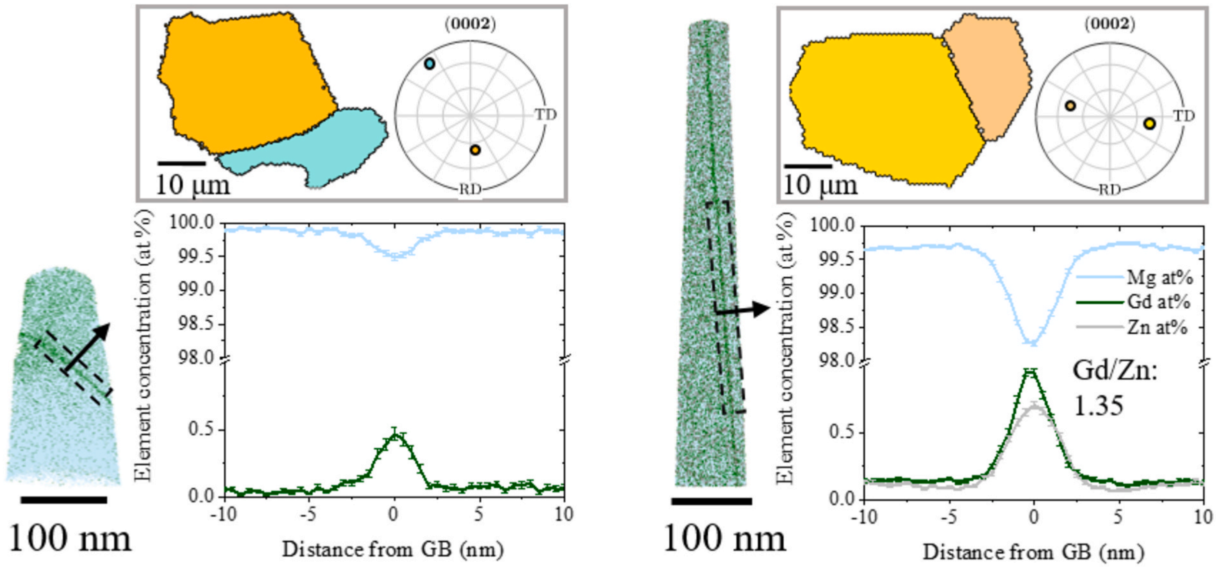

(a) Mg-Gd

(b) Mg-Gd-Zn 2:1

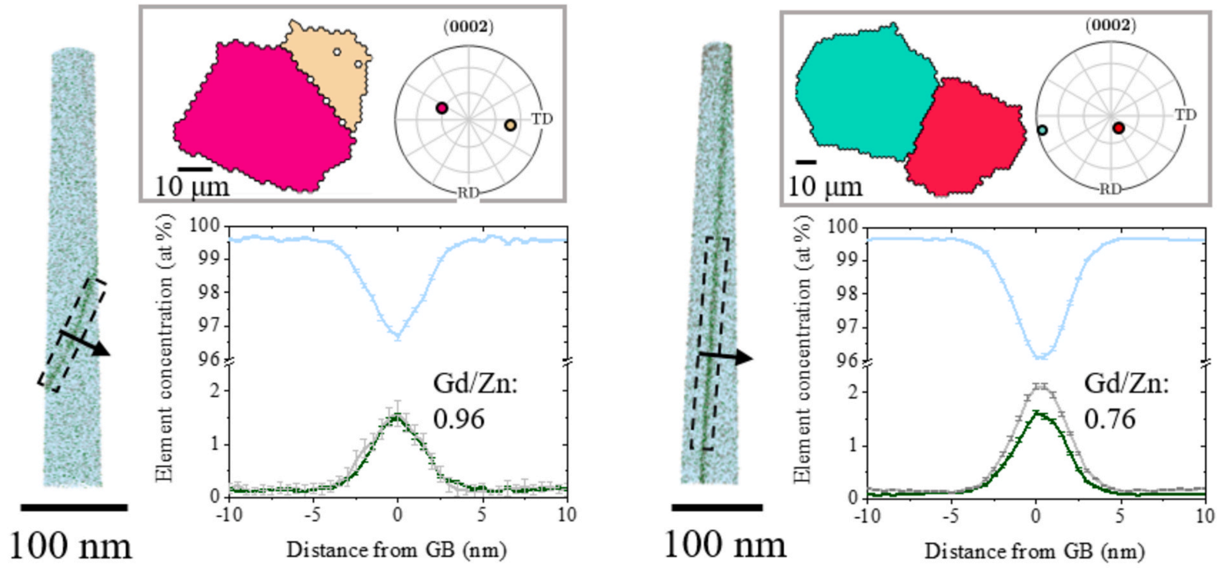

(c) Mg-Gd-Zn 1:1

(d) Mg-Gd-Zn 1:2

Fig. 7. Atomic reconstruction of a high angle grain boundary from atom probe tomography. The corresponding initial grains and their orientations are presented in terms of ND-IPF coloring and (0002) pole figures. The elemental distribution profiles were obtained in the region of interest (dashed rectangle) across the grain boundary of Mg–Gd (a) and Mg-Gd-Zn with a Gd:Zn ratio of 2:1 (b), 1:1 (c) and 1:2 (d). The given Gd/Zn ratios in the concentration profiles correspond to the peak concentrations of both solute elements at the grain boundary.

3.3. *Mechanical properties*

Fig. 8 (a) shows the uniaxial stress-strain response of all three Mg-Gd-Zn alloys (annealed at 400 °C for 60 min) loaded in tension in the rolling (RD) and transvers directions (TD), respectively. Table 2 provides a summary of the tensile properties of all investigated ternary Mg-Gd-Zn alloys. The stress-strain behavior of a binary Mg–Gd alloy under similar testing conditions can be found in a previous publication [10]. All three alloys exhibited a similar initial grain size, which helps exclude the role of grain size in any observed differences in the yield strength. Depending on the testing direction, the yield strength (YS) was seen to vary, demonstrating planar anisotropy. In the RD, the YS was similar for all alloys, however a slight increase of the yield stress with a decreasing Gd:Zn ratio could be observed (see Table 2). Whereas in the TD, it dropped by ~20–~45 MPa for the alloy with the highest relative Zn content. The strain hardening capability and maximum tensile elongation were higher in the TD. The largest maximum tensile strain was also found in Mg-Gd-Zn 1:2 strained in the TD, followed by 1:1 and 2:1, which showed a smaller degree of anisotropy.

To understand the different deformation behavior of the present ternary alloys, EBSD-assisted slip trace analysis was employed. Slip traces formed by the intersection of the slip plane and the sample surface usually appear as straight lines, and can be thus linked to a slip system by acquiring the grain orientation from the EBSD data [40].

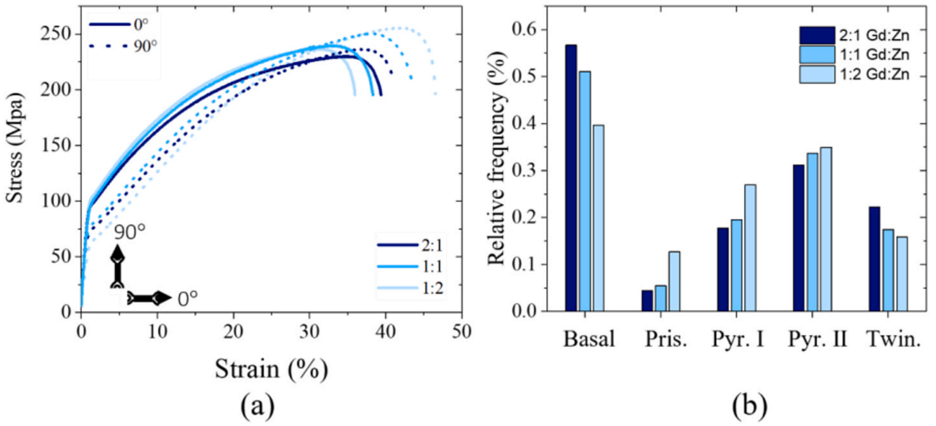

Fig. 8. (a) Stress-strain response in uniaxial tension along RD and TD of Mg-Gd-Zn with different Gd:Zn ratios (1:1, 1:1, 1:2) annealed for 60 min at 400 °C. (b) Distribution of the active slip systems from slip trace analysis (Fig. 9) of Mg-Gd-Zn alloys strained in RD.

Table 2
Tensile properties of ternary Mg-Gd-Zn alloys.

Alloy/Gd: Zn	Yield Stress R_p (MPa)				Fracture elongation A (%)			
	RD	s.d.	TD	s.d.	RD	s.d.	TD	s.d.
2:1	92.04	0.71	71,00	0.61	37.16	4.80	35.00	0.40
1:1	95.14	1.56	73.83	0.70	34.38	0.87	37.28	0.93
1:2	98.51	1.22	60.92	0.93	29.91	1.15	38.85	0.78

Uniform elongation A_g (%)				Ultimate Tensile strength (MPa)			
RD	s.d.	TD	s.d.	RD	s.d.	TD	s.d.
23.50	0.35	30.45	0.64	162.12	1.07	217.66	2.71
25.15	0.83	31.15	0.57	218.08	1.50	228.66	3.05
21.50	0.35	34.55	0.57	226.14	1.70	248.04	1.22

Deformation twinning was analyzed separately by visual evaluation of each grain. Fig. 9 presents examples of such analysis, where basal, pyramidal I and pyramidal II slip activities were identified by correlating the traces in the SE images with the theoretical slip traces based on the grain orientation. Regions that showed twinning were highlighted by a white circle. For the present analysis, at least 80 grains per alloy were evaluated and the relative frequency of grains that showed slip traces corresponding to a specific slip system was calculated.

Fig. 8 (b) shows the relative frequency of the observed active slip systems, i.e. basal, prismatic, pyramidal I, $c + a$ pyramidal II and twinning for uniaxial tensile deformation in RD up to a strain of 5%. Although basal slip was found to be dominant in all alloys, the addition of Zn seems to lead to an enhanced activation of non-basal slip, while the frequency of grains that deform by basal slip decreased. The frequency of prismatic as well as pyramidal I and $c + a$ pyramidal II slip was found to gradually increase with an increasing rel. Zn solute concentration.

4. Discussion

4.1. Synergistic effects on solute segregation and cluster formation

Combined addition of Gd and Zn solutes was found to lead to the development of a preferentially TD-oriented texture evident upon annealing at 400 °C for 60 min (Fig. 3, bottom row). This type of texture has been already reported in several studies investigating the microstructure development of rolled and annealed Mg–Zn-RE alloys, including similar Mg-Gd-Zn alloy systems [10,16,17,19,41]. What is however still an open question is how the synergistic effect of the co-alloying elements, Zn and Gd, can trigger such a strong texture modification, where we not only see a difference between the binary and the ternary alloy but also between different Gd/Zn concentration ratios. The texture obviously shifts from a spread of the basal pole towards the RD in the binary alloy to a pole spread towards the TD with almost no remaining RD and ND components in the case of the ternary composition. Moreover, with increasing relative Zn fraction, i.e. in the Mg-Gd-Zn 1:2 alloy, the TD spread becomes more prominent.

Fig. 10 (a) shows the relative area fraction of grains with close orientations to ND, TD and RD, respectively, as a function of relative Zn fraction. The corresponding grains were assigned according to the angle between their c-axis and the respective direction. ND grains were defined by a tilt angle between the c-axis and ND smaller than 40°, TD

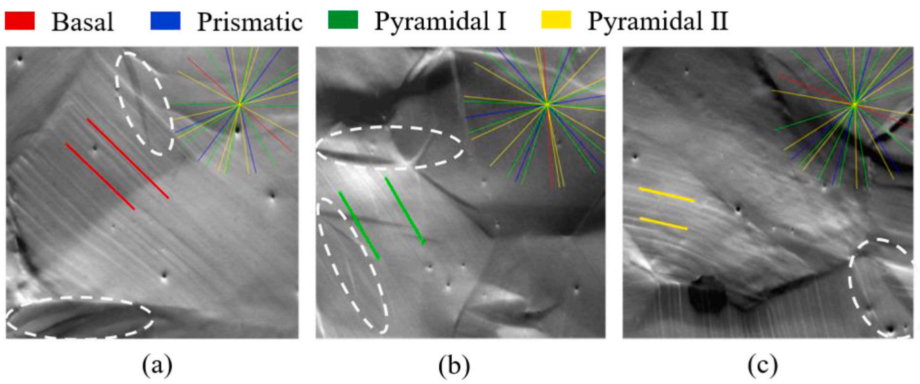

Fig. 9. Examples of the EBSD-assisted slip trace analysis carried out in the study. Slip lines of basal (red) (a), pyramidal I (green) (b) and pyramidal II (yellow) (c) slip. Twinned regions are highlighted by a white circle. Additionally, all theoretical slip lines according to the grain orientation from EBSD are shown in the upper right corner of each image. (For interpretation of the references to color in this figure legend, the reader is referred to the Web version of this article.)

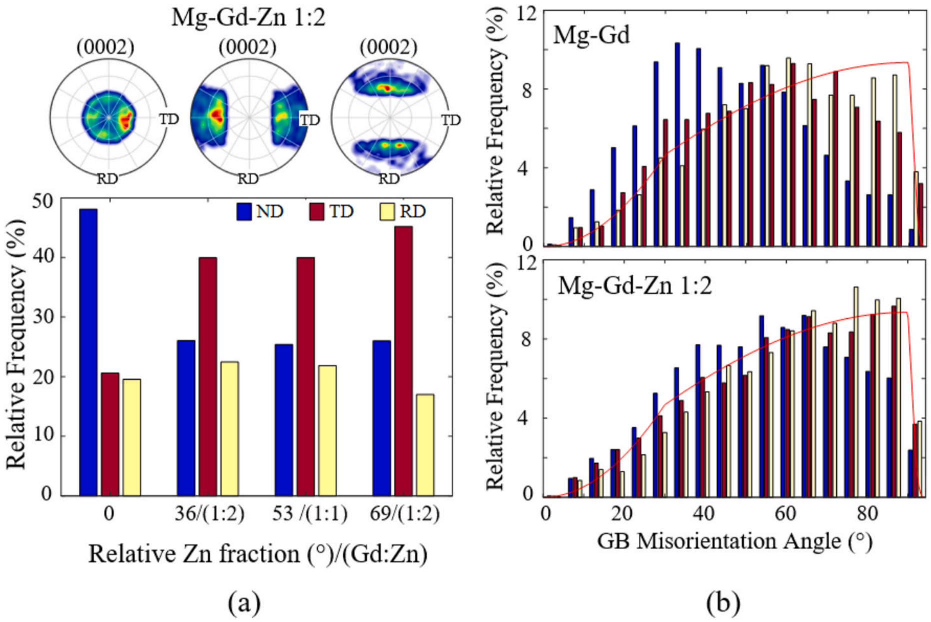

Fig. 10. (a) (0002)-pole figures of ND, TD and RD-oriented grains, assorted by the tilt angle between their c-axis and the three sample coordinate axes (upper part). Relative area fraction of ND, TD and RD grains as a function of the rel. Zn solute fraction (lower part). (b) Grain boundary misorientation distribution corresponding to ND, TD and RD grains of binary Mg–Gd (upper) and ternary Mg-Gd-Zn 1:2 (lower) (same color key used in (a)). The red line shows the Mackenzie distribution. (For interpretation of the references to color in this figure legend, the reader is referred to the Web version of this article.)

and RD grains by an angle larger than 60° from ND towards TD or RD. Additionally, the chosen TD- and RD-oriented grains were allowed a scatter of ±20° in the RD or TD. An example of corresponding (0002)-pole figures illustrating the orientation of the ND, TD and RD grains of Mg-Gd-Zn 1:2 is shown in the upper part of Fig. 10 (a). The fraction of grains with an ND orientation decreases significantly at the expense of off-basal texture components with the addition of Zn as it can be seen from Fig. 10 (a). Even a small relative Zn fraction, e.g., 36%, leads to the decrease of ND oriented grains and an increase of both RD and TD oriented grains. However, a further increase of the rel. Zn fraction in Mg-Gd-Zn 1:2 shows that ND grains will decrease preferentially at the expense of TD rather than RD oriented grains. It is therefore evident that not only the amount of Zn, but also the Gd:Zn ratio plays a key role in the grain growth characteristics, and therefore the texture evolution. The grain size distribution after 60 min of annealing at 400C shows no significant difference in grain size, accordingly solute drag might cause anisotropic grain growth of TD texture components at early growth stages, while it did not significantly affect the grain size after long term annealing.

The grain boundary misorientation distribution in Fig. 6 showed that the addition of Zn (regardless of Gd:Zn ratio) shifts the frequency peaks towards larger angles (i.e. the distribution becomes similar to the Mackenzie distribution). By examining the grain boundary misorientation distribution for the different orientation groups, ND, TD and RD, for binary Mg–Gd (Fig. 10 b upper part) it becomes clear that the peak around 30–40° originates from the ND grains, while the TD and RD grains tend to exhibit higher misorientation angles with their neighbors and show a distribution close to the theoretical case of a random polycrystal. The small misorientation angles found for ND grains hint at similar orientation between neighboring grains. Accordingly, ND grains might exist in a preferentially oriented ND neighborhood, as their misorientation is further away from the theoretical distribution. Those small misorientation angles are commonly observed in Mg alloys and attributed to the low energy and high mobility of 30° 0001 grain boundaries, which are suggested to cause a sharp basal texture upon recrystallization [42].

By comparison, the distribution of grain boundary misorientation angles in the ternary Mg-Gd-Zn 1:2 alloy (Fig. 10) shows an evident decrease in area fraction for ND-oriented grains, which were not showing frequency peaks at 30° but rather at 55°. Another significant trend in the distribution after the addition of Zn is the increase of area fraction for TD-oriented grains at large misorientation angles between 60° and 90°. Accordingly non-basal grains (whether TD or RD-oriented) are the main reason for the occurrence of large misorientation angles after the addition of Zn. This is likely a result of a modified grain boundary migration behavior due to solute pinning and solute segregation.

A large size misfit between solute atoms and matrix atoms, e.g. in the case of Mg and Gd, introduces elastic strain that is accommodated by solute segregation to grain boundaries. Zn atoms create a negative size misfit and tend to co-segregate alongside the Gd solutes to minimize the overall elastic energy. Next to the size misfit solutes-solute and solute-matrix binding energies will play a key role during segregation. To quantify the extent of segregation, the segregation energy ΔG_{seg} was calculated after the Langmuir-McLean adsorption model using Eq. (4.1), where X_M represents the solute concentration within the matrix and X_{GB} at the grain boundary [43].

$$\frac{X_{GB}}{1-X_{GB}} = \left(\frac{X_M}{1-X_M}\right)*exp\left(-\frac{\Delta G_{seg}}{RT}\right) \qquad \text{(Eq. 4.1)}$$

Fig. 11 (b) shows the segregation energy as a function of the rel. Zn fraction. X_M was calculated from the matrix concentration within the cylindric region of interest (see Fig. 7) expanding from ± 10 nm to ± 5 nm away from the grain boundary. The negative segregation energy of the ternary alloys increased for Gd as well as for Zn, in the case of Gd from 11 kJ/mol to 16 kJ/mol. The binary alloy shows approximately the same segregation energy as the ternary alloy with a rel. Zn fraction of 36%, but a further increase of the rel. Zn fraction led to a significant magnification of segregation. The Gd solutes of the alloy with the highest rel. Zn fraction (69%) show a very high negative segregation energy despite the fact that the Gd concentration within the alloy was smaller compared to the other two ternary alloys. This suggests that co-segregation might be crucial for the development of the microstructure since it governs the segregation behavior. The amount of Gd solutes that participate in segregation, and therefore has an impact on microstructure evolution does not mainly depend on the Gd concentration within the alloy, but its combination with other alloying elements, namely Zn. This is in accordance with the texture observations made before, as the preference for TD oriented components emerged mainly in the alloy with the highest relative Zn fraction compared to the others.

As co-segregation appears to be more or less effective depending on the Gd to Zn ratio of the alloy composition, it becomes important to

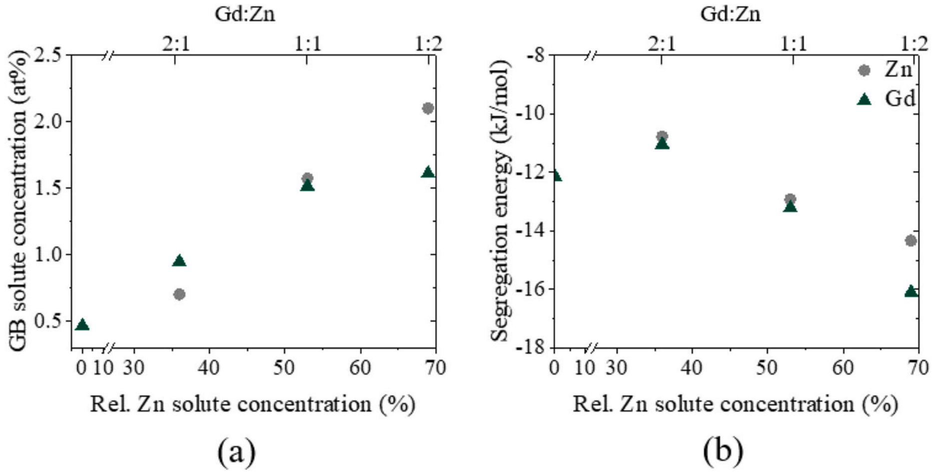

Fig. 11. Measured peak concentration of Gd (green) and Zn (grey) at the grain boundary (a), as well as the corresponding GB segregation energy as a function of the relative Zn fraction (b). (For interpretation of the references to color in this figure legend, the reader is referred to the Web version of this article.)

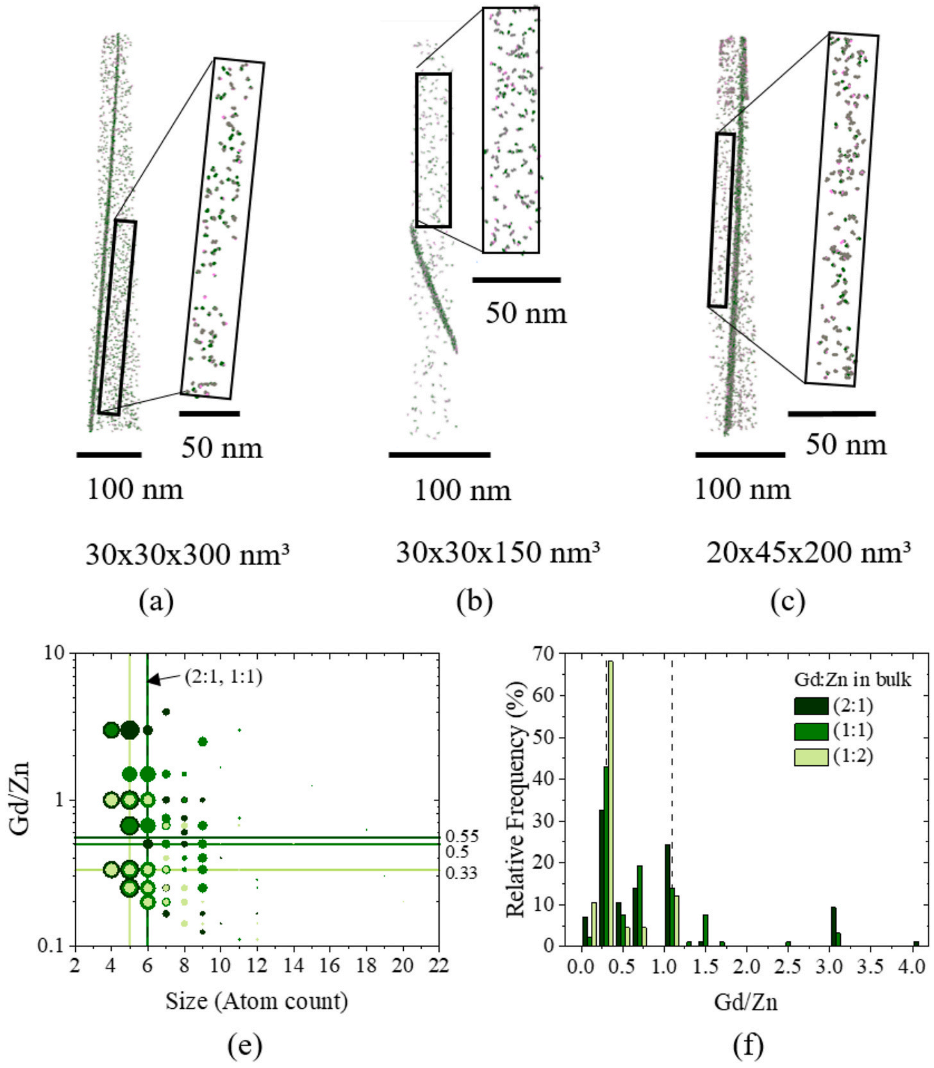

Fig. 12. Quantitative solute cluster analysis calculated from APT data showing elemental distribution of separated cluster atoms for Mg-Gd-Zn with Gd:Zn ratios of 2:1 (a), 1:1 (b) and 1:2 (c), respectively. Gd:Zn ratio within the Gd–Zn clusters as a function of the cluster size in atoms, the symbol size was scaled according to the frequency of the cluster size (e), as well as the cluster distribution as a function of the Gd:Zn ratio (f).

examine the characteristics of the existing solute clusters within the matrix. Solute clusters were analyzed using the IVAS, Cameca software and only first order clusters with a minimum size of 4 solute atoms and a distance to the nearest-neighbor within the cluster (d_{max}) of 1.25 nm were considered. Fig. 12 (a-c) show the detected solute clusters in all measured ternary Mg-Gd-Zn APT tips, 2:1, 1:1 and 1:2, respectively. Additionally, a cuboid region of interest was selected and highlighted. Its precise dimensions are given below each tip. Gd–Zn, Zn–Zn and a limited number of Gd–Gd clusters were detected. Zn–Zn clusters were most frequent in Mg-Gd-Zn 1:2, they represented 43% of all clusters. On the other hand, they were the least frequent in Mg-Gd-Zn 2:1 (18% of all clusters). Gd–Gd clusters were only found in Mg-Gd-Zn 2:1. This could be attributed to the low Zn concentration in this alloy. The formation of Gd–Zn clusters is probably preferential compared to Gd–Gd clusters, therefore there formation will be limited if there is a sufficient amount of Zn. Table 3 summarizes the results of the solute cluster analysis including the number frequency, density, size and cluster composition (for Gd–Zn clusters). To quantify the composition and size of clusters with respect to their Gd:Zn ratio, the Gd–Zn clusters within the marked region were further analyzed. Fig. 12 (d) shows the Gd:Zn ratio of the clusters as a function of the cluster size. The horizontal lines indicate the median Gd:Zn ratio and the vertical ones the median cluster size. Fig. 12 (e) shows the distribution of the Gd:Zn ratio of the clusters. The present solute clusters of all three alloys have a similar size and composition. The median Gd:Zn ratios vary between 0.33 and 0.55 and are significantly smaller than 1 in all alloys. Although Mg-Gd-Zn 2:1 has the largest Gd:Zn ratio (0.55) within the clusters compared to the other alloys, it is still far from the Gd:Zn ratio of 2 of the original alloy compositions.

The cluster distributions show a frequency peak around a Gd:Zn ratio of 0.33 for all alloys, hence the formed clusters come close to the nominal ratio of 0.5 in the Mg-Gd-Zn 1:2 alloy. Nearly 70% of all Gd–Zn clusters in Mg-Gd-Zn 1:2 exhibited a ratio of 0.33, while it was only 34% in Mg-Gd-Zn 2:1. The latter exhibited a second Gd:Zn ratio peak of 24% around 1:1. This ratio was found by Nie et al. for metastable phases during precipitation in an Mg-Gd-Zn-Zr alloy of similar Gd/Zn composition [44]. Assuming that co-segregation to grain boundaries occurs via the segregation of solute clusters of a Gd:Zn ratio of 0.33, an alloy with a high rel. Zn fraction is crucial for the formation of clusters and following GB segregation. The low Gd:Zn ratio in Mg-Gd-Zn 1:2 might enable the formation of more 1:3 Gd–Zn clusters, that will segregate to the boundaries. This would explain the higher negative segregation energy in Mg-Gd-Zn 1:2 (see Fig. 11).

Mg-Gd-Zn 1:2 exhibited the largest tendency for TD tilted texture components, as well as the highest segregation at grain boundaries. Both were found to be consistent the high relative Zn fraction of the alloy, demonstrating the influence of synergistic effects of combined solute additions on grain boundary segregation and texture evolution. To explain the favorable growth of TD-tilted texture components and the prevalence of specific grain boundary misorientation angles, anisotropic grain boundary properties and in particular boundary mobility need to be considered. In this regard, Barrett et al. suggested that solute segregation can lead to homogenization of the grain boundary energy, as well as a reduction of the mobility of highly mobile grain boundaries, suppressing the growth advantage of basal texture components, and thereby enabling nucleation and growth of new orientations [9,29]. This hypothesis helps explain the disappearance of the rolling basal texture components during annealing, but the reason for the observed pronounced TD preference remains unclear. A recent theoretical study showed by means of ab-initio simulations that the binding energy between RE solutes and Mg atoms varies significantly with the grain boundary character [32]. This will most probably result in an anisotropic mobility, affecting the stability of specific grain boundaries, thus influencing texture evolution during recrystallization and grain growth. Additionally, not only the effect of solutes on specific boundaries but segregation itself might be anisotropic, as it was recently proven to be in Mg-Mn-Nd [45] and other material systems (e. g. (Pt-Au) [46]). Accordingly, selective growth of TD tilted texture components is assumed to be caused by a growth advantage of specific grain boundaries due to alterations in their energy and mobility, induced by complex solute-boundary interactions. While a clear understanding of the nature of these anisotropic effects needs further experimental and theoretical investigation, it was shown in the present study that they are likely to be manipulated by the synergistic properties resulting from different co-alloying concentration. This became clear as small alterations of the Gd:Zn contents were able to trigger RE-texture effects of different extents. Considering the importance of the atomic solute ratio compared to the absolute solute concentrations shown in this work, the influence of clustering on solute-boundary interaction appears to be crucial for the development of a synergistic alloy design concept tailored towards desirable TD-type textures for enhanced formability.

4.2. Connection between active deformation modes and the yield stress anisotropy

An anisotropy of the yield point between strain in RD and TD was observed from tensile tests. This anisotropy is most likely linked to the alloy composition as it deviates significantly amongst the analyzed alloys. Although all analyzed alloys contain different total solute concentrations, as well as different relative concentrations of Gd and Zn (see. Table 1), the yield strength in the rolling direction of all alloys is similar (see Fig. 8). This indicates that the effect of solid solution strengthening on the yield point is limited. Changes of the deformation behavior may be attributed to the previously observed texture modifications and/or solute effect on the activation of the available deformation modes. Accordingly, the reason for the observed anisotropy needs further investigation.

EBSD-assisted slip trace analysis revealed a connection between non basal slip and Zn additions (cf. Fig. 9). Table 4 shows the basal to non-basal slip ratio for all detected non-basal slip systems and twinning. It is worth noticing that this ratio increases with an increasing rel. Zn

Table 4

Non-basal to basal ratio of activated slip systems obtained from slip trace analysis in Mg-Gd-Zn 2:1, 1:1 and 1:2 strained in RD and TD (only 1:2). The deformation modes considered are prismatic, pyramidal I and II as well as twinning (manual detection).

Alloy/Gd:Zn	Basal: Pris.	Basal: Pyr. I	Basal: Pyr. II	Basal: Twin.
2:1 RD	1:0.08	1:0.31	1:0.55	1:0.39
1:1 RD	1:0.11	1:0.38	1:0.66	1:0.34
1:2 RD	1:0.32	1:0.68	1:0.88	1:0.40
1:2 TD	1:0.22	1:0.78	1:0.78	**1:1**

Table 3

Characteristics of present Gd–Zn, Gd–Gd and Zn–Zn solute clusters in the investigated Mg-Gd-Zn alloys obtained from solute cluster analysis by means of APT data mining using the commercial software IVAS, Cameca.

Alloy/Gd:Zn	Gd–Zn				Gd–Gd			Zn–Zn		
	Size [atom]	Count	Ratio	Density [nm^{-1}]	Size [atom]	Count	Density [nm^{-1}]	Size [atom]	Count	Density [nm^{-1}]
2:1	5	89	0.55	$33\cdot10^{-5}$	5	6	$2.2\cdot10^{-5}$	5	19	$7.0\cdot10^{-5}$
1:1	6	93	0.5	$69\cdot10^{-5}$	–	–	–	5	34	$25\cdot10^{-5}$
1:2	6	66	0.33	$36\cdot10^{-5}$	–	–	–	5	51	$28\cdot10^{-5}$

fraction for all non-basal slip systems, especially for pyramidal II $c+a$ slip. This coincides with the previously observed increase of the yield stress with an increasing rel. Zn fraction (see Table 2). A larger activation of non-basal slip may elevate the flow stress as non-basal slip systems are known to have a significantly larger CRSS compared to basal slip [47]. By contrast, the ratio twinning: basal slip remained approximately constant. A markedly low occurrence of prismatic slip was observed, which can be rationalized by the relatively low applied strain of 5%, as higher strains are needed to enable cross slip of basal dislocations to the prismatic plane [48,49]. The large fraction of basal slip traces in all the samples is correlated to the low critical resolved shear stress (CRSS) of basal slip, commonly known to be significantly lower than the CRSS for non-basal slip modes [50]. In the present case, a higher activation of non-basal slip modes, including $c+a$ slip is to be expected due to the presence of Gd, as it is commonly the case for Mg-RE alloys vs. conventional RE-free alloys, e.g. AZ31 [22]. It is further reasonable to assume that this effect is further enhanced in the current alloys due to the co-presence of Zn [24,51]. In fact, this is clearly demonstrated by the enhanced activation of non-basal slip in alloys containing a higher relative Zn fraction, which could be caused by a change in the relative CRSS ratio between basal and non-basal slip. Prior studies suggested basal slip strengthening by RE solute pinning of basal a dislocations as a possible mechanism [52,53]. Next to the inhibition of dislocations solute segregation to grain boundaries could hinder the emission of dislocations from the boundary [54]. Accordingly, synergistic effects of RE and Zn can be reasonably presumed to have a stronger interaction with mobile dislocations, and hence play a more prominent role in slip system activity as compared to individual RE additions.

Despite the observed deviations in slip system activation during straining in RD (Table 4), the yield point in that direction (unlike in TD) was only marginally affected by the Gd:Zn ratio of the alloy composition (Fig. 8a). To further characterize the anisotropic mechanical response in TD, slip trace analysis at 5% strain in TD was performed for the Mg-Gd-Zn 1:2 alloy exhibiting the largest anisotropy. Fig. 13 (b) presents the corresponding relative frequencies of the different active slip systems and Table 4 contains the basal to non-basal slip ratio for Mg-Gd-Zn 1:2 for both strain paths in RD and TD. The results show that slip activation of all considered slip systems in TD was similar to that in RD. However, the activation of twinning was found to increase significantly in the TD sample compared to the RD. The basal to twinning ratio changed from 1:0.4 under strain in RD to 1:1 under strain in TD. Hence, in the case of strain in TD twinning was as frequent as basal slip. To investigate this further, tensile specimens of all three ternary alloys were strained up to 25% in RD and TD and analyzed via EBSD. Fig. 14 shows the resulting IPF maps and the corresponding pole figures of Mg-Gd-Zn 2:1 (a), 1:1 (b) and 1:2 (c), as well as the corresponding distribution of the grain boundary misorientation angles, the positions of twin boundaries of $\{10\bar{1}1\}$ compression (56°) and $\{10\bar{1}2\}$ tension (86°), as well as $\{10\bar{1}1\}-\{10\bar{1}2\}$ double twinning (37.5°) are marked in red, blue, and magenta, respectively.

As evident by the RD tension texture (Fig. 14 a, b, c upper part), the TD-spread of the basal poles of the initial textures was further enhanced during tension in RD, while a transition from a TD dominated texture to a slightly off-basal ring texture was formed under straining in TD.

Fig. 15 shows the starting (a) and final texture after 20% straining in TD (c), as well as a theoretical (0002) pole figures (b) illustrating whether the observed texture transition is a result of tension (TT) or compression twinning (CT). The orientations resulting from a rotation of the basal plane around $\bar{2}110$ by 56° (CT) and 86° (TT), respectively are in accordance with the experimental texture components arising upon 25% tensile strain in TD. Hence, the high activity of twinning, particularly compression twinning, leads to a shift of peak density in TD to a favorable one in RD during tension in TD. Additionally, the samples strained in TD of all alloys show an overall higher fraction of grain boundaries with misorientations corresponding to twinning (Fig. 14). This is also in accordance with the enhanced twinning after 5% of strain in TD compared to RD observed via slip trace analysis. In the literature, some studies (e.g. by Luo et al. [55]) reported similar findings of enhanced deformation twinning activity in a ternary Mg–2Zn-0.8Gd alloy and pointed out its importance with respect to formability.

All three alloys show a similar increase of compression twinning under uniaxial strain in TD compared to strain in RD. The fraction of grain boundaries with a misorientation angle of 56° increased from approximately 7 to 15%. Tensile twinning increased in both Mg-Gd-Zn 2:1 and 1:2, while it remained constant in Mg-Gd-Zn 1:1. However, the change in tensile twinning in Mg-Gd-Zn 1:2 was significantly larger compared to Mg-Gd-Zn 2:1. The magnitude of anisotropy in tensile twin activation in Mg-Gd-Zn 1:2, compared to the alloys with a lower relative Zn fraction, matches the yield stress anisotropy shown in Fig. 13 (a). Both, the observed anisotropy in twinning activation, as well as the resulting anisotropy in mechanical properties are in accordance with previous studies indicating enhanced twinning under strain in TD [56,57]. The enhanced activation of twinning could originate from the priory observed texture modifications, however all alloys show similar texture components while the amount of tensile twins under strain in TD was enhanced significantly. This suggests a combination of texture and immediate solute effects as the underlying mechanisms for a change of the deformation modes. Accordingly, the synergistic influence of Zn and

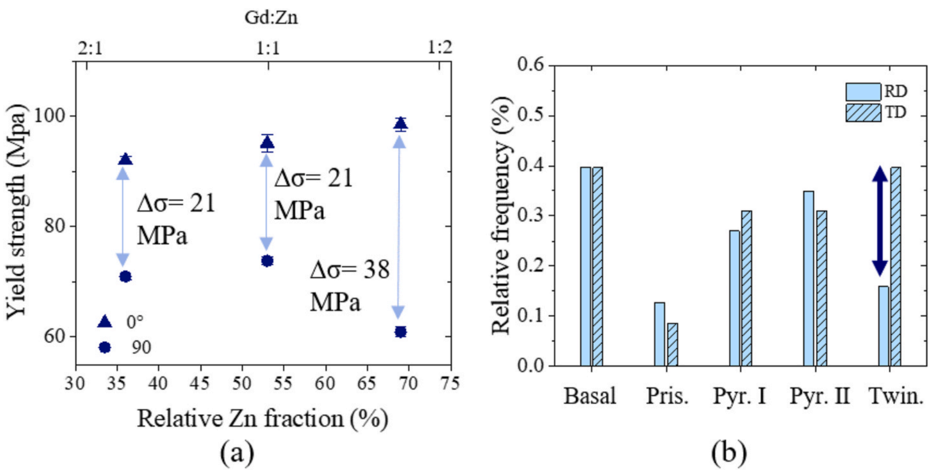

Fig. 13. (a) Yield strength obtained from the corresponding stress-strain curves in RD, TD and 45° sheet directions as a function of the relative Zn fraction. (b) Distribution of the active slip systems extracted from slip trace analysis of Mg-Gd-Zn with the ratio 1:2 during uniaxial-tension up to 5% strain in RD and TD. All samples were initially subjected to annealing at 400 °C for 60 min.

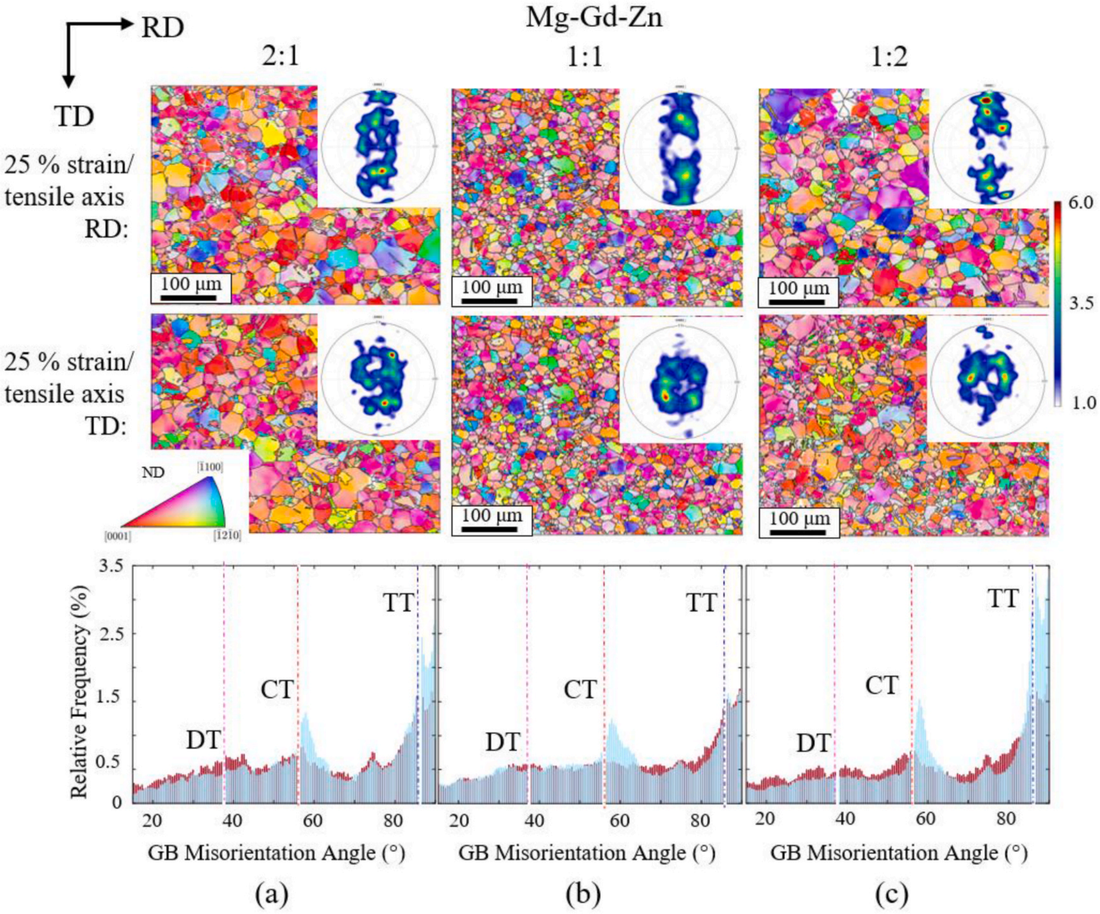

Fig. 14. IPF-ND maps from EBSD data of Mg-Gd-Zn 2:1 (a), 1:1 (b) and 1:2 (c) collected after 25% tensile strain in RD (upper row) and TD (lower row) with the corresponding distributions of the grain boundary misorientation angles. The misorientation angles of compression (56°), tension (86°) and double twin boundaries (37.5°) are indicated in red, blue, and magenta respectively. (For interpretation of the references to color in this figure legend, the reader is referred to the Web version of this article.)

Gd on twin activation was found to be a central mechanism in terms of planar yield stress anisotropy. Segregation of Gd and Zn to twin boundaries was previously found to influence the mobility and enhance the stability of twin boundaries [27]. This suggests a high impact of the aforementioned synergistic solute effects on twinning. The activation of non-basal deformation modes, as well as twinning, did not solely depend on the amount and type of solute species but was shown to be strongly linked to their relative ratio in the material.

5. Conclusions

1. Addition of different relative Zn content to a dilute Mg–Gd sheet alloy led to a significant texture modification favoring off-basal texture components. With increasing relative Zn fraction there was a clear preference for a unique basal pole spread towards the transverse direction. This suggests a significant impact of synergistic solute effects on the microstructure evolution and the resulting texture.
2. A shift in the grain boundary misorientation angle distribution from 30° to 40° (in a Mg–Gd alloy) towards larger angles was observed in all the investigated Mg-Gd-Zn alloys leading to a distribution close to the Mackenzie distribution of a random polycrystal. Special analysis of the boundary distribution data based on individual assessment of ND, RD and TD-oriented grains revealed that a random distribution originates from the non-basal texture components.
3. Atom probe tomography of Mg–Gd and the three Mg-Gd-Zn alloys with a different relative Zn solute fraction showed that solute segregation is controlled by the ratio of Gd to Zn solute concentration in the matrix. The negative segregation energy, as well as the peak concentration at the grain boundary were found to increase with an increasing relative Zn solute fraction. The absolute amount of Gd concentration was of little importance in this case.
4. Identified solute clusters from the APT data revealed a frequent solute composition of Gd:Zn equal to 0.33 in all three ternary alloys despite different nominal Gd:Zn ratios of the original alloy composition. Accordingly, the formation of stable clusters capable of grain boundary co-segregation is likely to require a higher Zn concentration. This would explain the enhanced segregation in alloys with a large relative Zn solute fraction.
5. Uniaxial tensile tests of the ternary Mg-Gd-Zn alloys in both RD and TD directions revealed a planar anisotropy of the yield stress. The magnitude of this anisotropy was found to be correlated to the Gd:Zn solute ratio, particularly in straining along the TD.
6. EBSD-assisted slip trace analysis of 5% strained Mg-Gd-Zn samples in RD revealed enhanced activation of non-basal slip accompanied by a relative decrease of basal slip events. This was particularly the case for the Mg-Gd-Zn 1:2 alloy with the highest relative Zn fraction. A comparison of active slip systems under strain in RD and TD in this alloy revealed similar activation of all common slip systems in magnesium. The fraction of grains exhibiting twinning was however doubled for straining in TD, which was also confirmed by grain boundary distribution data from EBSD. This is likely the reason for the observed RD/TD anisotropy of the yield stress.

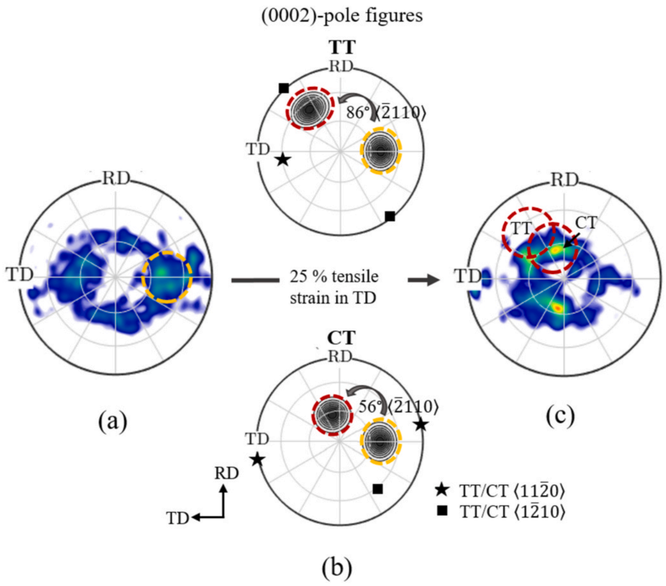

Fig. 15. (a) Starting texture of Mg-Gd-Zn 1:2 annealed at 400 °C for 60 min prior to tensile tests and (c) final texture after 25% of strain in TD. Characteristic TD-texture component of the initial state (yellow circle) and possible orientations after tension (TT, top) and compression twinning (CT, bottom) with a basal plane rotation around $11\bar{2}0$ (marked by stars), $1\bar{2}10$ (marked by rectangle) and $\bar{2}110$, which lead to orientations that can be found in the texture after tensile deformation (red circle) (b). (For interpretation of the references to color in this figure legend, the reader is referred to the Web version of this article.)

Data availability statement

The raw/processed data required to reproduce these findings cannot be shared at this time as the data also forms part of an ongoing study.

CRediT authorship contribution statement

F. Mouhib: Conceptualization, Methodology, Validation, Formal analysis, Investigation, Data curation, Writing – original draft, preparation, Visualization. **R. Pei:** Methodology, Software. **B. Erol:** Validation, Formal analysis, Investigation. **F. Sheng:** Validation, Formal analysis, Investigation. **S. Korte-Kerzel:** Resources, Supervision, Project administration, All authors have read and agreed to the published version of the manuscript. **T. Al-Samman:** Conceptualization, Resources, Data curation, Writing – review & editing, Supervision, Project administration, Funding acquisition.

Declaration of competing interest

The authors declare that they have no known competing financial interests or personal relationships that could have appeared to influence the work reported in this paper.

Acknowledgement

The authors are grateful for financial support from the Deutsche Forschungsgemeinschaft (DFG), Grant No. AL1343/7-1.

References

[1] A. Ahmadian, et al., Aluminum depletion induced by co-segregation of carbon and boron in a bcc-iron grain boundary, Nat. Commun. 12 (1) (2021) 6008.
[2] M. Takenaka, et al., Unique effect of carbon addition on development of deformation texture through changes in slip activation and twin deformation in heavily cold-rolled Fe-3% Si alloys, Acta Mater. 157 (2018) 196–208.
[3] A. Maldar, et al., Activation of <c> dislocations in Mg with solute Y, J. Magnesium Alloys (2021), https://doi.org/10.1016/j.jma.2021.11.004. https://www.sciencedirect.com/science/article/pii/S2213956721002711.
[4] C. Wang, et al., Grain boundary design of solid electrolyte actualizing stable All-solid-state sodium batteries, Small 17 (40) (2021), e2103819.
[5] J.J. Bhattacharyya, S.R. Agnew, G. Muralidharan, Texture enhancement during grain growth of magnesium alloy AZ31B, Acta Mater. 86 (2015) 80–94.
[6] L.A.I. Kestens, H. Pirgazi, Texture formation in metal alloys with cubic crystal structures, Mater. Sci. Technol. 32 (13) (2016) 1303–1315.
[7] R. Gehrmann, M.M. Frommert, G. Gottstein, Texture effects on plastic deformation of magnesium, Mater. Sci. Eng., A 395 (1–2) (2005) 338–349.
[8] Technology of magnesium and magnesium alloys, in: Magnesium Technology: Metallurgy, Design Data, Applications, Springer Berlin Heidelberg, Berlin, Heidelberg, 2006, 219-430.
[9] C.D. Barrett, et al., Effect of grain boundaries on texture formation during dynamic recrystallization of magnesium alloys, Acta Mater. 128 (2017) 270–283.
[10] T. Al-Samman, X. Li, Sheet texture modification in magnesium-based alloys by selective rare earth alloying, Mater. Sci. Eng., A 528 (10–11) (2011) 3809–3822.
[11] J.P. Hadorn, et al., Role of solute in the texture modification during hot deformation of Mg-rare earth alloys, Metall. Mater. Trans. 43 (4) (2011) 1347–1362.
[12] K. Hantzsche, et al., Effect of rare earth additions on microstructure and texture development of magnesium alloy sheets, Scripta Mater. 63 (7) (2010) 725–730.
[13] J.D. Robson, Effect of rare-earth additions on the texture of wrought magnesium alloys: the role of grain boundary segregation, Metall. Mater. Trans. 45 (8) (2013) 3205–3212.
[14] M.R. Barnett, M.D. Nave, C.J. Bettles, Deformation microstructures and textures of some cold rolled Mg alloys, Mater. Sci. Eng., A 386 (1–2) (2004) 205–211.
[15] E.A. Ball, P.B. Prangnell, Tensile-Compressive Yield Asymmetries in High Strength Wrought Magnesium Alloys, Scripta Metallurgica et Materialia, 1994, p. 31.
[16] L. Mackenzie, M. Pekguleryuz, The recrystallization and texture of magnesium–zinc–cerium alloys, Scripta Mater. 59 (6) (2008) 665–668.
[17] F.-Z. Mouhib, et al., Texture selection mechanisms during recrystallization and grain growth of a magnesium-erbium-zinc alloy, Metals 11 (1) (2021).
[18] I. Basu, T. Al Samman, G. Gottstein, Recrystallization and grain growth related texture and microstructure evolution in two rolled magnesium rare-earth alloys, Mater. Sci. Forum 765 (2013) 527–531.
[19] I. Basu, T. Al-Samman, Triggering rare earth texture modification in magnesium alloys by addition of zinc and zirconium, Acta Mater. 67 (2014) 116–133.
[20] L. Wang, et al., Study of slip activity in a Mg-Y alloy by in situ high energy X-ray diffraction microscopy and elastic viscoplastic self-consistent modeling, Acta Mater. 155 (2018) 138–152.
[21] J. Wu, et al., Study of basal < a > and pyramidal < c + a > slips in Mg-Y alloys using micro-pillar compression, Phil. Mag. (2020) 1–22.
[22] S. Sandlöbes, et al., On the role of non-basal deformation mechanisms for the ductility of Mg and Mg–Y alloys, Acta Mater. 59 (2) (2011) 429–439.
[23] S. Sandlöbes, et al., Ductility improvement of Mg alloys by solid solution: ab initio modeling, synthesis and mechanical properties, Acta Mater. 70 (2014) 92–104.
[24] C. Ha, et al., Texture development and dislocation activities in Mg-Nd and Mg-Ca alloy sheets, Mater. Char. (2021) 175.
[25] F. Wang, et al., In situ observation of collective grain-scale mechanics in Mg and Mg–rare earth alloys, Acta Mater. 80 (2014) 77–93.
[26] I. Basu, T. Al-Samman, Hierarchical twinning induced texture weakening in lean magnesium alloys, Front. Mater. 6 (2019).
[27] J.F. Nie, et al., Periodic segregation of solute atoms in fully coherent twin boundaries, Science 340 (6135) (2013) 957–960.
[28] E. Hersent, K. Marthinsen, E. Nes, The effect of solute atoms on grain boundary migration: a solute pinning approach, Metall. Mater. Trans. 44 (7) (2013) 3364–3375.
[29] C.D. Barrett, A. Imandoust, H. El Kadiri, The effect of rare earth element segregation on grain boundary energy and mobility in magnesium and ensuing texture weakening, Scripta Mater. 146 (2018) 46–50.
[30] J.D. Robson, et al., Grain boundary segregation of rare-earth elements in magnesium alloys, Metall. Mater. Trans. 47 (1) (2015) 522–530.
[31] N. Stanford, et al., Solute segregation and texture modification in an extruded magnesium alloy containing gadolinium, Scripta Mater. 65 (10) (2011) 919–921.
[32] R. Mahjoub, N. Stanford, The electronic origins of the "rare earth" texture effect in magnesium alloys, Sci. Rep. 11 (1) (2021) 14159.
[33] I. Basu, et al., The role of atomic scale segregation in designing highly ductile magnesium alloys, Acta Mater. 116 (2016) 77–94.
[34] X.H. Shao, et al., Atomic-scale segregations at the deformation-induced symmetrical boundary in an Mg-Zn-Y alloy, Acta Mater. 118 (2016) 177–186.
[35] C. He, et al., Unusual solute segregation phenomenon in coherent twin boundaries, Nat. Commun. 12 (1) (2021) 722.
[36] R. Hielscher, H. Schaeben, A novel pole figure inversion method: specification of theMTEXalgorithm, J. Appl. Crystallogr. 41 (6) (2008) 1024–1037.
[37] J. Humphreys, G.S. Rohrer, A. Rollett, Recrystallization of Two-phase Alloys, 2017, pp. 321–359.
[38] I. Basu, T. Al-Samman, Twin recrystallization mechanisms in magnesium-rare earth alloys, Acta Mater. 96 (2015) 111–132.
[39] Yuling Xu, et al., Solid solution strengthening in Mg–Gd alloys, Magnesium Technol. 2016 (2016).
[40] J.S.K. Gibson, et al., Finding and characterising active slip systems: a short review and tutorial with automation tools, Materials 14 (2) (2021).

[41] H. Yan, et al., Effects of trace Gd concentration on texture and mechanical properties of hot-rolled Mg–2Zn–xGd sheets, J. Magnesium Alloys 1 (1) (2013) 23–30.

[42] X. Liu, J. Wang, Low-energy, mobile grain boundaries in magnesium, Sci. Rep. 6 (2016) 21393.

[43] D. McLean, A. Maradudin, Grain boundaries in metals, Phys. Today 11 (7) (1958) 35–36.

[44] J.F. Nie, et al., Solute segregation and precipitation in a creep-resistant Mg–Gd–Zn alloy, Acta Mater. 56 (20) (2008) 6061–6076.

[45] R. Pei, et al., Atomistic Origin of the Anisotropic Grain Boundary Segregation in a Mg-Mn-Nd Alloy, Archived on arXiv, 2022.

[46] C.M. Barr, et al., The role of grain boundary character in solute segregation and thermal stability of nanocrystalline Pt-Au, Nanoscale 13 (6) (2021) 3552–3563.

[47] M.R. Barnett, A taylor model based description of the proof stress of magnesium AZ31 during hot working, Metall. Mater. Trans. 34 (2003).

[48] S. Sandlöbes, et al., Basal and non-basal dislocation slip in Mg–Y, Mater. Sci. Eng., A 576 (2013) 61–68.

[49] Y. Chino, M. Kado, M. Mabuchi, Enhancement of tensile ductility and stretch formability of magnesium by addition of 0.2wt%(0.035at%)Ce, Mater. Sci. Eng., A 494 (1–2) (2008) 343–349.

[50] M.R. Barnett, A taylor model based description of the proof stress of magnesium AZ31 during hot work, Metall. Mater. Trans. 34 (2003).

[51] C. Ha, et al., Influence of Nd or Ca addition on the dislocation activity and texture changes of Mg–Zn alloy sheets under uniaxial tensile loading, Mater. Sci. Eng., A (2019) 761.

[52] J.P. Hadorn, et al., Effects of solute and second-phase particles on the texture of Nd-containing Mg alloys, Metall. Mater. Trans. 43 (4) (2012) 1363–1375.

[53] A. Tehranchi, B. Yin, W.A. Curtin, Solute strengthening of basal slip in Mg alloys, Acta Mater. 151 (2018) 56–66.

[54] Y. Ma, et al., Phase boundary segregation-induced strengthening and discontinuous yielding in ultrafine-grained duplex medium-Mn steels, Acta Mater. 200 (2020) 389–403.

[55] J. Luo, et al., Cold rollability improvement by twinning and twin–slip synergy in an Mg–Zn–Gd alloy with rare earth texture, J. Alloys Compd. (2021) 883.

[56] P. Dobroň, et al., A study of mechanical anisotropy of Mg–Zn–Rare earth alloy sheet, J. Alloys Compd. 588 (2014) 628–632.

[57] S.A. Habib, et al., Anisotropy, tension-compression asymmetry and texture evolution of a rare-earth-containing magnesium alloy sheet, ZEK100, at different strain rates and temperatures: experiments and modeling, Int. J. Plast. 95 (2017) 163–190.

7.3 On the role of selective nucleation and growth to recrystallization texture development in a Mg-Gd-Zn alloy

F. Z. Mouhib[1], RB. Gao[1]2 and T. Al-Samman[1].
[1]Institute of Physical Metallurgy and Materials Physics, RWTH Aachen University, Germany
[2]Steel Institute (IEHK), RWTH Aachen University, 52056 Aachen, Germany

Journal of Materials Science 59 (2023), p. 1044-1055, issn: 1573-4803.

The candidate carried out the conceptualisation, participated in the experimental work, guided and performed data analysis and did writing and editing of the manuscript.

Online availability: 10.1007/s10853-023-09243-3

J Mater Sci (2024) 59:1044–1055

Metals & corrosion

On the role of selective nucleation and growth to recrystallization texture development in a Mg–Gd–Zn alloy

F. Mouhib[1,*], B. Gao[1], and T. Al-Samman[1]

[1] *Institute of Physical Metallurgy and Materials Physics, RWTH Aachen University, 52056 Aachen, Germany*

Received: 15 September 2023
Accepted: 3 December 2023

ABSTRACT

One of the main material properties altered by rare earth additions in magnesium alloys is texture, which can be specifically adjusted to enhance ductility and formability. The current study aims at illuminating the texture selection process in a Mg–0.073at%Gd–0.165at%Zn alloy by investigating recrystallization nucleation and early nucleus growth during static recrystallization. An as-cast sample of the investigated alloy was deformed in uniaxial compression at 200 °C till 40% strain and was then cut into two halves for subsequent microstructure characterization via ex situ and quasi in situ EBSD investigations. In order to gain insights into the evolution of texture during recrystallization, the contributions from dynamic and static recrystallization were initially separated and the origin of the non-basal orientation of recrystallization nuclei was traced back to several potential nucleation sites within the deformed matrix. Considering the significant role of double-twin band recrystallization in determining the recrystallization texture, this type of recrystallization nucleation was further investigated via quasi-in situ EBSD on a deformed sample, annealed at 400 °C for different annealing times. With progressive annealing, a noticeable trend was observed, in which the basal nuclei gradually diminished and eventually vanished from the annealed microstructure. In contrast, the off-basal nuclei exhibited continuous growth, ultimately becoming the dominant contributors to the recrystallization texture. The study therefore emphasizes the importance of particular nucleation sites that generate favorably oriented off-basal nuclei, which over the course of recrystallization outcompete the neighboring basal-oriented nuclei in terms of growth and thereby dominate the recrystallization texture.

Handling Editor: Sophie Primig.

Address correspondence to E-mail: mouhib@imm.rwth-aachen.de

Springer

https://doi.org/10.1007/s10853-023-09243-3

Introduction

Texture is one of the main properties governing formability in magnesium alloys. Accordingly, the study of texture formation might be the key to the design of highly formable magnesium alloys [1]. In common magnesium alloys, the hexagonal crystal structure and therefore limited activation of non-basal slip lead to a strong basal texture rendering the material incapable of accommodating stresses out of the basal plane, i.e., along the c-axis [2, 3]. In that respect, it was found that magnesium-rare earth alloys are especially suitable to produce soft and weak textures through fine tuning of the alloy chemistry and processing parameters [4]. Binary Mg–RE alloys readily show major texture improvements characterized by weaker intensities and off-basal components in the rolling direction. New developments of ternary Mg–RE–Zn systems showed that respective alloys develop even more favorable textures with a characteristic spread of the basal poles in the transverse direction. Moreover, these alloys show a finer recrystallized grain size and a higher strength making them great candidates for sheet forming operations [5–13].

Despite extensive research efforts in that field, particular details of how new texture components nucleate during deformation or early recrystallization and come to dominate during growth remain elusive [6, 10, 14, 15]. From segregation studies, RE solute is known to segregate to grain boundaries and hence affect their migration behavior during recrystallization and grain growth [16–18]. This is thought to lead to the development of RE-texture components through competitive growth between basal and non-basal nuclei. The role of nucleation remains in comparison harder to elucidate due to the small scales considered. Nonetheless, we can reasonably assume that favorable nucleation conditions for RE orientations do exist since they were seen to dominate the final recrystallization texture. Common nucleation sites reported for magnesium alloys are deformation twins, grain boundaries and triple junctions, shear or deformation bands and second phase particles [19]. The contribution of these sites to the nuclei orientation is of crucial importance for the survival of certain orientations during further texture development in the course of nuclei growth. Particularly, nucleation at $\left\{10\bar{1}1\right\}-\left\{10\bar{1}2\right\}$ double twins and shear bands was found to generate characteristic RE texture components during static recrystallization of cold rolled Mg–RE alloys [20, 21].

Recent quasi-in situ electron backscatter diffraction (EBSD) studies have provided useful insights into the origin of RE texture formation by means of tracking the evolution of microstructure during recrystallization. Guan et al. analyzed the impact of double twins [21] and shear bands on the recrystallization texture formation [20] and reported that the resultant recrystallized grains made the main contribution to the final texture development. Interestingly, the authors have also reported that concurrent events, such as precipitation, can intervene with the competitive growth of basal and RE-oriented grains, thereby decreasing the substance of the desired RE components in the final texture [20]. Jiang et al. provided evidence of growth selection of RE orientations in an extruded and subsequently annealed Mg–Zn–Gd alloy depicting no significant amount of twins or shear localization [22]. Encouraged by these reports, the current study examines the influence of different nucleation sites and early nucleus growth on the texture selection during recrystallization in a Mg–Gd–Zn alloy.

Experimental

For this study, a ternary Mg–0.073at%Gd–0.165at%Zn alloy was used. Its chemical composition was measured by optical emission spectrometry (ICP/OES). An Ar/Co_2 gas atmosphere was applied when melting the alloy, which was cast into a pre-heated copper mold and homogenized at 460 °C for 960 min. Compression tests of cylindrical samples with a diameter of 5 mm and a height of 10 mm were conducted using a ZWICK screw-driven, mechanical testing machine at temperatures between room temperature (RT) and 400 °C and at a constant strain rate of $2 \times 10^{-3}\ s^{-1}$. The imposed deformation strains ranged between 0.1 and 0.8. Subsequently, the samples were cooled by Water quenching. The deformation conditions are summarized in Table 1.

Subsequent to compression, the samples were cut in half along the compression direction (cf. Fig. 1) and subjected to metallographic preparation using mechanical grinding and polishing with an ethanol-based diamond suspension up to 0.25 µm. For panoramic optical microscopy, the samples were electro-polished in an 5:3 ethanol/H_3PO_4 solution and subsequently etched in an acetic picral solution. Multiple overlapping micrographs were taken per sample

Table 1 The investigated deformation conditions in the current work (marked by x). The sample selected for the quasi-in situ EBSD was deformed at 200 °C for 40%

Def. (%)\T (°C)	RT	200	400
10	x	–	–
20	x	x	–
40	–	Quasi-in situ EBSD	X
60	–	–	X
80	–	–	x

using a Leica/Leitz DMR light microscope equipped with an Axiocam 305 camera and subsequently stitched with Image Composite Editor (Microsoft). For EBSD investigations, the respective sample was additionally electro-polished for 120 s using a Lectro-Pol 5 operating at 20 V and − 20 °C in a Struers AC2 solution.

EBSD measurements were conducted using a focused ion beam Helios 600i equipped with a HKL-Nordlys II EBSD detector operating at 20 kV and 2.7 nA. The resulting raw data were analyzed using the texture analysis toolbox MTEX [23]. Quasi-in situ EBSD experiments were done by interrupted heat treatments at 370 °C up to 95 min in a tube furnace under protective Ar atmosphere to minimize oxidation. Between the annealing steps, the sample was shortly polished using Struers OP-U suspension. Micro-indents were used as markers for relocating the same sampled area, using the x-,y-distance between the intend and the initial EBSD area. No data cleaning procedure was used on the EBSD data.

Results

Figure 1a shows the stress–strain curves after compression at different temperatures (see Table 1). Samples compressed at 400 °C are characterized by a steady plastic flow at low stresses of ~ 25 MPa. On the contrary, samples compressed at RT exhibited rapid work hardening and early fracture. Both of these conditions were deemed unsuitable for further annealing experiments demanding the right amount of stored deformation energy in order to track early nucleus growth in the mapped sample. This was obtained in the sample compressed at 200 °C up to 40% strain. Despite the somewhat elevated temperature, the sample at that deformation condition still cracked due to retarded dynamic recrystallization and lack of multiple slip systems. The work softening after the peak in the respective flow curve is associated with the macroscopic cracking of the sample, evident in Fig. 2.

In accordance with Fig. 1b, the chosen sample (200 °C/40%) was cut in two halves along the compression direction (CD) that were characterized further by panoramic optical microscopy, EBSD and XRD, as shown in Fig. 2. The investigated microstructure in Fig. 2a revealed numerous twins that were yet unrecrystallized. This changed in the other half of the sample (half 2), which was annealed at 400 °C for 60 min to initiate static recrystallization. To determine

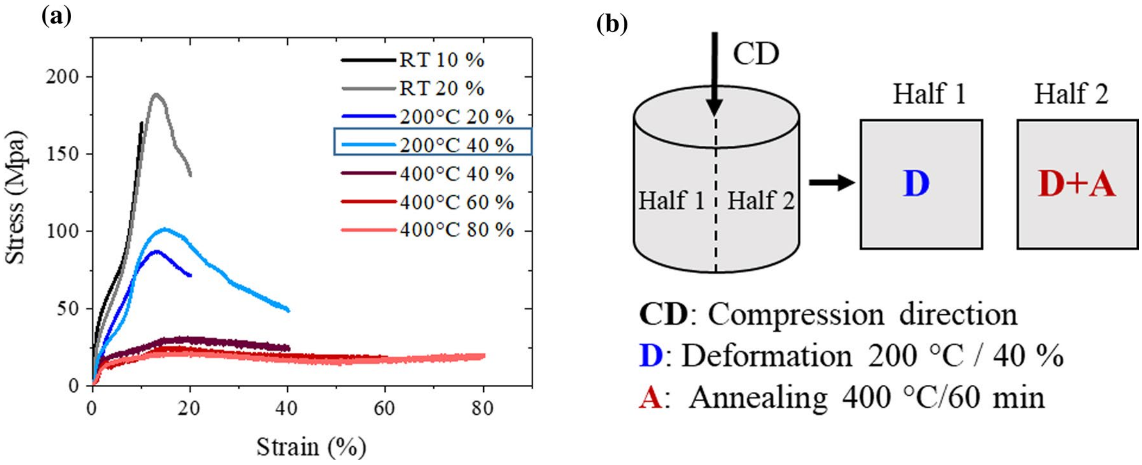

Figure 1 **a** Stress–strain response during compression tests at RT, 200 °C and 400 °C for deformation degrees ranging from 10 to 80%. **b** Schematic image of the cylindrical compression sample and the mirroring sample halves with their processing details.

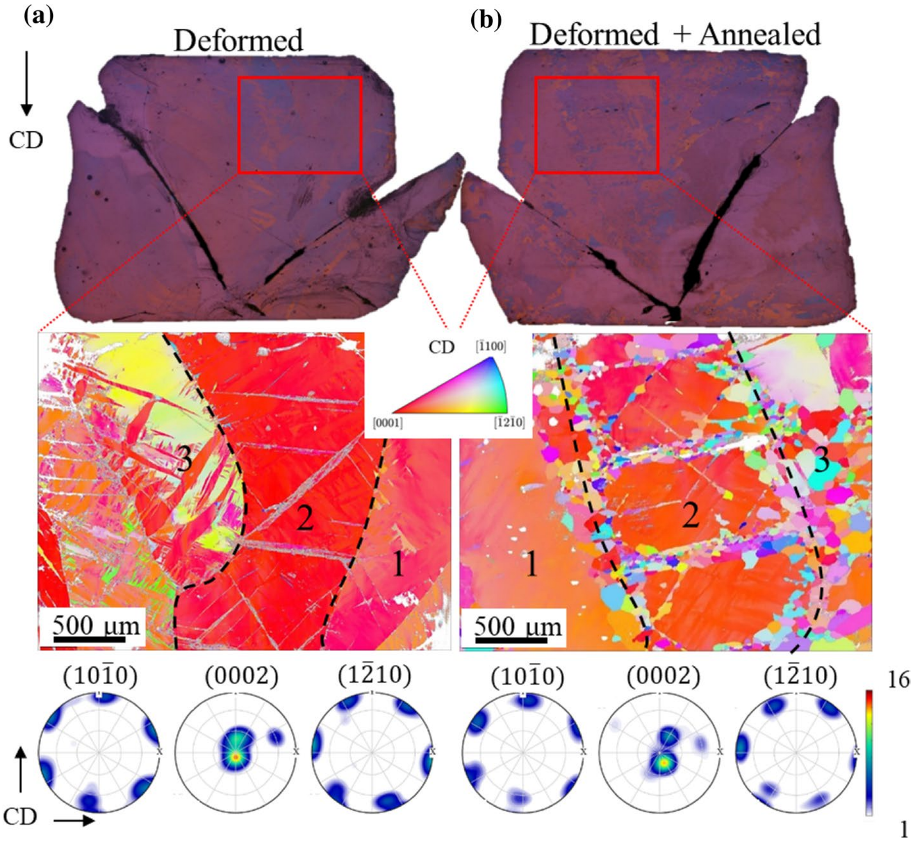

Figure 2 Panoramic optical micrographs of the entire compression sample, obtained in the mid-plane parallel to the compression direction CD: **a** deformed at 200 °C to 40%, **b** subsequently annealed at 400 °C for 60 min. EBSD data show CD-IPF maps of the sampled areas (in the deformed and recrystallized state) and corresponding textures. The original dataset was rotated by 90° about the x-axis in MTEX, aligning the CD perpendicular to the plane of the page. The texture intensity is represented in terms of multiples of a random distribution (m.r.d.).

the orientation of the recrystallized grains and evaluate their nucleation mechanism, EBSD was done on both the deformed and the subsequently annealed halves of the sample. The selected EBSD areas were mirroring each other, as outlined in Fig. 2, in order to allow a correlation between the deformed and recrystallized microstructures. In addition to inverse pole figure (IPF) maps with respect to CD, the corresponding (0002), (10$\bar{1}$0) and (10$\bar{1}$2) pole figures are also presented in Fig. 2. The provided IPF color key is applicable to all subsequent IPF maps. Hence, it is only presented once.

The left side of the CD-IPF of the deformed sample exhibited a high twin density (region 3), which subsequent to annealing underwent extensive recrystallization visible on the right side of the counterpart CD-IPF of Fig. 2b. Another feature in the deformed microstructure is a large grain with thin bands (region 2) that were liable to recrystallization nucleation and growth during annealing (Fig. 2b). As shown later in Fig. 4, those recrystallized bands are associated with double twins as they exhibited a characteristic misorientation relationship with the matrix. Further, recrystallization after annealing was seen at high angle grain boundaries separating the three big grains (regions) in the deformed microstructure. The right side of the deformed map (region 1), featuring one large matrix grain free from inner grain boundaries or obvious stress accumulations, remained free of recrystallization. The pole figures of the deformed and recrystallized microstructures do not show large qualitative differences in the overall texture since recrystallization was not advanced.

To further characterize the twinning activity seen in region 3 of the deformed state, Fig. 3 presents a CD-IPF map of a higher resolution (Fig. 3b), obtained from the outlined area of interest in the original map (Fig. 3a). The microstructure of the selected area reveals profuse twinning of several twin variants, as well as limited dynamic recrystallization in the grain boundary region (cf. Fig. 5). The misorientation angle distribution exhibits a distinct peak around 86° ± 4° revealing that the observed twins were mostly $\left\{10\bar{1}2\right\}$ tension twins (TT). Additional peaks around 56° ± 4° and 37.5° ± 4° might be related to some $\left\{10\bar{1}1\right\}$ compression (CT) and compression–tension double twins (DT) (Fig. 3c). The deformation texture was found to be a characteristic basal

Figure 3 **a** CD-IPF map after 40% of compression at 200 °C and corresponding grain boundary angle misorientation distribution (**b**), as well as texture from (0002), and $(1\bar{2}10)$ pole figures.

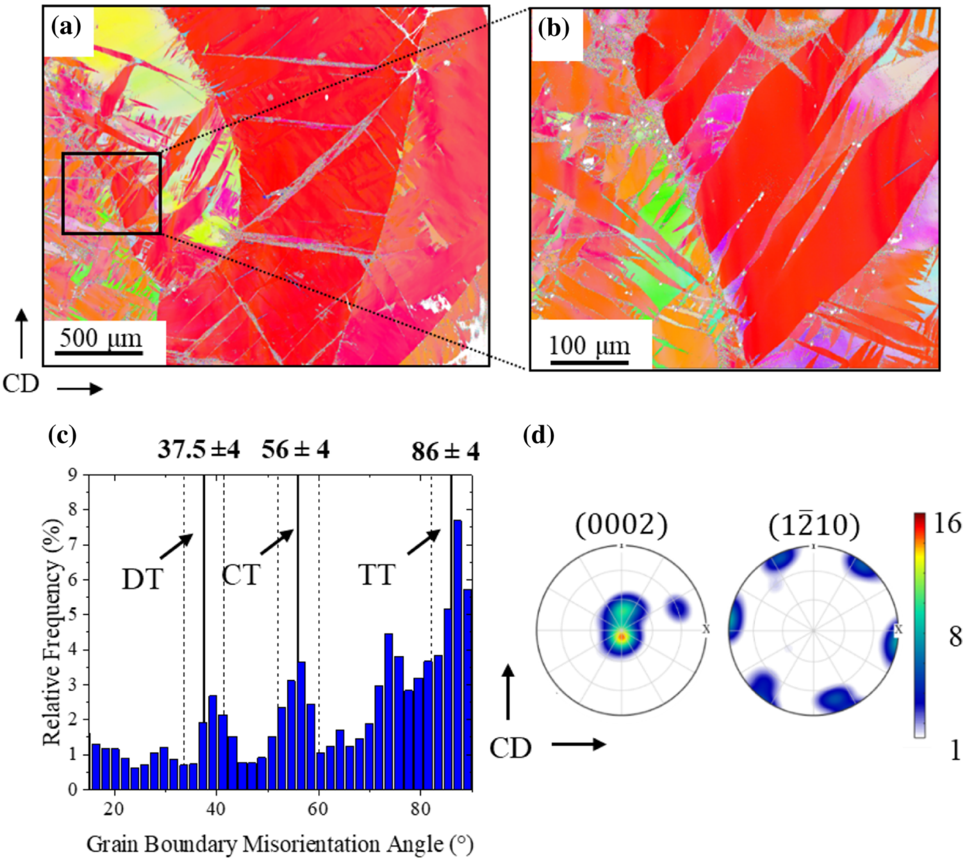

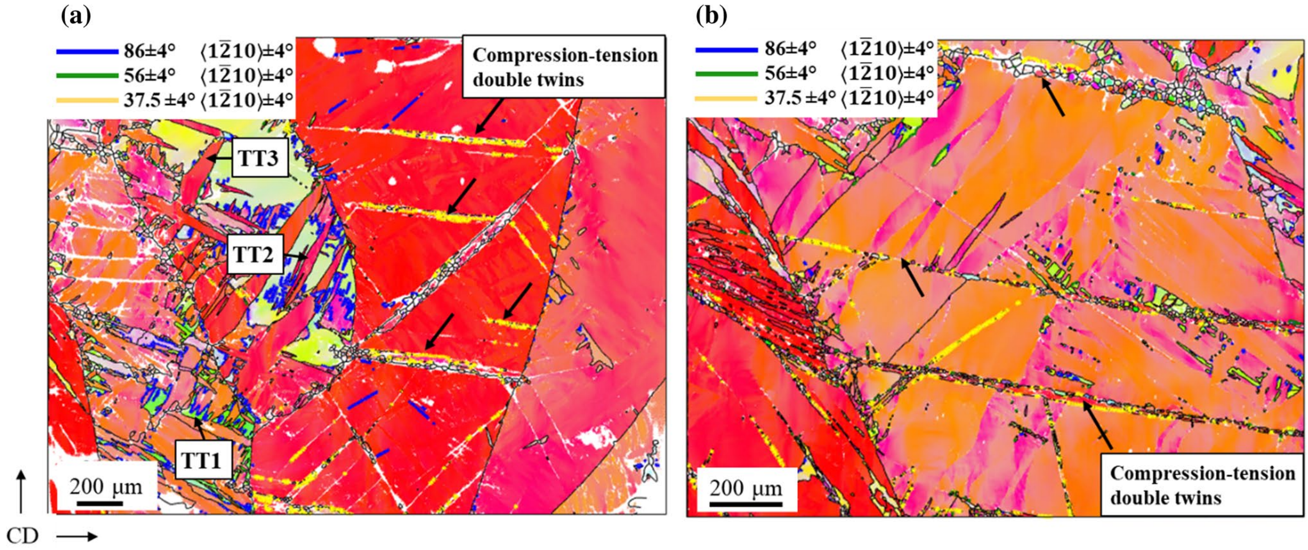

Figure 4 EBSD CD-IPF maps showcasing the $\{10\bar{1}1\}-\{10\bar{1}2\}$ double-twin bands in the deformed microstructure (**a**) and their role as a nucleation site for recrystallization in an annealed sample (370 °C/5 min) (**b**). TT1-3 in (**a**) refer to three different variants of $\{10\bar{1}2\}$ tension twins. Due to the coarse grain structure in the deformed and annealed samples, local orientation gradients within individual grains are clearly visible.

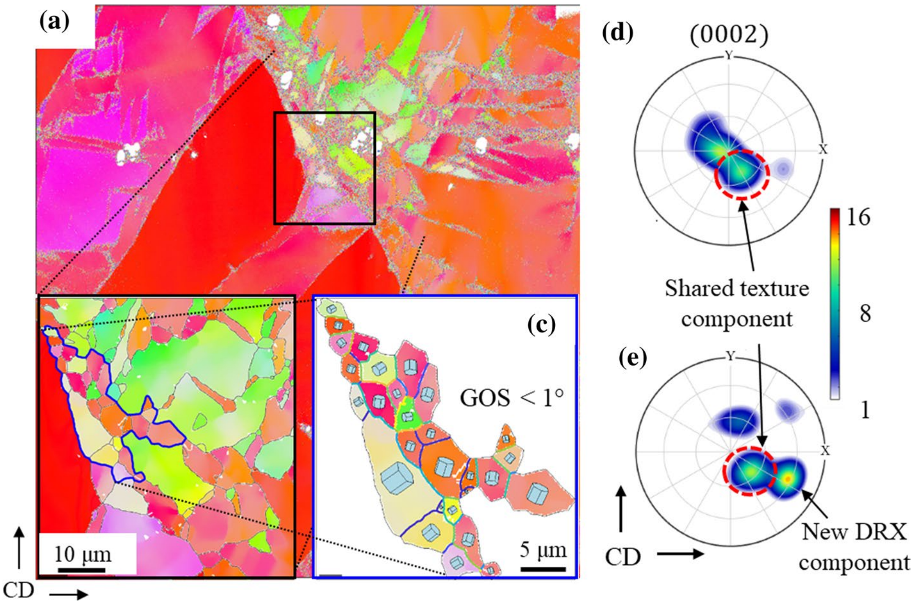

Figure 5 Selected area from the CD-IPF map of the deformed sample presented in Fig. 3b featuring a dynamically recrystallized region outlined in blue (**b**), which is characterized by means of grain orientation spread (GOS) < 1° (**c**) and corresponding (0002) pole figures for the whole map shown in **a** (**d**) and the dynamically recrystallized region depicted in **b** (**e**), respectively.

texture, with a slight tilt of basal poles (± 10°) about the compression direction (Fig. 3d).

Figure 4 shows two IPF map examples showcasing the thin bands observed in the deformed microstructure, which were seen to recrystallize during annealing. As evident from the misorientation analysis of twins and their parent matrix, the thin bands in the microstructure correspond to compression–tension double twins of the type $\left\{10\bar{1}1\right\}-\left\{10\bar{1}2\right\}$ that exhibits a characteristic misorientation of 37.5° $\langle 1\bar{2}10\rangle$ with the parent matrix. These twins are also evident in the IPF map in Fig. 4b, which shows a different region of the microstructure after a short annealing at 370 °C for 5 min. These parameters were chosen carefully to obtain evidence of the onset of recrystallization in these particular nucleation sites. The region shown in Fig. 4b is utilized later for the quasi-in situ annealing experiments presented in Fig. 8 to gain insights into the selective growth behavior exhibited by the off-basal oriented nuclei. The labeled twins TT1-3 correspond to tension twin variants examined later in Fig. 7 in relation to recrystallization nucleation in that region.

Discussion

To understand the development of texture during early stages of recrystallization, the contributions from dynamic and static recrystallization have to be separated and assigned to the different potential nucleation sites present in the microstructure (grain boundaries, tension twins, and double-twin bands). The deformed area from the compression test at 200 °C up to 40% strain showed limited dynamic recrystallization near the grain boundaries (GB). One example is shown in Fig. 5a, b featuring a selected area of few recrystallized grains, detected using a grain orientation spread criterion (GOS < 1) (Fig. 3c). The lack of sufficient number of DRX grains in the map does not allow for sound correlations to be made. However, it can be seen by the single orientations of these grains and their corresponding (0002) pole figure that some of them developed a new texture component located at 60° from the compression direction (Fig. 5e). It is also visible that the rest of the DRX grains share a similar texture component (30° from CD) with the deformed matrix (Fig. 5d, e).

Retardation of dynamic recrystallization at 200 °C is caused by the segregation of RE solute atoms to grain boundaries leading to solute drag [24]. This intended effect is beneficial for further static recrystallization because a sufficient amount of deformation will still be retained in the deformed microstructure. Indeed, as will be shown later, static recrystallization is crucial for the formation of soft, off-basal texture components. Figure 6 shows the distribution of the basal poles with respect to the CD for the uniquely deformed (red) and the subsequently annealed sample half (blue), along with their corresponding (0002) pole figures, as obtained from EBSD. After deformation, the distribution of basal poles shows a close alignment with the CD (sharp basal texture) but with annealing, the spread of basal poles about the CD shifts to higher angles, leading to a much weaker texture. Similar orientation distributions with large tilt angles from the principal loading axis have been previously observed in heat treated Mg–RE–Zn alloys [5, 25], but their formation from a deformation basal texture is still unclear.

To trace back the development of the non-basal recrystallization nuclei from the deformation basal texture, the recrystallized grains from the EBSD map in Fig. 2b were carefully analyzed in connection to their original matrix site. The analysis is shown in Fig. 7, which features the isolated subset of recrystallized grains (GOS < 1°) and individual (0002) pole figures of different portions of the recrystallization microstructure. The three sets of pole figures shown in Fig. 7(b) (i-iii) correspond to recrystallized grains at different nucleation sites in the deformed microstructure (cf. Fig. 2a): (i) Large-angle GB between matrix regions 1 and 2 (red rectangle), (ii) parallel recrystallized double-twin bands in region 2 (blue rectangle), and (iii) $\left\{10\bar{1}2\right\}$ twinned region (black rectangle). For establishing a connection with the deformation texture components, the average orientation of the parent matrix is provided in each pole figure. For (i), this information is given in terms of the average orientation of the two adjacent grains M1 and M2, for (ii) in terms of the average orientation of grain M2 and that of the double twins (DT), and for (iii) in terms of the orientation of three $\left\{10\bar{1}2\right\}$ twin variants (cf. Fig. 4) labeled TT1, TT2, and TT3. The superposition of all (0002) pole figure sets produces the final (0002) pole figure for the total recrystallized IPF map, shown in Fig. 7c. The texture components in that pole figure are outlined on the basis of their origin, whether stemming from nucleation (i) at the grain boundary, (ii) within the recrystallized double-twin bands, or (iii) within the heavily tensile twinned region. The latter is quite difficult to assess because of the large heterogeneity of that region in the deformed state. Hence, recrystallization in region (iii) is not only restricted to nucleation in the twin interior but also to other nucleation sites, including twin–twin interfaces, twin–GB intersections, and other grain boundary segments. This leads to multiple texture components in the corresponding (0002) pole figure that partially overlaps with components from the other regions (i) and (ii) (Fig. 7).

From the sharpest recrystallization texture component in Fig. 7b-i, the orientation of recrystallized grains at the GB lies close to the orientation of the deformed parent matrix M1 and M2. For the tensile twinned region 3 (cf. Fig. 2), the sharpest components in the pole figures (Fig. 7b-iii) do not overlap with each other nor with the displayed orientations of the three twin variants. They show basal poles with a 30° tilt from the CD and are believed to stem from a combination of several nucleation sites seen in region (iii). With respect to recrystallization within the parallel double-twin bands, corresponding recrystallization nuclei revealed clear off-basal components at 60° and 90° from the CD (Fig. 7b-ii). As evident, both pole figures in Fig. 7a-ii exhibit virtually the same recrystallization texture, which seems to be quite reproducible for this nucleation site. Also visible is that this off-basal texture differs markedly from the original deformation basal texture depicted in Fig. 6. This follows the trend of texture alteration observed in Mg–RE–Zn alloys after hot-rolling and recrystallization annealing [6, 26]. The individual analysis of orientation relationships shown in Fig. 7a, b for different nucleation sites helps clarify how the final, net texture shown in Fig. 7c emerges from the competition among growing nuclei of types (i-iii) during commencing recrystallization.

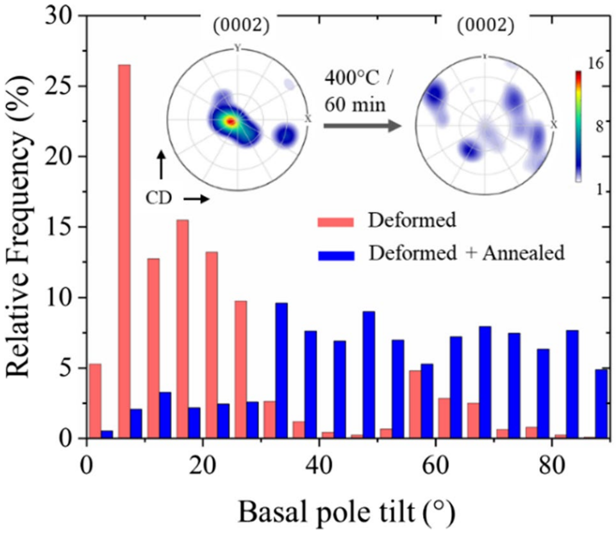

Figure 6 Angle distribution between the c-axis and the compression direction obtained from EBSD data of the deformed (200 °C/40%) and annealed sample. Low angles indicate close alignment of basal poles with the compression axis, i.e., a basal orientation. The insets in the figure show the corresponding (0002) pole figures of the deformed (outlined in red) and the recrystallized regions (blue) after 60 min of annealing at 400 °C.

Figure 7 **a** IPF subset map of the recrystallized fraction (GOS < 1) reproduced from the IPF map shown in Fig. 2b. The marked regions (i)–(iii) correspond to recrystallization nucleation at a grain boundary (i), within deformation bands (ii), and within a heavily-twinned region (iii). These regions are analyzed individually by means of their (0002) pole figures (**b**) (i)-(iii). The texture components in the total (0002) pole figure in (**c**) can be traced back to their nucleation mechanism by correlating the respective orientations between (**b**) and (**c**).

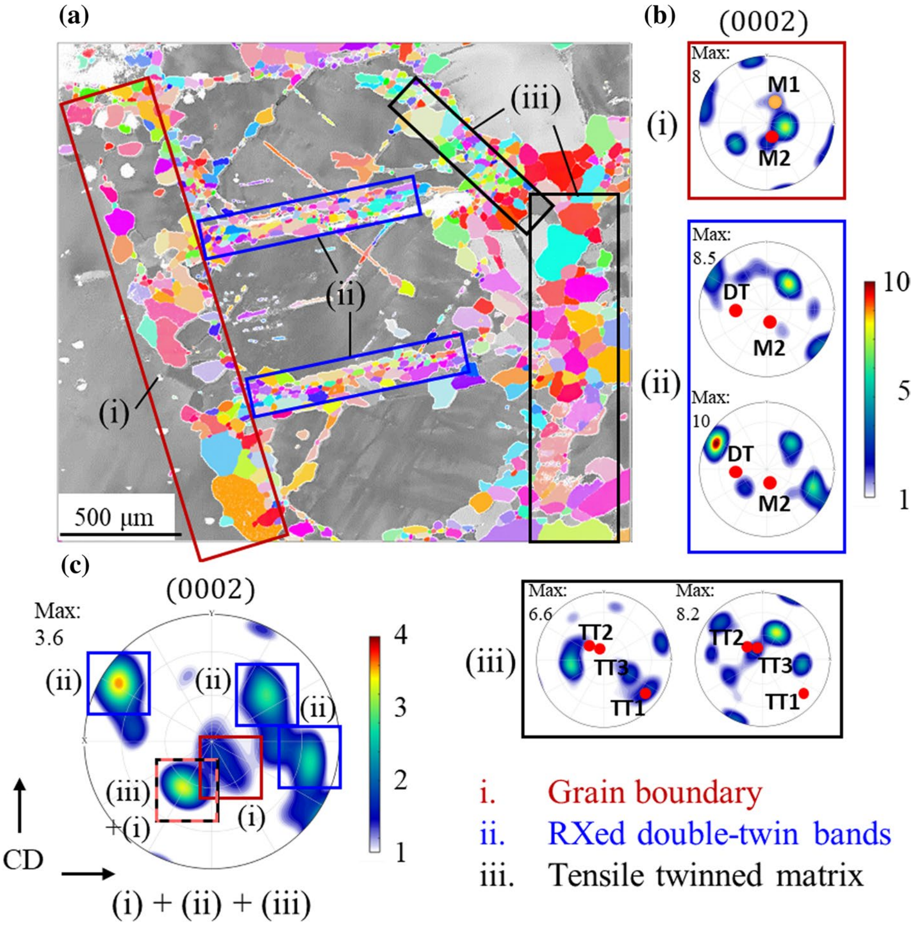

Given the important contribution of double-twin band recrystallization to the final recrystallization texture, this type of recrystallization nucleation was further investigated via quasi-in situ EBSD on a deformed sample, annealed at 400° for different annealing times between 600 and 5700 s (95 min). The results are shown in Fig. 8 in terms of IPF maps relative to CD and corresponding (0002) pole figures. It is noted that the observation of microstructure evolution at a free surface might be affected by the reaction of grain boundaries below the surface, leading to lower average grain boundary mobility during nucleus growth. While this might have an influence on the growth rate of recrystallizing grains, it is less likely that it biases the evolution of texture in comparison with bulk recrystallization.

The orientations of recrystallized grains (GOS < 1°) inside the deformation band for different annealing times are presented in Fig. 8g and h by means of discrete and contour pole figures, respectively. The grains used for the analysis were selected manually to eliminate artifacts. The relatively high texture intensity in the contour pole figures is mainly due to the small number of GOS < 1° grains investigated. The initial texture of the recrystallization nuclei after 5 min of annealing at 370 °C shows both, basal and off-basal orientations. With increasing annealing time, the off-basal orientation is further strengthened, while the basal orientation weakens and eventually disappear. It should be noted that the resulting main texture component after 85 min annealing time resembles the main texture components observed during ex situ recrystallization of the double-twin bands (see Fig. 7ii). The importance of this nucleation site for the formation of favorable recrystallization texture components is therefore its ability to provide off-basal oriented nuclei capable of eclipsing basal orientations during growth. This is shown in Fig. 9 on the basis of three selected off-basal nuclei G1, G2, and G3 that grow on the expense of basal-oriented neighboring grains.

Figure 9 presents three examples highlighting the favorable growth behavior of off-basal

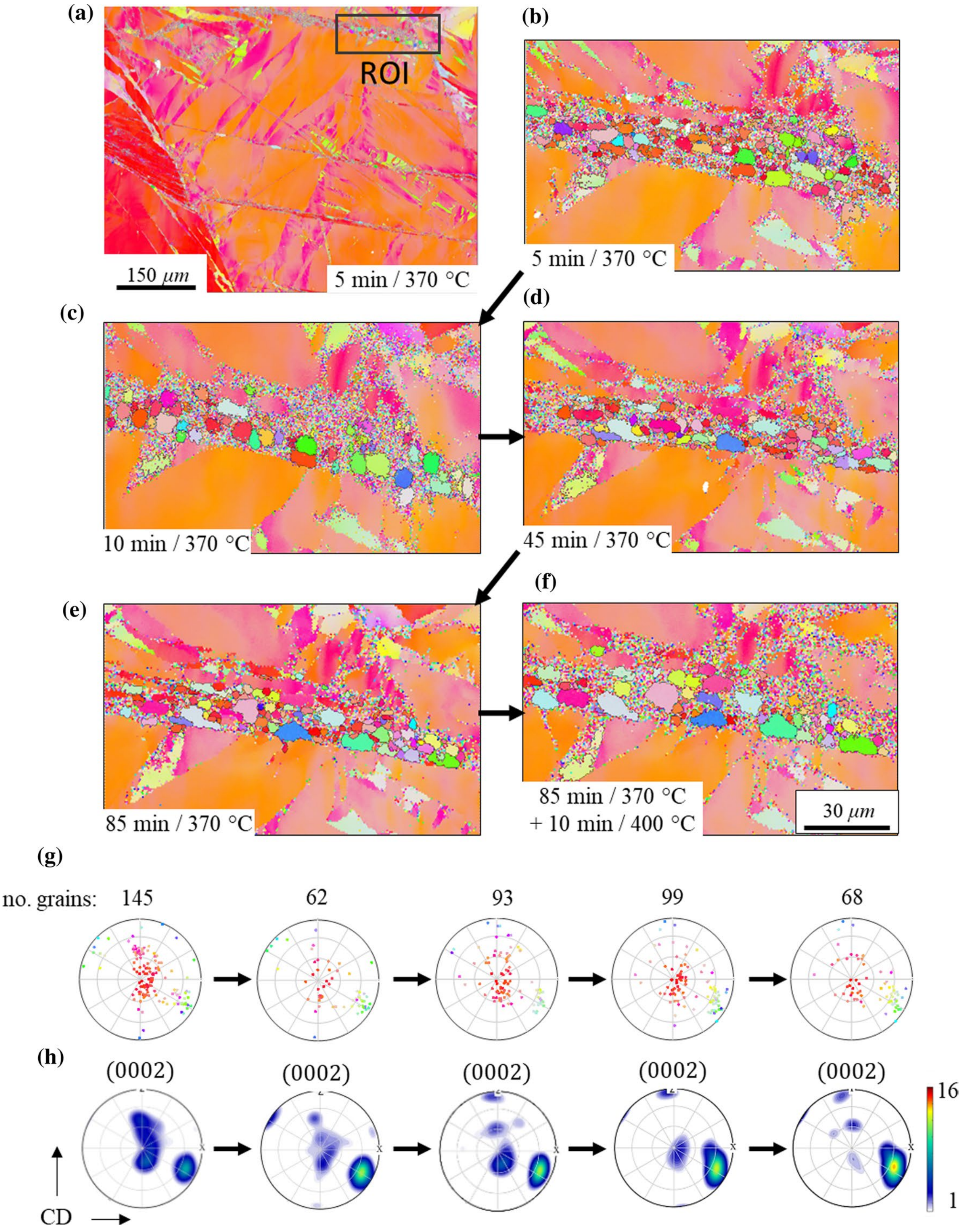

Figure 8 Quasi-in situ CD-IPF maps of a region of interest (ROI) used to track early nuclei growth in a deformation band as a function of annealing time (**a**–**f**). The corresponding texture evolution of the GOS < 1° grains inside the deformation band is shown in terms of (0002) discrete (**g**) and contour pole figures (**h**).

recrystallization nuclei. These examples were reproduced from the quasi-in situ EBSD data shown in Fig. 8. The presented cases show the off-basal nuclei G1, G2, and G3 that initially coexist with basal-oriented neighbors of a comparable size. With progressive annealing, it can be observed how the basal nuclei

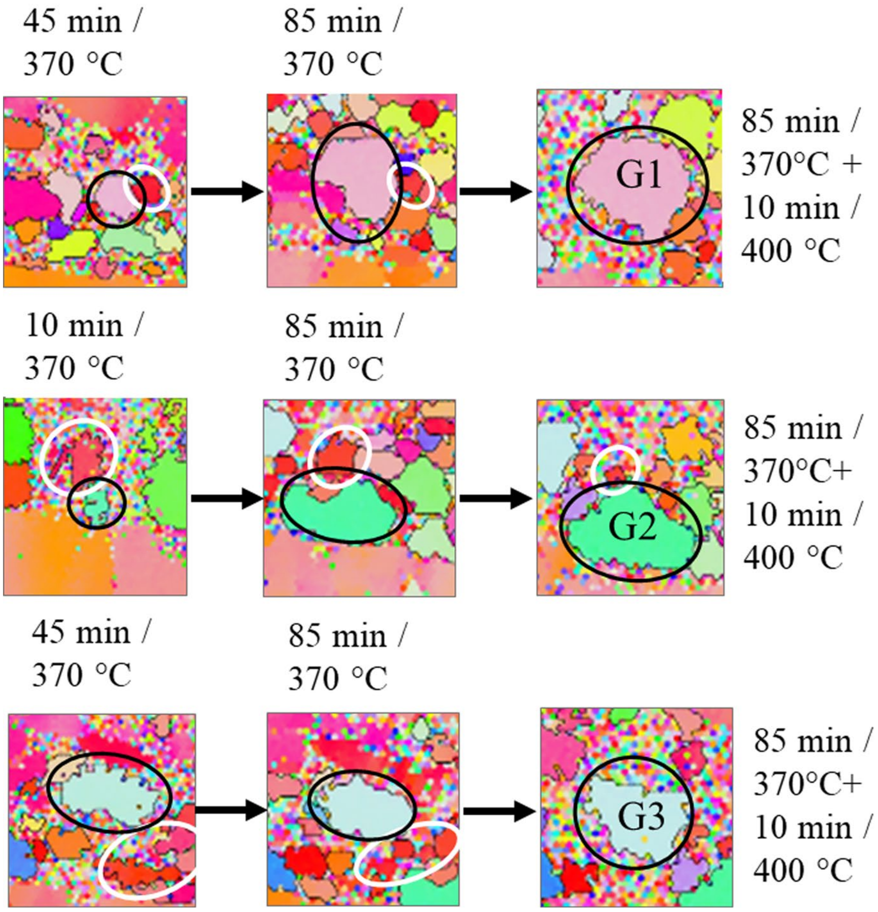

Figure 9 Examples of off-basal recrystallization nuclei G1, G2, and G3 that demonstrate a selective growth behavior at the expense of shrinking, neighboring basal nuclei (white circles). This behavior explains the strengthening of the off-basal texture component shown in Fig. 7g.

(marked by white circles) gradually shrink and disappear from the annealed microstructure, whereas the off-basal nuclei grow to dominate the recrystallization texture (cf. Figs. 7 and 8). The competitive growth behavior between the basal and off-basal nuclei in the deformation bands is currently suspected to be governed by anisotropic solute segregation and resulting drag effect on the boundary migration [5, 16, 27, 28]. Solute co-segregation of both Gd and Zn to grain boundaries is to be expected, for which experimental evidence was found in previous TEM and APT studies [5, 16]. Furthermore, recent research utilizing atomistic simulations has shown that segregation to grain boundaries is of inhomogeneous nature and depends on the local atomic arrangements within the boundaries [16]. While a comprehensive understanding of anisotropic GB segregation is yet to be achieved, its effect on boundary mobility and thus on the formation of favorable RE textures is evident. This study demonstrates the importance of particular nucleation sites in providing off-basal nuclei that prevail during incipient nucleus growth of static recrystallization at the expense of basal-oriented neighbors.

Summary and conclusions

The current study aimed at establishing a correlation between the deformation microstructure, recrystallization nucleation, and texture selection during nucleus growth in a Mg–0.073at%Gd–0.165at%Zn alloy. For this, an as-cast sample was deformed in uniaxial compression at 200 °C till 40% and then cut along the compression direction into two halves. One sample half was kept as is and the other half was annealed at 400 °C for 60 min for comparative EBSD microstructure characterization of the same area. Additionally, quasi-in situ EBSD characterization was conducted on a selected area of interest featuring preferential recrystallization within a double-twin band. The following main conclusions can be drawn from the results:

1. Dynamic recrystallization in the 40% deformed sample in uniaxial compression at 200 °C was restricted due to the alloy composition containing low concentrations of Gd and Zn. This was beneficial for further static recrystallization because a sufficient amount of deformation was still retained in the deformed microstructure. Texture analysis of the few dynamically RX grains revealed good potential for altering the deformation texture by forming new off-basal components.
2. Comparative EBSD microstructure characterization of the same area in the deformed and deformed + annealed samples revealed that static recrystallization after annealing at 400 °C for 60 min was related to specific nucleation sites in the deformation microstructure. For clarity, these sites were assigned to separate regions that included thin double-twin bands and profuse $\left\{10\overline{1}2\right\}$ twining.
3. (0002) pole figures of the deformed and recrystallized counterpart regions revealed a strong qualitative modification of the sharp basal texture developed during uniaxial deformation. The altered recrystallization texture was composed of several off-basal components that could be tracked through site-specific EBSD analysis to recrystallization within $\left\{10\overline{1}2\right\} - \left\{10\overline{1}1\right\}$ double-twin bands and recrystallization within a $\left\{10\overline{1}2\right\}$ heavily-twinned region with numerous twin–parent interfaces and twin–twin intersections.
4. The influential role of double-twin recrystallization in dictating the recrystallization texture was closely examined via a combination of sequential annealing at 400 °C up to 95 min and quasi-in situ EBSD mapping. With progressive annealing, the development of texture and microstructure displayed a selective growth behavior, where the basal nuclei diminished and eventually disappeared from the microstructure, and simultaneously the off-basal nuclei grew to dominate the recrystallization texture.

Acknowledgements

The authors are grateful for financial support from the Deutsche Forschungsgemeinschaft (DFG), Grant No. AL1343/7-1.

Authors' contribution

F. Mouhib contributed to conceptualization, methodology, validation, formal analysis, investigation, data curation, writing—original draft, preparation, and visualization. B. Gao was involved in validation, formal analysis, and investigation. T. Al-Samman contributed to resources, supervision, project administration, conceptualization, writing—review and editing, and funding acquisition. All authors have read and agreed to the published version of the manuscript.

Funding

Open Access funding enabled and organized by Projekt DEAL.

Data availability

The raw/processed data required to reproduce these findings cannot be shared at this time as the data also form part of an ongoing study.

Declarations

Conflict of interest The authors declare that they have no known competing financial interests or personal relationships that could have appeared to influence the work reported in this paper.

Ethical approval Not applicable.

References

[1] Bhattacharyya JJ, Agnew SR, Muralidharan G (2015) Texture enhancement during grain growth of magnesium alloy AZ31B. Acta Mater 86:80–94

[2] Gehrmann R, Frommert MM, Gottstein G (2005) Texture effects on plastic deformation of magnesium. Mater Sci Eng A 395(1–2):338–349

[3] Li MR, Deng DW, Kuo KH (2006) Crystal structure of the hexagonal (Zn, Mg)4Ho and (Zn, Mg)4Er. J Alloys Compd 414(1–2):66–72

[4] Al-Samman T, Li X (2011) Sheet texture modification in magnesium-based alloys by selective rare earth alloying. Mater Sci Eng A 528(10–11):3809–3822

[5] Mouhib F et al (2022) Synergistic effects of solutes on active deformation modes, grain boundary segregation and texture evolution in Mg-Gd-Zn alloys. Mater Sci Eng A 847:143348

[6] Mouhib F-Z et al (2021) Texture selection mechanisms during recrystallization and grain growth of a magnesium-erbium-zinc alloy. Metals 11(1):171

[7] Cui SJ et al (2017) Microstructure and mechanical properties of Mg-Er-Zn alloys with LPSO phase. Mater Sci Forum 898:53–60

[8] Stanford N, Barnett MR (2008) The origin of "rare earth" texture development in extruded Mg-based alloys and its effect on tensile ductility. Mater Sci Eng A 496(1–2):399–408

[9] Stanford N et al (2008) Effect of microalloying with rare-earth elements on the texture of extruded magnesium-based alloys. Scripta Mater 59(7):772–775

[10] Mackenzie L, Pekguleryuz M (2008) The recrystallization and texture of magnesium–zinc–cerium alloys. Scripta Mater 59(6):665–668

[11] Hantzsche K et al (2010) Effect of rare earth additions on microstructure and texture development of magnesium alloy sheets. Scripta Mater 63(7):725–730

[12] Hadorn JP et al (2011) Role of solute in the texture modification during hot deformation of Mg-rare earth alloys. Metall Mater Trans A 43(4):1347–1362

[13] Basu I, Al-Samman T (2014) Triggering rare earth texture modification in magnesium alloys by addition of zinc and zirconium. Acta Mater 67:116–133

[14] Basu I, Al Samman T, Gottstein G (2013) Recrystallization and grain growth related texture and microstructure evolution in two rolled magnesium rare-earth alloys. Mater Sci Forum 765:527–531

[15] Barrett CD et al (2017) Effect of grain boundaries on texture formation during dynamic recrystallization of magnesium alloys. Acta Mater 128:270–283

[16] Pei R et al (2022) Atomistic insights into the inhomogeneous nature of solute segregation to grain boundaries in magnesium. Scripta Mater 230:115432

[17] He C et al (2021) Unusual solute segregation phenomenon in coherent twin boundaries. Nat Commun 12(1):722

[18] Mahjoub R, Stanford N (2021) The electronic origins of the "rare earth" texture effect in magnesium alloys. Sci Rep 11(1):14159

[19] Robson JD (2013) Effect of rare-earth additions on the texture of wrought magnesium alloys: the role of grain boundary segregation. Metall Mater Trans A 45(8):3205–3212

[20] Guan D et al (2018) Individual effect of recrystallisation nucleation sites on texture weakening in a magnesium alloy: Part 2—shear bands. Acta Mater 145:399–412

[21] Guan D et al (2017) Individual effect of recrystallisation nucleation sites on texture weakening in a magnesium alloy: Part 1- double twins. Acta Mater 135:14–24

[22] Jiang MG et al (2021) Quasi-in-situ observing the rare earth texture evolution in an extruded Mg-Zn-Gd alloy with bimodal microstructure. J Magn Alloys 9(5):1797–1805

[23] Hielscher R, Schaeben H (2008) A novel pole figure inversion method: specification of theMTEXalgorithm. J Appl Crystallogr 41(6):1024–1037

[24] Cram DG et al (2012) The effect of solute on discontinuous dynamic recrystallization. Acta Mater 60(18):6390–6404

[25] Griffiths D (2014) Explaining texture weakening and improved formability in magnesium rare earth alloys. Mater Sci Technol 31(1):10–24

[26] Jiang MG et al (2018) Correlation between dynamic recrystallization and formation of rare earth texture in a Mg-Zn-Gd magnesium alloy during extrusion. Sci Rep 8(1):16800

[27] Barrett CD, Imandoust A, El Kadiri H (2018) The effect of rare earth element segregation on grain boundary energy and mobility in magnesium and ensuing texture weakening. Scripta Mater 146:46–50

[28] Stanford N et al (2011) Solute segregation and texture modification in an extruded magnesium alloy containing gadolinium. Scripta Mater 65(10):919–921

7.4 Exploring solute behavior and texture selection in magnesium alloys at the atomistic leve

F. Z. Mouhib[1], Z. Xie[1], A. Atila[2], J. Guenole[3],4, S. Korte-Kerzel[1] and T. Al-Samman[1].
[1]Institute of Physical Metallurgy and Materials Physics, RWTH Aachen University, Germany
[2]Department of Materials Science and Engineering, Saarland University, 66123 Saarbrücken, Germany
[3]Université de Lorraine, CNRS, Arts et Métiers ParisTech, LEM3, 57070 Metz, France
[4]Labex Damas, Université de Lorraine, 57070 Metz, France

Acta Materialia 266 (2024), p. 119677. issn: 1359-6454.

The candidate carried out the conceptualisation, experimental work and data analysis of experimental data, drafted the manuscript and participated in writing and editing. Atomistic calculations and cluster analysis was done by the co-authors

Online availability: https://doi.org/10.1016/j.actamat.2024.119677.

Acta Materialia 266 (2024) 119677

Contents lists available at ScienceDirect

Acta Materialia

journal homepage: www.elsevier.com/locate/actamat

Exploring solute behavior and texture selection in magnesium alloys at the atomistic level

F. Mouhib [a,*], Z. Xie [a,*], A. Atila [b], J. Guénolé [c], S. Korte-Kerzel [a], T. Al-Samman [a]

[a] Institute of Physical Metallurgy and Materials Physics, RWTH Aachen University, Aachen 52056, Germany
[b] Department of Materials Science and Engineering, Saarland University, Saarbrücken 66123, Germany
[c] Université de Lorraine, CNRS, Arts et Métiers ParisTech, LEM3, Metz 57070, France

ARTICLE INFO

Keywords:
Solute segregation
Solute clustering
Solute binding energies
Ab initio calculations
Atom probe tomography
Texture evolution
Magnesium alloys

ABSTRACT

This study advances our understanding of how chemical binding and solute distribution impact grain boundary segregation behavior and subsequent annealing texture modification in lean Mg-X-Zn alloys (X = RE or Ca). Notably, differences in Ca and Gd solute behavior at grain boundaries were revealed, where Ca exhibited stronger binding to vacancy sites than Gd, resulting in elevated Ca segregation and an RD-TD-type texture. The introduction of Zn showed significant synergistic effects on solute clustering, with Gd-Zn pairs forming more favorably than Ca-Zn pairs, leading to a strong synergy between Zn and Gd. This promoted their co-segregation and high concentration at the grain boundary, generating a unique TD-spread texture. In contrast, weaker binding in Ca-Zn pairs did not affect Ca segregation but influenced Zn segregation, which underscores the importance of solute binding behavior in alloy design concepts. Additionally, the combined atomic-scale experiments and ab initio predictions provide strong evidence that selective texture development in Mg alloys is tied to heterogeneous solute-boundary interactions, where the sensitivity of the binding energy to volumetric strain affects solute segregation at grain boundaries, resulting in varying grain boundary mobilities and specific texture component growth. It also emphasizes that solute behavior in clustering and segregation is influenced not only by atomic size but also by chemical binding strength with vacancies or co-added Zn.

1. Introduction

The choice of alloying elements hinges upon the specific requirements and performance criteria of a given application, where solute additions have demonstrated a remarkable capability to significantly enhance and modify the material properties. As such, they have become indispensable to the design of cutting-edge materials. Fundamental research in this area has shown that interactions between solutes and defects play a pivotal role in shaping microstructure formation and influencing the mechanical response of materials [1–3]. This is particularly important in the context of lightweight materials like magnesium (Mg), where dilute alloying with specific solute elements extends the scope of their utility by improving their formability at low temperatures [4].

The addition of rare earth elements (RE) to Mg alloys has proven to be a highly effective strategy for altering the material's texture and enhancing its mechanical properties. Several related studies have consistently reported enhanced ductility, increased yield strength, mitigated anisotropic behavior, and softened annealing textures that respond favorably to an applied strain, compared to common Mg alloys [5–7]. It was established that the large size misfit of RE solutes within the Mg matrix causes solute segregation to grain boundaries (GB) influencing the GB energy and mobility. Combined addition of transition elements, such as zinc (Zn) into Mg-RE alloys induces a negative lattice misfit, giving rise to local solute clusters of Zn and RE atoms with important co-segregation effects on the properties of grain boundaries [8,9]. Numerous studies have demonstrated that the combination of RE elements with Zn intensifies the rare earth effect on texture, resulting in a unique split of basal poles into the transverse direction (TD) of rolled alloy sheets [7,10–13]. In that respect, the available literature points to a correlation between GB solute segregation and an orientation selection process occurring during recrystallization nucleation and growth [9,14]. Proposed mechanisms behind this phenomenon include anisotropic solute drag effects and alterations of the grain boundary structure and properties by the segregated solutes [2,15–19]. A recent atom probe tomography (APT) study on Mg-Gd-Zn alloys has unveiled that the

---

* Corresponding authors.
E-mail addresses: mouhib@imm.rwth-aachen.de (F. Mouhib), xie@imm.rwth-aachen.de (Z. Xie).

https://doi.org/10.1016/j.actamat.2024.119677
Received 20 September 2023; Received in revised form 28 December 2023; Accepted 11 January 2024

synergistic effects of combined solute species on GB segregation and texture selection are contingent not only on the type of solute atoms but also on the relative atomic concentration ratio between them [20].

Given the limited availability and higher cost of RE elements, calcium (Ca) frequently emerges as the preferred alloying element in Mg alloys because it is more abundant and cost-effective. Owing to its relatively large atomic size, it also tends to segregate to grain boundaries, and consequently produce qualitative changes of the texture components [21,22]. However, its co-segregation behavior and associated GB drag effect in ternary alloys still lack clarity. As shown here, the resulting annealing texture in an Mg-Zn-RE alloy diverges, to some extent, from that in a counterpart Mg-Zn-Ca alloy, suggesting dissimilar segregation behaviors. Given that the atomic radius of Ca is similar to that of RE elements, the hypothesized disparity in the mechanistic factors governing texture development implies additional considerations beyond the elastic energy effect due to solute size mismatch. Hence, the present study endeavors to establish a better understanding of how solute interactions within the microstructure correlate with the macroscopic behavior of the investigated materials. This is pursued through a comprehensive approach that combines scale-bridging experiments and ab initio calculations, designed to provide and connect insights into the solute behavior and texture selection, spanning multiple scales of observation.

2. Experiments and methods

2.1. Sample preparation

Binary and ternary Mg-Gd-(Zn) and Mg-Ca-(Zn) were investigated in this study. Their chemical composition, measured by ICP/OES is given in Table 1. The alloys were melted in an induction furnace under a protective Ar/CO_2 gas atmosphere and subsequently cast into a pre-heated copper mold to be finally homogenized at 460 °C for 960 min.

Sheet samples of the dimensions 60 × 40 × 4 mm^3 were machined out of the cast materials and hot rolled at 400 °C (nominal furnace temperature) to 80 % thickness reduction in multiple passes. To refine the microstructure, the final rolling pass was performed at a lower temperature (200 °C). Smaller samples (10 × 12 × 1 mm^3) cut from the rolled sheets were annealed at 400 °C for 60 min in a Heraeus RL200E air furnace. Metallographic sample preparation involved mechanical grinding and polishing of the mid-surface with a diamond suspension up to 0.25 μm. Additionally, all samples were electro-polished in a Struers AC-2 solution using a Lectro-Pol 5 operated at −20 °C and 25 V for 120 s.

2.2. Microstructure characterization

For macrotexture characterization, six incomplete pole figures $[\{10\bar{1}0\}, \{0002\}, \{10\bar{1}1\}, \{10\bar{1}2\}, \{11\bar{1}0\}, \{10\bar{1}3\}]$ were measured using a Bruker D8 advance diffractometer. From these incomplete pole figures, full pole figures and orientation distribution functions (ODFs) were calculated using the texture analysis toolbox MTEX [23]. A dual beam microscope Helios 600i equipped with a HKL-Nordlys II EBSD detector operating at 20 kV was used for EBSD measurements. The used step size varied between 0.5 and 1.5 μm depending on the grain size. The MTEX toolbox was used to analyze the raw EBSD data.

Site-specific preparation of APT tips with general, high-anle grain bounadries, identified through the EBSD measurements, was performed by a coordinated process of focused ion beam (FIB) milling and transmission Kikuchi diffraction (TKD) to ensure a precise position of the GB within the APT tips. The FIB sharpening of the tips was carried in several steps with decreasing beam currents (from 0.43 nA to 40 pA) and milling radii (from 1.5 to 0.1 nm). Subsequently, the elemental distributions of solute atoms in the vicinity of the measured grain boundaries were characterized by 3D APT using a Cameca LEAP 4000X HR in laser-pulsing mode at 30 K. This involved an ultra-violet laser with wavelength of 355 nm, pulse energy of 30 pJ and a pulse rate of 125 kHz maintaining a constant evaporation rate of 0.5 %.

Table 1
Chemical composition of the investigated binary and ternary alloys and their.

Alloys	Gd (at%)	Ca (at%)	Zn (at%)
Mg-Gd	0.142	–	–
Mg-Ca	–	0.150	–
Mg-Gd-Zn	0.148	–	0.165
Mg-Ca-Zn	–	0.150	0.395

2.3. Local solute cluster analysis

To assess the local clustering tendency of multiple solute elements in the reconstructed APT samples, a clustering ratio parameter R_{A-B} is utilized [24].This parameter compares the number of atoms of a particular solute element within a specific cutoff distance r to the expected number of atoms of that element in a homogeneous distribution within the same cutoff. Accordingly, the average number of B atoms within a specific cutoff distance from an A site is calculated using the following equation:

$$\overline{N}_{A-B}(r) = \frac{\sum_{N_A} N_{A-B}(r)}{N_A},$$

where $N_{A-B}(r)$ is the number of B atoms surrounding an A site within r (excluding a potential B atom on the A site) and N_A is the number of A sites. Assuming a homogeneous distribution of B atoms throughout the sample, the ideal number of B atoms within a volume with a cutoff distance r can be calculated as:

$$N_{B,homo}(r) = \frac{4}{3}\pi r^3 \frac{N_B}{V},$$

From that, the clustering ratio R_{A-B} is defined as:

$$R_{A-B} = \frac{\overline{N}_{A-B}(r)}{N_{B,homo}(r)},$$

if $R_{A-B} = 1$, the distribution of B atoms surrounding the A site within a cutoff distance r is considered homogeneous.

For the analysis, the reconstructed APT tips were divided into two regions: a GB region with a thickness of 20 nm along the GB, and a bulk region comprising the remaining part. To calculate the R_{A-B} values for the GB and bulk regions, as well as for the entire tip, the data was normalized using $N_{B,homo,bulk}(r)$, which is obtained based on the number of B atoms in the bulk region, $N_{B,bulk}$, and the corresponding volume, V_{bulk}.

2.4. Density functional theory (DFT) calculations

DFT calculations in the present work were done with the Quantum ESPRESSO package [25] using the projector augmented wave (PAW) [26,27] method and the Perdew-Burke-Ernzerhof (PBE) generalized gradient approximation (GGA) [28] to the exchange-correlation functional. The kinetic energy cutoff was 40 Ry for wave functions and 280 Ry for charge densities and potentials. The convergence threshold for electronic self-consistency was 10^{-8} Ry. For RE solutes, 4f electrons were treated as core electrons in the pseudopotentials. The Broyden-Fletcher-Goldfarb-Shanno (BFGS) relaxation scheme was used for structural relaxation [29]. The convergence thresholds of energy and force are 10^{-4} a.u and 2 × 10^{-4} a.u, respectively. The orthorhombic simulation cells consisted of 4 × 2 × 2 unit cells (64 atoms) with a 6 × 6 × 6 k-point mesh and 5 × 3 × 3 unit cells (180 atoms) with a 4 × 4 × 4 k-point mesh. The solute-vacancy and solute-solute binding energies were calculated by the following equations:

$$E_{\text{bind}}^{\text{vac}-X} = \left(E_{\text{bulk}}^{\text{vac}} + E_{\text{bulk}}^{\text{X}}\right) - \left(E_{\text{bulk}}^{\text{vac}-X} + E_{\text{bulk}}\right), \quad (2.1)$$

$$E_{\text{bind}}^{X-Y} = \left(E_{\text{bulk}}^{\text{X}} + E_{\text{bulk}}^{\text{Y}}\right) - \left(E_{\text{bulk}}^{X-Y} + E_{\text{bulk}}\right), \tag{2.2}$$

where E_{bulk} is the energy of the Mg matrix, $E_{\text{bulk}}^{\text{vac,X,Y}}$ is the energy of the Mg matrix containing one vacancy or a solute atom X or Y, $E_{\text{bulk}}^{\text{vac}-X}$ is the energy of the Mg matrix containing a pair of vacancy and solute atom X, and E_{bulk}^{X-Y} is the energy of the Mg matrix containing a pair of solute atoms X and Y. In the current calculations, a positive binding energy indicates attraction, i.e. a favorable binding. The energies were calculated at 0 K.

3. Results

3.1. Annealing textures

The development of the annealing texture in the Gd-containing alloys reveals notable distinctions in comparison to the counterpart Ca-containing alloys. Fig. 1 shows the (0002) pole figures of the examined binary and ternary Mg-Gd-(Zn) and Mg-Ca-(Zn) alloys after 80 % rolling and subsequent recrystallization annealing at 400 °C for 60 min. In case of the Gd-containing alloy there is a pronounced texture transition from an RD-split texture to a TD-split texture upon the addition of Zn. However, this trend is less evident in the Mg-Ca and Mg-Ca-Zn alloys, where the spread of basal poles and associated maximum densities are almost equal in the RD and TD directions.

3.2. Solute segregation

The spatial distribution of solute atoms at general, high-angle grain boundaries was investigated by means of 3D APT measurements. An overview of the grain boundary angles and axes is given in Table 2.

The reconstructed tips and solute concentration profiles across the measured GB segments are displayed in Fig. 2 for the Mg-Gd-(Zn) and Mg-Ca-(Zn) alloys, respectively. In the case of the Gd-containing alloys, the boundary concentration of Gd in the binary alloy was relatively low (Fig. 2c) in comparison to the ternary alloy upon the introduction of Zn (Fig. 2d) (0.5 at.% vs. 1.5 at.%). Additionally, a significant amount of Zn appears to co-segregate at the GB (1.6 at.%) (Fig. 2d). In the Ca-containing alloys, the GB segregation behavior of Ca was similar in both alloys (2.3 at.% in Mg-Ca vs. 1.9 at.% in Mg-Ca-Zn). Accordingly, the addition of Zn did not seem to enhance the segregation behavior of Ca. The boundary concentration of Zn was lower (0.8 at.%), compared to the Mg-Gd-Zn alloy. The variations in the concentration profiles presented here are discussed later in terms of co-segregation effects and the local atomic environment of the GBs involved, leading to heterogeneous solute segregation phenomena.

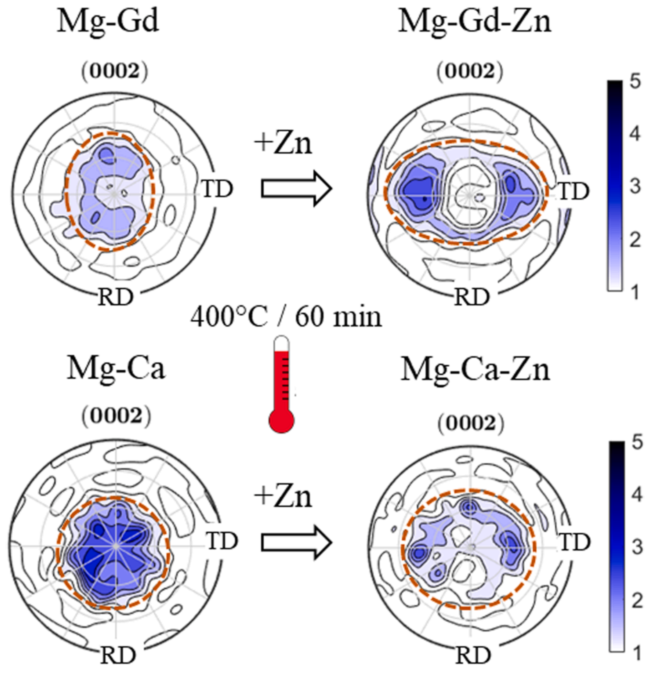

Fig. 1. Comparison of the texture development in Mg-Gd-(Zn) and Mg-Ca-(Zn) alloys upon annealing at 400 °C for 60 min. The color coding for the texture intensities is displayed in terms of multiples of a random distribution. The outlined areas in the (0002) pole figures denote the texture spread with respect to the RD and TD directions.

Table 2
Angles and Axes of the general, high angle grain boundaries in Mg-Ca-(Zn) and Mg-Gd-(Zn) investigated by 3D APT.

Alloys	Angle (°)	Axis (hkil)
Mg-Gd	72.3	$\bar{2}\,3\,\bar{1}\,1$
Mg-Ca	66.6	$\bar{1}\,2\,\bar{1}\,1$
Mg-Gd-Zn	79	$\bar{5}\,6\,\bar{1}\,0$
Mg-Ca-Zn	66.4	$\bar{2}\,3\,\bar{1}\,1$

3.3. Solute clustering

Whether solute atoms are arranged randomly in the solid solution or exhibit specific spatial patterns due to clustering, this aspect can significantly influence the material properties. In order to quantify the measured solute distributions, we employed the clustering ratio R_{A-B} parameter to detect possible solute clusters in the atom probe point cloud data, and examine how the clustering tendency of RE and Ca atoms is influenced by the addition of Zn in the ternary alloys. Fig. 3 shows the R_{A-B} values in the binary and ternary alloys as a function of the cut-off radius for the entire APT tip (solid lines), GB region (short-dashed lines), and the bulk (long-dashed lines). As shown, the R_{A-B} values decrease with an increasing cut-off radius, eventually approaching 1 in the bulk regions. This trend indicates a homogeneous distribution when a sufficiently large space of the measured tips is sampled. By comparison, the R_{A-B} values for the GB region are consistently higher than those for the bulk region, suggesting a more inhomogeneous distribution of solute atoms in the vicinity of grain boundaries in general. Fig. 3a shows a comparison of the Gd-Gd vs. Ca-Ca cluster distribution in the Mg-X system. Note that for the GB region, the $R_{\text{Gd}-\text{Gd}}$ value is higher than the $R_{\text{Ca}-\text{Ca}}$ value within a distance $r <$ 4.5 Å corresponding to second nearest-neighbor (2NN) sites (lattice constant $a = 3.2$ Å). This suggests a less uniform distribution of Gd compared to Ca solutes in the GB for short-range order. In the bulk region, the $R_{\text{Gd}-\text{Gd}}$ value is higher than the $R_{\text{Ca}-\text{Ca}}$ value for all distances. Interestingly, with the addition of Zn (Fig. 3b), the clustering tendency of Ca-Ca solutes in the GB region decreases dramatically, as compared to the binary system. Accordingly, the $R_{\text{Gd}-\text{Gd}}$ value for the GB region is significantly higher than the $R_{\text{Ca}-\text{Ca}}$ value for all the distances considered. As for clustering of Zn-Zn pairs in the ternary alloys, $R_{\text{Zn}-\text{Zn}}$ in the Mg-Gd-Zn alloy was higher than in the Mg-Ca-Zn alloy (Fig. 3c). For the latter, the inhomogeneity of Zn solute distribution in the GB region is comparable to that in the bulk, whereas in the Mg-Gd-Zn alloy, the inclination of Zn-Zn pairs to cluster is more pronounced in the GB region than in the bulk. In Fig. 3d, the plotted $R_{\text{Zn}-X}$ ratio characterizes the tendency for X solute species to cluster around Zn sites, indicating the attraction of Zn solutes to X solutes. As evident, the $R_{\text{Zn}-\text{Gd}}$ ratio notably exceeds the $R_{\text{Zn}-\text{Ca}}$ ratio for all the distances considered, particularly in the GB region (cf. Fig. 3d). This suggests that clustering of Zn-Gd pairs is more favorable than the clustering of Zn and Ca.

3.4. Solute binding

The binding energies of vacancy-X and Zn-X pairs in the Mg matrix were computed using DFT calculations. The vacancy-X binding energy

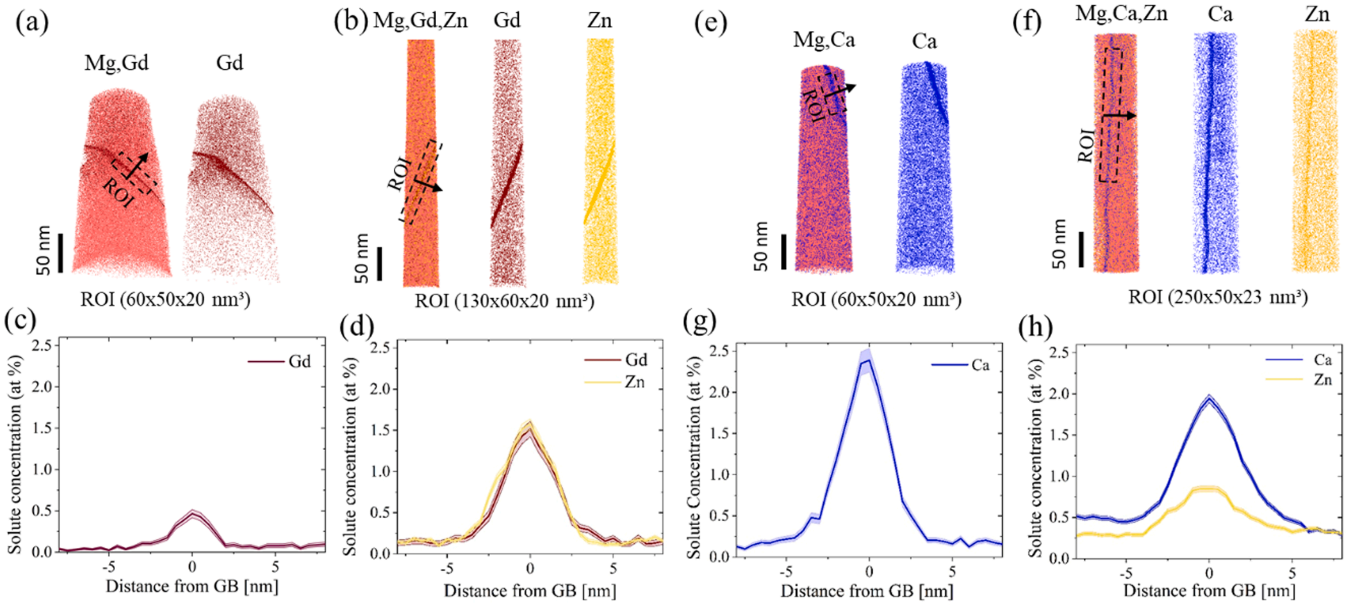

Fig. 2. APT results of the measured tips containing general, high-angle boundaries. (a,b,e,f) 3D elemental distributions of Mg and the solute atoms in the reconstructed tips of the Mg-Gd-(Zn) and Mg-Ca-(Zn) alloys. (c,d,g,h) 1D concentration profiles across the GB. The measurement position and direction are outlined by rectangular regions of interest (ROI) and a marked direction, perpendicular to the GB plane. The GB misorientation angles/axes were the following: 72°$\langle\overline{2}3\overline{1}1\rangle$ (a), 79°$\langle\overline{5}6\overline{1}0\rangle$ (b), 66°$\langle\overline{1}2\overline{1}1\rangle$ (c), 66°$\langle\overline{2}3\overline{1}1\rangle$ (d).

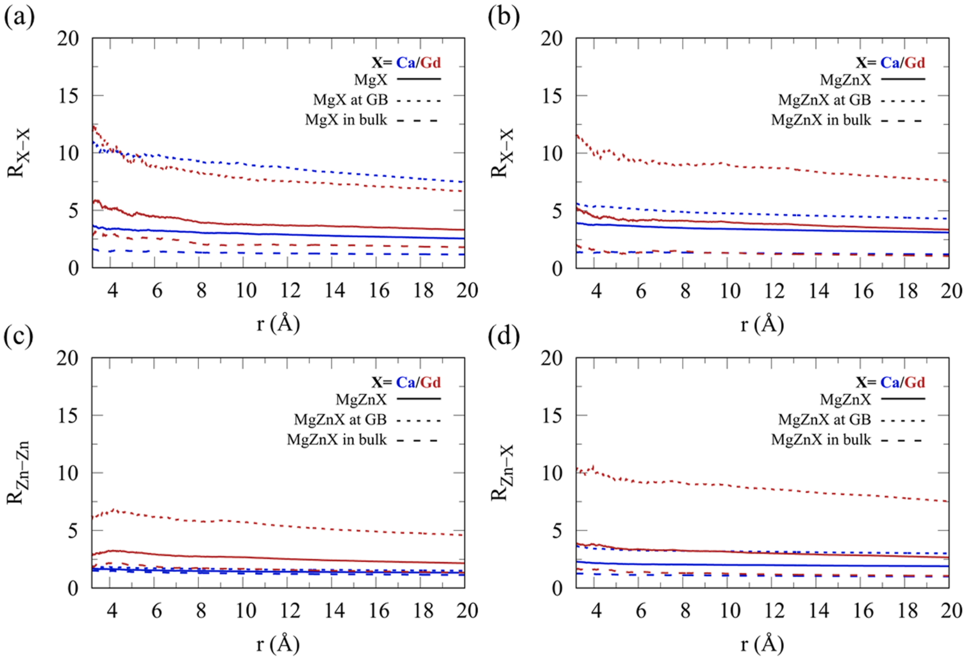

Fig. 3. Clustering analysis of the solute distribution in the reconstructed APT samples as a function of a cutoff distance r. (a) Clustering of X-X atom pairs in binary Mg-X alloys. (b) Clustering of X-X pairs, (c) Zn-Zn pairs, and (d) Zn-X pairs in ternary Mg-X-Zn alloys. X = Gd or Ca.

served as an estimate for the binding of solute X to a GB site with excess free volume compared to the matrix. Meanwhile, the interaction of Zn and X solutes in the ternary alloys was evaluated based on the Zn-X binding energy within the Mg matrix. Fig. 4a shows examples of the orthorhombic simulation cells containing X solute (e. g. Ca) and Zn, as well as a vacancy and X solute (e. g. Gd). When the center feature, i.e. a vacancy or a solute, is placed at the origin of the supercell, there are two possible positions for a first nearest neighbor site. One is on the basal plane with a pair distance of a_0, and the second is on the prismatic plane with a pair distance of $0.577a_0 + 0.5c_0$. Both possibilities were considered when computing the binding energies, resulting in two different energies for each case.

Table 3 summarizes the resulting binding energies for vacancy-X and Zn-X pairs in the binary and ternary alloys. For the binary Mg-X alloys, it was observed that Gd binding to a vacancy was notably less favorable compared to Ca binding to a vacancy. This is evident from the negative value of the vacancy-Gd binding energy, indicating that this binding is energetically unfavorable. In the ternary Mg-X-Zn alloys, the binding energies of Gd and Zn were larger than those of Ca and Zn. This highlights a stronger attraction between Gd-Zn pairs compared to Ca-Zn

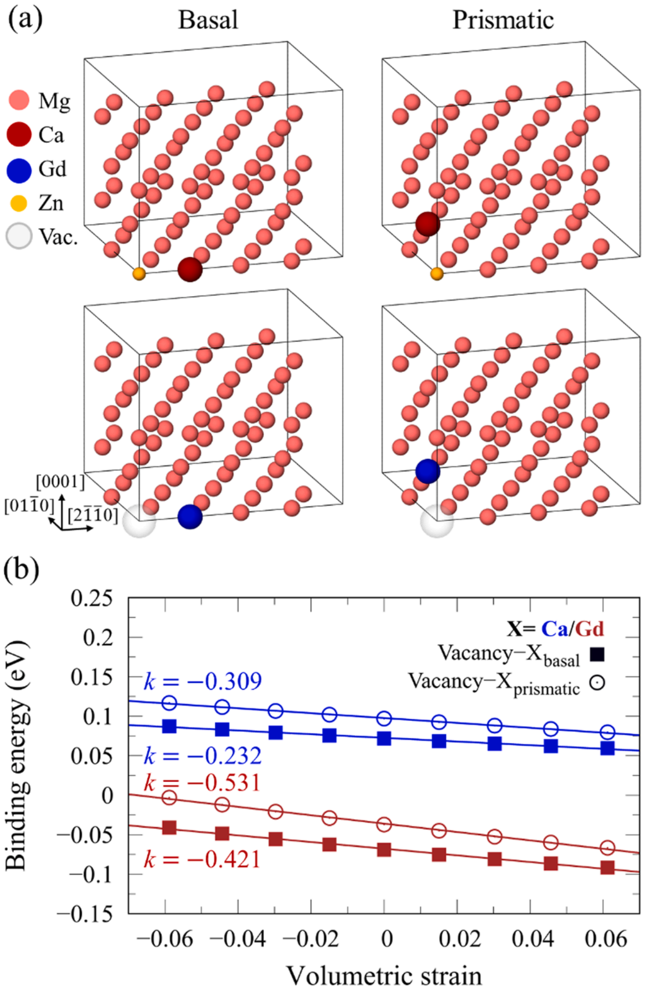

Fig. 4. DFT calculations of the solute-solute and solute-vacancy binding energies in Mg. (a) Orthorhombic simulation cells containing Zn-X and vacancy-X pairs, where either Zn or a vacancy is placed at the origin of the supercell and the solute atom X is placed at the first nearest neighbor on the basal or the prismatic plane. X=Gd or Ca. (b) Volumetric strain-dependent vacancy-X binding energies in 5 × 3 × 3 unit cells (180 atoms). The results were fitted to linear regression with k as the gradient.

Table 3
Ab initio Zn-X and vacancy-X binding energies in 5 × 3 × 3 unit cells (180 atoms).

X	$E_{\mathrm{bind}}^{\mathrm{vac.}-\mathrm{X}}$ (eV)	$E_{\mathrm{bind}}^{\mathrm{Zn}-\mathrm{X}}$ (eV)
$\mathrm{Ca}_{\mathrm{basal}}$	0.072	0.070
$\mathrm{Ca}_{\mathrm{pris.}}$	0.097	0.080
$\mathrm{Gd}_{\mathrm{basal}}$	−0.069	0.083
$\mathrm{Gd}_{\mathrm{pris.}}$	−0.037	0.099

pairs. Notably, the energy associated with binding to a neighbor on the basal plane is consistently less favorable for all cases compared to the prismatic plane.

The volumetric strain-dependent binding energies for vacancy-X pairs were also computed, as illustrated in Fig. 4b. The vacancy-X pairs are energetically more favorable under compressive rather than tensile strain, as evidenced by the linear decrease in binding energies with strain. Interestingly, the binding energies of the vacancy-Ca pairs remain positive even at the maximum tensile strain of 6 %, considered in this work. In contrast, the binding energies of vacancy-Gd pairs appear to be more sensitive to the volumetric strain, with the gradient of the fitted linear function being 1.7 to 1.8 times higher than that of the vacancy-Ca pairs. It is worth noting that the binding energy is anticipated to become positive for vacancy-Gd pairs on the prismatic plane when the compressive strain exceeds 7 %.

4. Discussion

The findings presented in this study highlight important distinctions in the clustering and chemical binding behavior of Ca and Gd in the presence of grain boundaries. Synergistic ternary effects arising from the co-addition of transition elements, such as Zn, were also observed to modify the clustering and binding tendencies of solutes, as compared to the binary systems. In prior DFT calculations [11,12,30,31], the segregation preferences of Ca, Gd and Zn solutes in Mg $\{10\bar{1}1\}$ and $\{10\bar{1}2\}$ twin boundaries, as well as $\Sigma7$ $\{12\bar{3}0\}\langle0001\rangle21.8^\circ$ GBs, were investigated. The per-site segregation energies for these solutes, along with numerous other RE elements, were primarily governed by the minimization of elastic strain energy due to atomic size mismatch. Specifically, Ca and Gd, with larger atomic radii than the Mg matrix, exhibit a preference for segregating at extensive GB sites, while the smaller Zn solute tends to segregate at compressive GB sites. In addition to the elastic energy effect, the effect of chemical binding, encompassing coordination environment and solute electronic configuration, can lead to unusual solute segregation behavior in twin boundaries for specific elements [12]. Notably, these seminal DFT calculations focused primarily on a few GB sites within highly symmetric GB structures, offering only a partial consideration of the broad local atomic environment spectrum. However, it is acknowledged that highly symmetric GBs might not fully capture the complexity of polycrystalline GB environments, potentially leading to incorrect structure-property relationships [32]. To address this limitation, the current work introduces the consideration of solute-vacancy pairs as a scenario within the local atomic environment space characterized by a significant excess of free volume. Similar atomic configurations are commonly observed in various structural units within high-angle symmetric GBs and more general GBs, particularly when the conventional dislocation description falls short. The DFT calculations in this work unveiled that the binding between vacancy sites and Ca solute is energetically more favorable in comparison to Gd. This trend aligns with the aforementioned DFT results on the Mg $\{10\bar{1}2\}$ twin boundary, where it was demonstrated that Ca is more energetically favorable than Gd for segregation at the extensive site [30]. This observation provides a possible explanation for the higher levels of Ca segregation at the grain boundary in the Mg-Ca alloy and the comparatively less pronounced texture spread in the radial direction (RD) compared to its Mg-Gd alloy counterpart. Moreover, it was found that the binding energies between vacancies and Gd solute exhibit high sensitivity to volumetric strain, which would cause an inhomogeneous segregation pattern at GB sites, with analogous local atomic environment and excess free volume. This observation is consistent with the clustering analysis of the APT point cloud data, which illustrate a less uniform Gd solute distribution within a 2NN distance (cf. Fig. 3a). In this context, the presence of an inhomogeneous solute distribution within GBs is likely to influence their mobilities, subsequently impacting the development of texture.

In the ternary alloys, the formation of Gd-Zn pairs proved to be more favorable compared to Ca-Zn pairs. This preference led to a more pronounced synergistic effect of Zn with Gd, consequently enhancing their co-segregation behavior. This effectively explains the similarly high concentration of both Gd and Zn at the GB (Fig. 2d), as well as their pronounced clustering in the GB region (Fig. 3d). Conversely, Ca-Zn pairs exhibited a lower binding energy, which does not seem to strongly influence the individual segregation of Ca to the GB (Fig. 2g) but rather affect the segregation of Zn (Fig. 2h). This observation strongly suggests that the synergistic effect of combined alloying additions depends on their binding behavior. The more attractive the binding, the more effective their synergy in GB co-segregation and texture modification. For additional insights into the role of combined solute addition in promoting the segregation levels, the segregation energy ΔG_{seg} in all four alloys was calculated after the Langmuir-McLean adsorption model represented by Eq. (4.1) (Table 4). X_{GB} represents the peak solute concentration at the grain boundary, and X_M the solute concentration in the matrix [33]. X_M was obtained from the APT data and represents an average of solute concentrations within a region spanning from ± 10 nm to ± 5 nm from the grain boundary within the specified region of interest in Fig. 2.

$$\frac{X_{GB}}{1 - X_{GB}} = \left(\frac{X_M}{1 - X_M}\right) \times \exp\left(-\frac{\Delta G_{seg}}{RT}\right) \tag{4.1}$$

Fig. 5a and b depict a correlation between the peak concentration in the GB and the segregation energy ΔG_{seg} for both binary and ternary alloys. The segregation energies corroborate the solute segregation behavior indicated by the peak concentrations. For instance, in the case of Mg-Gd-Zn, the negative segregation energies of both Gd and Zn are approximately twice as high as those of Ca and Zn in the Mg-Ca-Zn alloy . Conversely, in the binary alloys, the negative segregation energy of Ca is higher than that of Gd (Fig. 5b).

The difference between the synergistic effect of Gd and Ca on Zn segregation at the grain boundary can be effectively correlated with the small, yet favorable difference in the binding energy of −0.019 eV between the Zn-Ca and Zn-Gd pairs. This was shown experimentally to result in a significant enhancement in the peak concentration of Zn at the boundary, increasing from 0.86 at.% to 1.56 at.%, due to the substitution of Ca with Gd. Taking the binding energy difference of −0.019 eV and the estimated Zn segregation energy of −0.059 eV in Mg-Ca-Zn, in addition to the measured Zn bulk concentration of 0.313 at.%, a 38 % enhancement in Zn GB concentration from 0.86 to 1.19 at.% was achieved by replacing Ca with Gd following the Langmuir-McLean model. It is noted that the observed variations in the segregation behavior cannot be solely attributed to co-segregation effects because the tendency for segregation can also depend on the local atomistic details of the GBs involved, and thus on their macroscopic character. The inherent disorder within grain boundaries encompasses a broad variety of local atomic environments that for a given GB site can either attract or repulse solute atoms to varying degrees [34,35].

The observed characteristics in solute-vacancy and solute-solute interactions with respect to binding and segregation are likely to underlie the distinct TD-spread tendency of the annealing texture observed in the Mg-RE-Zn alloy. Notably, the "boost" in the segregation behavior of Gd upon the addition of Zn, causes a pronounced shift of the orientation of maximum intensity in the (0002) pole figure from the RD towards the TD (Fig. 1). This aligns with the literature, which has previously proposed a connection between the spread of texture poles and the segregation of solutes [8,36–38]. However, the current data uniquely reveals that the association between the formation of a TD-split texture and the magnitude of segregation benefits largely from the strong Zn/Gd solute synergy present in the Mg-Gd-Zn alloy. In this regard, it is important to point out that despite a relatively high solute concentration of Ca at the GB in the Mg-Ca-Zn alloy (2 at.%), the resulting annealing texture does not exhibit a significant TD-spread feature akin to that observed in the Mg-Gd-Zn alloy. This is likely due to the weaker attraction between Zn and Ca atoms, resulting in a less pronounced segregation of Zn to the grain boundaries.

Table 4

Local chemical composition for the investigated alloys at the grain boundary (GB) and in the matrix (M) measured by APT and the resulting segregation energy ΔG_{seg} from Eq. (4.1).

Alloy	Ca/Gd GB at (%)	Zn GB at (%)	Ca/Gd M at (%)	Zn M at (%)	ΔG_{seg} (Gd/Ca) (eV/ atom)	ΔG_{seg} (Zn) (eV/ atom)
Mg-Gd	0.466 +/- 0.049	–	0.0536 +/- 0.004	–	−0.126 +/ 0.00009	–
Mg-Gd-Zn	1.516 +/−0.093	1.575 +/- 0.064	0.145 +/- 0.007	0.159 +/- 0.005	−0.137 +/- 0.00004	−0.134 +/- 0.00003
Mg-Ca	2.39 +/- 0.145	–	0.163 +/- 0.007	–	−0.158 +/- 0.00001	–
Mg-Ca-Zn	1.95 +/- 0.051	0.857 +/- 0.034	0.421 +/- 0.005	0.313 +/- 0.004	−0.090 +/- 0.00008	−0.059 +/- 0.0003

The findings presented in this paper provide substantial evidence supporting the notion that the preferential development of specific texture components in Mg alloys is intricately connected to solute segregation through heterogeneous solute-boundary interactions. The reliance of binding energies on volumetric strains implies that solute segregation at grain boundaries is influenced by the local grain boundary structure. Consequently, a non-uniform GB solute distribution leads to varying grain boundary mobilities among different boundaries, facilitating the selective growth of specific texture components. These results align with previous literature that has also proposed anisotropic grain boundary segregation in diverse material systems, exemplary Mg-Mn-Nd, Au-Pt and Fe-B-C [3,16,39].

In the design of wrought magnesium alloys, it is crucial to recognize that achieving texture modification via the incorporation of RE/Ca and Zn alone may not be effective unless there is a sufficient driving force for co-segregation. In this context, the presence of a strong chemical interaction between RE/Ca and Zn emerges as a pivotal factor. Therefore, the segregation behavior and the redistribution of solutes are not solely determined by the minimization of elastic strain energy but are also heavily influenced by the strength of the chemical binding between these elements. The latter aspect is in excellent agreement with a very recent study that employed atomistic simulations to illustrate that solute segregation or depletion in Mg-Al alloys is induced by vacancy clusters [40].

5. Conclusions

The current study has contributed to a clearer understanding of the impact of chemical binding and solute distribution on the segregation behavior at grain boundaries, and the subsequent alteration of the annealing texture in dilute Mg-X-Zn alloys (*X*= RE or Ca). The following conclusions can be drawn:

1. This study reveals key differences in how Ca and Gd behave in the presence of grain boundaries. DFT calculations showed that Ca binds more favorably to sites with excess free volume than Gd, explaining the higher Ca segregation at general grain boundaries and the resulting RD-TD spread texture.
2. The addition of a transition element (Zn) had significant synergistic effects on solute clustering and binding. Gd-Zn pairs formed more favorably than Ca-Zn pairs, leading to a stronger synergistic effect between Zn and Gd. This observation, in conjunction with the variations arising from different grain boundary characters, provides a plausible explanation for the equally high concentrations of Gd and Zn at the grain boundary, ultimately contributing to the observed TD-spread texture.
3. In contrast, Ca-Zn pairs exhibited weaker binding, showing no influence on Ca segregation to the grain boundary but impacting Zn segregation. In terms of alloy design, this highlights a crucial aspect that the efficacy of alloying elements depends on the binding behavior of co-added solutes. In other words, stronger binding could enhance the synergy for grain boundary co-segregation and texture modification.
4. The DFT predictions and experiments offer substantial evidence that the selective formation of specific texture components in Mg alloys is closely tied to heterogeneous solute-boundary interactions. The fact

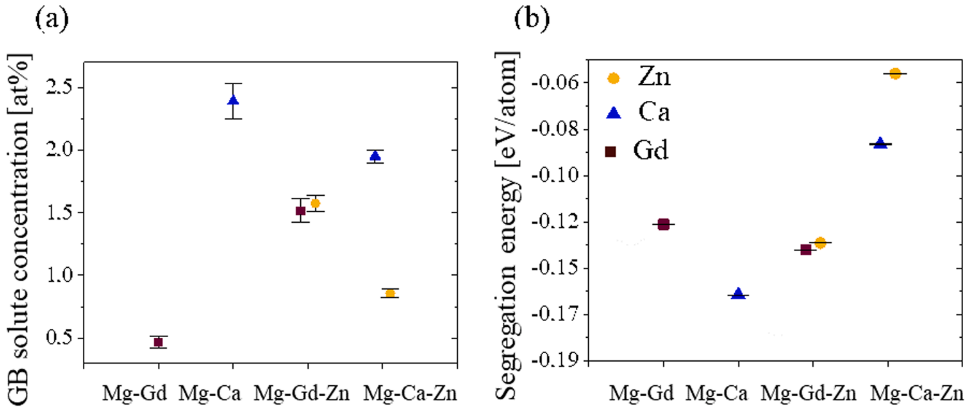

Fig. 5. (a) Peak concentration of solute at the GB in Mg-Gd, Mg-Ca, Mg-Gd-Zn and Mg-Ca-Zn . (b) The corresponding GB segregation energy.

that the binding energy can be sensitive to the volumetric strain suggests that solute segregation at grain boundaries is influenced by the local grain boundary structure. Consequently, an uneven distribution of solutes along grain boundaries results in varying grain boundary mobilities, enabling the preferential growth of specific texture components.

5. Solute behavior regarding clustering and segregation is shaped not only by the large atomic size of RE and Ca, and the resulting elastic strain energy minimization, but also by the considerable impact of the chemical binding strength, either with sites with excess free volume or with co-added Zn in the ternary alloys.

Declaration of competing interest

The authors declare that they have no known competing financial interests or personal relationships that could have appeared to influence the work reported in this paper.

Acknowledgements

F.M., and T.A.S. are grateful for the financial support from the German Research Foundation (DFG) (Grant Nr. AL1343/7-1). Z.X. and T.A.S. acknowledge the financial support by the DFG (Grant Nr. 505716422). Z.X. and S.K.K. acknowledge the financial support by the DFG through the SFB1394 Structural and Chemical Atomic Complexity – From Defect Phase Diagrams to Material Properties, project ID 409476157. J.G. acknowledges funding from the French National Research Agency (ANR), Grant ANR-21-CE08-0001 (ATOUUM) and ANR-22-CE92-0058-01 (SILA). Simulations were performed with computing resources granted by RWTH Aachen University under project (p0020267).

Supplementary materials

Supplementary material associated with this article can be found, in the online version, at doi:10.1016/j.actamat.2024.119677.

References

[1] J.J. Bhattacharyya, S.R. Agnew, G. Muralidharan, Texture enhancement during grain growth of magnesium alloy AZ31B, Acta Mater. 86 (2015) 80–94.
[2] R. Pei, et al., Solute drag-controlled grain growth in magnesium investigated by quasi *in-situ* orientation mapping and level-set simulations, J. Magnes. Alloys 11 (2023) 2312–2325.
[3] X. Zhou, et al., Atomic motifs govern the decoration of grain boundaries by interstitial solutes, Nat. Commun. 14 (1) (2023) 3535.
[4] C.D. Barrett, H. El Kadiri, R. Moser, Generalized interfacial fault energies, Int. J. Solids Struct. 110-111 (2017) 106–112.
[5] I. Basu, T. Al Samman, G. Gottstein, Recrystallization and grain growth related texture and microstructure evolution in two rolled magnesium rare-earth alloys, Mater. Sci. Forum 765 (2013) 527–531.
[6] J.P. Hadorn, et al., Role of solute in the texture modification during hot deformation of Mg-rare earth alloys, Metall. Mater. Trans. A 43 (4) (2011) 1347–1362.
[7] F.Z. Mouhib, et al., Texture selection mechanisms during recrystallization and grain growth of a magnesium-erbium-zinc alloy, Metals 11 (1) (2021).
[8] J.F. Nie, et al., Solute segregation and precipitation in a creep-resistant Mg–Gd–Zn alloy, Acta Mater. 56 (20) (2008) 6061–6076.
[9] A. Imandoust, et al., A review on the effect of rare-earth elements on texture evolution during processing of magnesium alloys, J. Mater. Sci. 52 (1) (2016) 1–29.
[10] X.H. Shao, et al., Atomic-scale segregations at the deformation-induced symmetrical boundary in an Mg-Zn-Y alloy, Acta Mater. 118 (2016) 177–186.
[11] J.F. Nie, et al., Periodic segregation of solute atoms in fully coherent twin boundaries, Science 340 (6135) (2013) 957–960.
[12] C. He, et al., Unusual solute segregation phenomenon in coherent twin boundaries, Nat. Commun. 12 (1) (2021) 722.
[13] I. Basu, T. Al-Samman, Triggering rare earth texture modification in magnesium alloys by addition of zinc and zirconium, Acta Mater. 67 (2014) 116–133.
[14] D. Guan, et al., Exploring the mechanism of “Rare Earth” texture evolution in a lean Mg–Zn–Ca alloy, Sci. Rep. 9 (2019) 7152.
[15] R. Pei, et al., Grain boundary co-segregation in magnesium alloys with multiple substitutional elements, Acta Mater. 208 (2021) 116749.
[16] Pei, R., et al., Atomistic origin of the anisotropic grain boundary segregation in a Mg-Mn-Nd alloy. Archived on arXiv, 2022.
[17] M.I. Mendelev, D.J. Srolovitz, Co-segregation effects on boundary migration, Interface Sci. 10 (2002) 191–199.
[18] R. Mahjoub, N. Stanford, The electronic origins of the "rare earth" texture effect in magnesium alloys, Sci. Rep. 11 (1) (2021) 14159.
[19] C.D. Barrett, A. Imandoust, H. El Kadiri, The effect of rare earth element segregation on grain boundary energy and mobility in magnesium and ensuing texture weakening, Scr. Mater. 146 (2018) 46–50.
[20] F. Mouhib, et al., Synergistic effects of solutes on active deformation modes, grain boundary segregation and texture evolution in Mg-Gd-Zn alloys, Mater. Sci. Eng. A 847 (2022) 143348.
[21] Y.Z. Du, et al., Effect of microalloying with Ca on the microstructure and mechanical properties of Mg-6 mass%Zn alloys, Mater. Des. 98 (2016) 285–293.
[22] Z.R. Zeng, et al., Effects of dilute additions of Zn and Ca on ductility of magnesium alloy sheet, Mater. Sci. Eng. A 674 (2016) 459–471.
[23] R. Hielscher, H. Schaeben, A novel pole figure inversion method: specification of the MTEXalgorithm, J. Appl. Crystallogr. 41 (6) (2008) 1024–1037.
[24] A. Tilocca, Structure and dynamics of bioactive phosphosilicate glasses and melts from ab initio molecular dynamics simulations, Phys. Rev. B 76 (22) (2007) 224202.
[25] P. Giannozzi, et al., Quantum Espresso: a modular and open-source software project for quantum simulations of materials, J. Phys. Condens. Matter 21 (39) (2009) 395502.
[26] G. Kresse, D. Joubert, From ultrasoft pseudopotentials to the projector augmented-wave method, Phys. Rev. B 59 (3) (1999) 1758–1775.
[27] P.E. Blöchl, Projector augmented-wave method, Phys. Rev. B 50 (24) (1994) 17953–17979.
[28] J.P. Perdew, K. Burke, M. Ernzerhof, Generalized gradient approximation made simple, Phys. Rev. Lett. 77 (18) (1996) 3865–3868.
[29] R. Fletcher, Practical Methods of Optimization, John Wiley & Sons, 2000.
[30] Z. Huang, J.F. Nie, Interaction between hydrogen and solute atoms in $\{10\bar{1}2\}$ twin boundary and its impact on boundary cohesion in magnesium, Acta Mater. 214 (2021) 117009.
[31] L. Huber, J. Rottler, M. Militzer, Atomistic simulations of the interaction of alloying elements with grain boundaries in Mg, Acta Mater. 80 (2014) 194–204.
[32] M. Wagih, C.A. Schuh, Viewpoint: can symmetric tilt grain boundaries represent polycrystals? Scr. Mater. 237 (2023) 115716.
[33] D. McLean, A. Maradudin, Grain boundaries in metals, Phys. Today 11 (7) (1958) 35–36.

[34] T. Nenninger, F. Sansoz, Local atomic environment analysis of short and long-range solute-solute interactions in a symmetric tilt grain boundary, Scr. Mater. 222 (2023) 115045.

[35] R. Pei, et al., Atomistic insights into the inhomogeneous nature of solute segregation to grain boundaries in magnesium, Scr. Mater. 230 (2023) 115432.

[36] F.Z. Mouhib, et al., Texture selection mechanisms during recrystallization and grain growth of a magnesium-erbium-zinc alloy, Metals 11 (1) (2021) 171.

[37] M.G. Jiang, et al., Correlation between dynamic recrystallization and formation of rare earth texture in a Mg-Zn-Gd magnesium alloy during extrusion, Sci. Rep. 8 (1) (2018) 16800.

[38] M.G. Jiang, et al., Quasi-*in-situ* observing the rare earth texture evolution in an extruded Mg-Zn-Gd alloy with bimodal microstructure, J. Magnes. Alloys 9 (2020) 1797–1805.

[39] C.M. Barr, et al., The role of grain boundary character in solute segregation and thermal stability of nanocrystalline Pt-Au, Nanoscale 13 (6) (2021) 3552–3563.

[40] P. Yi, et al., The interplay between solute atoms and vacancy clusters in magnesium alloys, Acta Mater. 249 (2023) 118805.

7.5 Basal Slip in laves Phases: The synchroshear dislocation

J. Guenole[1], F. Z. Mouhib[1], L. Huber[2], B. Grabowski[1]2 and S. Korte-Kerzel[1]. [1]Institute of Physical Metallurgy and Materials Physics, RWTH Aachen University, Germany
[2]Max-Planck-Institut für Eisenforschung GmbH, Max-Planck-Str. 1, D-40237 Düsseldorf, Germany

Scripta Materialia 166 (2019). issn: 1359-6462.

The candidate carried out the preliminary molecular statics and ab initio calculations, and participated in data analysis and the production of figures.

Online availability: https://doi.org/10.1016/j.scriptamat.2019.03.016.

Scripta Materialia 166 (2019) 134–138

Contents lists available at ScienceDirect

Scripta Materialia

journal homepage: www.elsevier.com/locate/scriptamat

Basal slip in laves phases: The synchroshear dislocation

Julien Guénolé [a,*], Fatim-Zahra Mouhib [a], Liam Huber [b], Blazej Grabowski [b], Sandra Korte-Kerzel [a]

[a] *Institute of Physical Metallurgy and Metal Physics, RWTH Aachen University, D-52056 Aachen, Germany*
[b] *Max-Planck-Institut für Eisenforschung GmbH, Max-Planck-Str. 1, D-40237 Düsseldorf, Germany*

ARTICLE INFO

Article history:
Received 4 February 2019
Received in revised form 11 March 2019
Accepted 12 March 2019
Available online xxxx

Keywords:
Plasticity
Complex alloys
Intermetallic
Atomistic simulations
Nudge elastic band

ABSTRACT

Two different mechanisms have been reported in previous *ab initio* studies to describe basal slip in complex intermetallic Laves phases: synchroshear and undulating slip. To date, no clear answer has been given on which is the energetically favourable mechanism and whether either of them could effectively propagate as a dislocation. Using classical atomistic simulations supported by *ab initio* calculations, the present work removes the ambiguity and shows that the two mechanisms are, in fact, identical. Furthermore, we establish synchroshear as the mechanism for propagating dislocations within the basal plane in Laves phases.

*Corresponding author.

Laves phases are intermetallic compounds that form in many alloys and can play a crucial role in their deformation [1,2]. Understanding the *intrinsic* deformation behaviour of Laves phases is critical and many activities have been initiated in that direction [3–12]. Laves phases can be cubic (C15) or hexagonal (C14 and C36) layered structures with the archetypal chemical compositions of Cu_2Mg, Zn_2Mg and Ni_2Mg. The lattice consists of two structural units: a single layer formed of large atoms and a triple layer mixing small and large atoms. For the hexagonal structures, these layers form the basal planes. In their pioneering work, Hazzledine et al. [3,4] predicted basal-slip to occur *via* a synchroshear mechanism [13] that reorganises the stacking of the layered structure by the motion of a synchroshockley dislocation within the triple layer, that is the synchronous glide of two ordinary Shockleys on adjacent parallel atomic planes. The Burgers vector of a synchroshockley dislocation is $\boldsymbol{b_s} = {}^1/_3\langle 10\bar{1}0\rangle$ and the glide of two synchroshockleys leads to the regular Burgers vector $\boldsymbol{b} = {}^1/_3\langle 11\bar{2}0\rangle$ [3]. More details on the Laves phase crystallography can be found in the references or in the Supplementary materials.

The first experimental observation of a basal dislocation core in a Laves phase was reported by Chisholm et al. [5] in C14 Cr_2Hf and was attributed to a synchroshockley. Atomistic studies of the basal slip in C14 Cr_2Nb have revealed two apparently different slip mechanisms. Based on *ab initio* calculations, Vedmedenko et al. [7] reported the experimentally observed synchroshear mechanism (SS), whereas Zhang et al. [8] reported a new mechanism called undulating slip (US). SS is described as the synchronous glide of two partials in the basal plane without any out-of-plane motion. Although no details on the dynamics of this mechanism are known, its activation energy is significantly lower than for classical crystallographic shear [7]. US also consists of the glide of two partials in the basal plane, but is assumed to have a different Burgers vector than SS and proceeds dynamically in three stages: 1) an elastic motion (termed crystallographic slip in [8]), 2) a plastic motion involving breaking of atomic bonds and atomic shuffling, and again 3) elastic motion/crystallographic slip. Note that the term “crystallographic slip” used in [8] can be seen as controversial since there is no atomic sliding at this stage. So far, no study has attempted to differentiate SS and US in any detail. In the present work, we address this point and show that US is in fact not a new mechanism, but rather the same as SS. This is accomplished using the nudge elastic band (NEB) approach and classical atomistic simulations supported by *ab initio* calculations.

The NEB method enables the calculation of both the minimum energy path (MEP) and the associated activation energy (or energy barrier E_b) of a mechanism [14–16]. NEB makes no assumption about the MEP besides the initial guess for the path, for which we use a linear interpolation of particle positions between an initial and a finale stable configuration. It is thus a well suited tool to assess unknown dislocation mechanisms, as for nucleation [17] or core transformations [18]. Relying on a recently developed interatomic potential [19], we study here basal slip in the Laves phase. While NEB has been used previously to study this effect with *ab initio* methods [7,8], these studies were limited to relatively small system sizes and the partial slip only, *i.e.* the transformation of a triple layer from a C14 to a C15 stacking. This restricts the degrees of freedom available for the system to use during slip. By using a classical potential, we can investigate larger system sizes and avoid imposing such constraints. The potential uses the modified

---

[*] Corresponding author.
E-mail address: guenole@imm.rwth-aachen.de (J. Guénolé).

https://doi.org/10.1016/j.scriptamat.2019.03.016

embedded energy method (MEAM) framework to accurately describe the mechanical properties of Mg-Ca compounds, in particular the C14 Mg_2Ca Laves phase [19]. Additionally, we have validated bulk properties of this phase against *ab initio* calculations performed with the Vienna *Ab-initio* Simulation Package (VASP) using the projector augmented wave method (See Supplementary materials).

Fig. 1a shows the generalized stacking fault energy (GSFE) for the basal slip as calculated in this work with the MEAM potential. Slip directions $\langle 11\bar{2}0\rangle$ and $\langle 10\bar{1}0\rangle$ are indicated by red and blue solid lines, respectively. The red and blue lines also correspond to the linearly interpolated initial configurations for the NEB in the case of slip in $\langle 11\bar{2}0\rangle$ and $\langle 10\bar{1}0\rangle$ directions, respectively. Note however that, while the GSFE contains the energy path of the crystallographic slip mechanism as considered in the NEB calculations, the calculation procedures are different. The GSFE is computed with the commonly used *free* boundary conditions in the direction normal to the glide plane, whereas the NEB calculations employ *periodic* boundary conditions in all directions. To ensure a constant strain state throughout the NEB calculations, the initial configuration has been elastically strained with a shear equivalent to a full Burgers vector such as to correspond to the plastic strain of the final configuration. Thus, configuration A exhibits a higher energy than configuration B in all computed NEB energy profiles (Figs. 1b, 2a, 3).

In order to assess the energy associated with mechanisms other than pure crystallographic slip, we performed NEB minimizations to reduce the force norms below 0.02 eV/Å using the quickmin algorithm as implemented in Lammps [16,20]. Due to the complexity of the system, it was necessary to add a spring force perpendicular to the path to converge the calculations, as proposed by Maras et al. [16]. The initial NEB

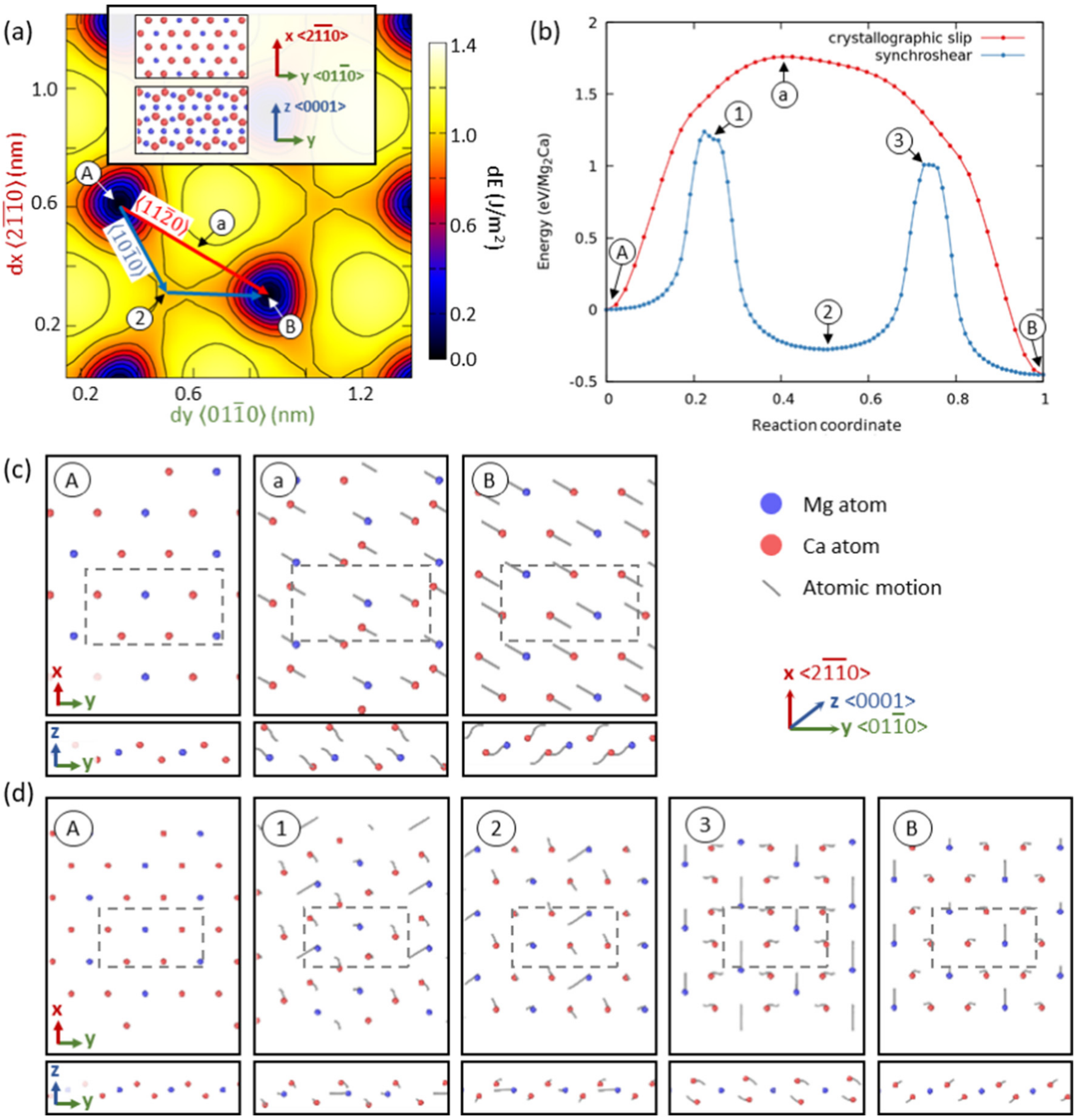

Fig. 1. Basal slip in the C14 Mg_2Ca Laves phase. (a) Generalized stacking fault energy (GSFE) surface obtain with the MEAM potential. Slip directions $\langle 11\bar{2}0\rangle$ and $\langle 10\bar{1}0\rangle$ are indicated with red and blue arrows, respectively. Inset: detail of the layered structure. (b) Energy path for the full slip with two mechanisms: crystallographic slip (red curve) and synchroshear (blue curve). The synchroshear is the minimum energy path. The overall change from reaction coordinate 0 to 1 corresponds to the full slip $^1/_3\langle 11\bar{2}0\rangle$. Energy in eV per Mg_2Ca unit. Mg_2Ca units divide the basal plane in areas formed of 2 Mg and 1 Ca, each belonging in a different sublayer of the triple layer. Snapshots of the corresponding mechanisms for (c) the crystallographic slip and (d) the synchroshear. The upper (lower) boxes show the perpendicular (parallel) views of the basal plane. The boundary of the periodic simulation box is indicated as a dashed box. The motion of the atoms from the previous snapshot are indicated with grey lines. Mg and Ca atoms are coloured in blue and red, respectively. (For interpretation of the references to colour in this figure legend, the reader is referred to the web version of this article.)

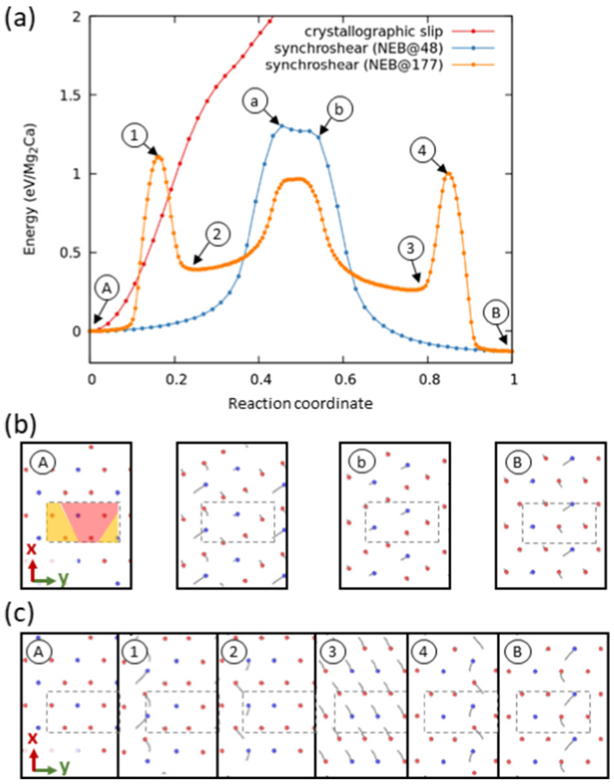

Fig. 2. Propagating basal slip in the C14 Mg_2Ca Laves phase. (a) Energy path for the partial slip with two mechanisms: crystallographic slip (red curve) and single synchroshear (red and orange curves). The synchroshear is the minimum energy path, as obtained by NEB with 48 and 177 intermediate images for the blue and orange curve, respectively. The overall change from reaction coordinate 0 to 1 corresponds to the partial slip $^1/_3\langle 10\bar{1}0\rangle$. Basal plane snapshots of the corresponding synchroshear mechanisms with (b) 48 and (c) 177 NEB intermediate configurations. The inset numbers in black circles correspond to the intermediate configurations in (a). The periodic simulation box consisting on two Mg_2Ca units is indicated as a dashed box. Units' areas are highlighted in yellow and red transparent filling colour. The motion of the atoms from the previous snapshot are indicated with grey lines. The crystallographic orientations are the same as in Fig. 1. (For interpretation of the references to colour in this figure legend, the reader is referred to the web version of this article.)

configurations have been linearly interpolated between the two perfect C14 Mg_2Ca configurations labelled A and B (Fig. 1a, red line), consisting of a fully periodic system of $1 \times 2 \times 20$ unit cells (480 atoms) with the z-axis normal to the basal plane. The computed MEP (Fig. 1b, blue line) exhibits a profile with two maxima and an energy barrier lower than for the crystallographic slip. The associated atomistic mechanism within the triple layer is shown in Fig. 1d. The Ca atoms slip in $\langle 10\bar{1}0\rangle$ directions for each of the MEP peaks (configurations 1 and 3), corresponding to a motion of the Mg atoms along $\langle 1\bar{1}00\rangle$ directions. For each peak, the *absolute* glide of the Ca atoms corresponds to $^1/_6\langle 10\bar{1}0\rangle$, but the glide of the top-layer Ca atoms *relative* to the bottom-layer Ca atoms corresponds exactly to $^1/_3\langle 10\bar{1}0\rangle$. The total shear is $^1/_3\langle 11\bar{2}0\rangle$ as expected. Simultaneously, the glide of the middle-layer Mg atoms is $^1/_3\langle 10\bar{1}0\rangle$. Without any assumption on the mechanism beside the Burgers vector of the full slip and that the linear interpolation lies in the same energy well as the MEP, it is clear that the MEP of a full shear in the C14 Mg_2Al structure corresponds exactly to two successive SSs [5,7].

Based on the above results and a re-interpretation of results from Ref. [8], we can now identify US as the same mechanism as SS. First, we focus on the energy barriers, E_b. The E_b computed in Ref. [8] for US in C14 Cr_2Nb (0.28 eV/Cr_2Nb) is nearly the same as the E_b of SS in the same system (0.29 eV/Cr_2Nb) [7]. Further, the E_b calculated for SS in Ref. [8] (0.41 eV/Cr_2Nb) is surprisingly close to the peak energy of the *unrelaxed* SS (0.42 eV/Cr_2Nb) [7]. This indicates that the MEP attributed in Ref. [8] to US is in fact the one of *relaxed* SS. Now we focus on the Burgers vector. For US, the plastic motion of the intermediate atomic layer was observed to be *perpendicular* to the slip direction, *i.e.*, along $\langle 11\bar{2}0\rangle$ [8]. This motion thus seems to be incompatible with that of SS, which is purely along $\langle 10\bar{1}0\rangle$. However, the plastic motion for the US is preceded and followed by a purely elastic motion. To evaluate the Burgers vector of the slip, the full process including the elastic and plastic motion needs to be considered. Hence, summing up the elastic motion with the plastic motion, the total motion of the intermediate layer is along the $\langle 10\bar{1}0\rangle$ direction, exactly as predicted for SS. We thus conclude that all features of US are already captured by the dynamics of SS and therefore US is not a new mechanism for basal slip in C14 structures.

To investigate the SS dynamics further, we studied slip in the $\langle 10\bar{1}0\rangle$ direction in greater detail. Fig. 2a shows the energy path of the crystallographic slip as well as the MEP of the SS mechanism in the $\langle 10\bar{1}0\rangle$ direction. The SS MEP has been obtained by NEB, with the initial configurations linearly interpolated between perfect and faulted C14 Mg_2Ca configurations A and B, respectively. By faulted, we mean that one of the triple layers of the C14 structure is in the C15 configuration, *i.e.* it has been displaced according to the SS mechanism. As in our previous simulations, the initial configuration A has been strained and the periodic simulation box consists of $1 \times 2 \times 20$ units cells, *i.e.*, two Mg_2Ca units in the basal plane (Fig. 2b,c dashed box).

The MEP^{48} and MEP^{177} obtained with 48 and 177 intermediate configurations, respectively, exhibit completely different profiles (Fig. 2a). Using additional intermediate configurations enables the NEB minimization to find a lower energy transition mechanism. Thus the MEP^{177} gives the most energetically favourable mechanism. The MEP^{48} and MEP^{177} consist of two and three maxima, respectively. This difference originates from the atomistic mechanisms detailed in Fig. 2b,c. The MEP^{48} exhibits a broad peak that corresponds to the atomic shuffling of the Mg and Ca atoms, preceded and followed by purely elastic shear (Fig. 2b). Meanwhile, the first maximum in the MEP^{177} corresponds to the shuffling of the Mg/Ca atoms in the first Mg_2Ca unit (Fig. 2c, configuration 1). The second maximum is related to a purely elastic shear of the entire system that occurs between configuration 2 and 3. The third maximum is finally related to the shuffling of the Mg/Ca atoms in the second Mg_2Ca unit (Fig. 2c, configuration 5). In both cases, the overall mechanism is a synchroshear.

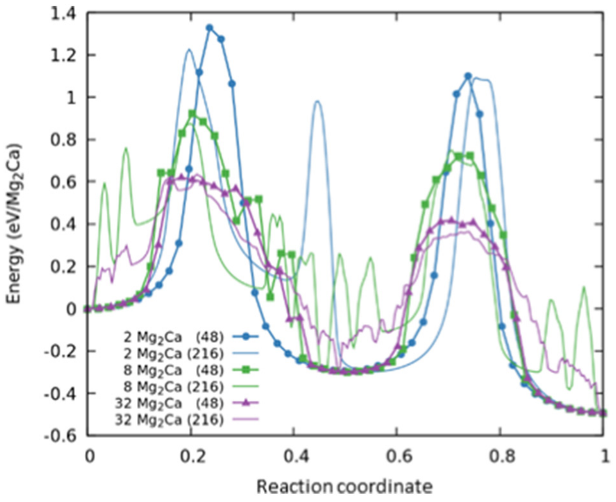

Fig. 3. Basal slip in the C14 Mg_2Ca Laves phase in bulk systems of different periodic dimension. Minimum energy path computed for a full slip by NEB with 48 (216) images in thick (thin) solid lines. The overall change from reaction coordinate 0 to 1 corresponds to the full slip $^1/_3\langle 11\bar{2}0\rangle$. Note that the blue thick curve is identical to that in Fig. 1b. (For interpretation of the references to colour in this figure legend, the reader is referred to the web version of this article.)

In parallel, we have performed *ab initio* NEB calculations in a C14 Mg_2Ca system of 1 × 2 × 2 unit cells (48 atoms). While significantly more computationally expensive, this framework enables more accurate calculations than semi-empirical potentials. We observe that the MEP of the basal slip remains associated with SS, and that the associated energy barrier is in good agreement with the MEAM potential (see Section 3.3 and Movie 1 in Supplementary materials). These qualitative and quantitative DFT calculations validate the results we obtained with the MEAM potential.

It appears that SS as computed by NEB is a slip that is divided into two phases: an atomic shuffling and an elastic straining. With sufficient degrees of freedom (DoF), a lower energy path than collective SS can be found, by inducing an asynchronous atomic shuffling of the different C14 units within the basal plane. We confirmed this last statement by studying larger systems, which intrinsically increase the DoF of the NEB process. Fig. 3 shows the MEP for a full-slip $^1/_3\langle 11\bar{2}0\rangle$ in the basal plane of systems with 1 × 2 × 20 (480 atoms), 2 × 4 × 20 (1920 atoms) and 4 × 8 × 20 (7680 atoms) unit cells, resulting in 2, 8 and 32 Mg_2Ca units in the basal plane, respectively. The smallest system is identical to the one presented above (Fig. 1b). Note that varying the number of NEB intermediate configurations increases the number of local maxima in the MEP. This is related to the shuffling of individual Mg_2Ca units, but does not alter the mechanism and does not change the value of E_b significantly (Fig. 3, and Supplementary materials). The E_b clearly decreases with the number of Mg_2Ca units in the basal plane, consistent with the asynchronous process described above. The overall associated mechanism is always a double SS. The decrease of E_b originates in the details of the slip, in particular its irregularity (see Movies 2 and 3 in Supplementary materials). Indeed, the motion of a particular atom is required to initiate the slip but is unfavourable since it increases the overall energy of the system. It is then more efficient to initiate the motion on one part of the system, and then to propagate it through the entire plane. This is the fundamental reason for dislocations as plasticity carriers in crystalline materials [21] and therefore confirms SS as a robust mechanism for dislocation propagation in bulk C14 Mg_2Ca.

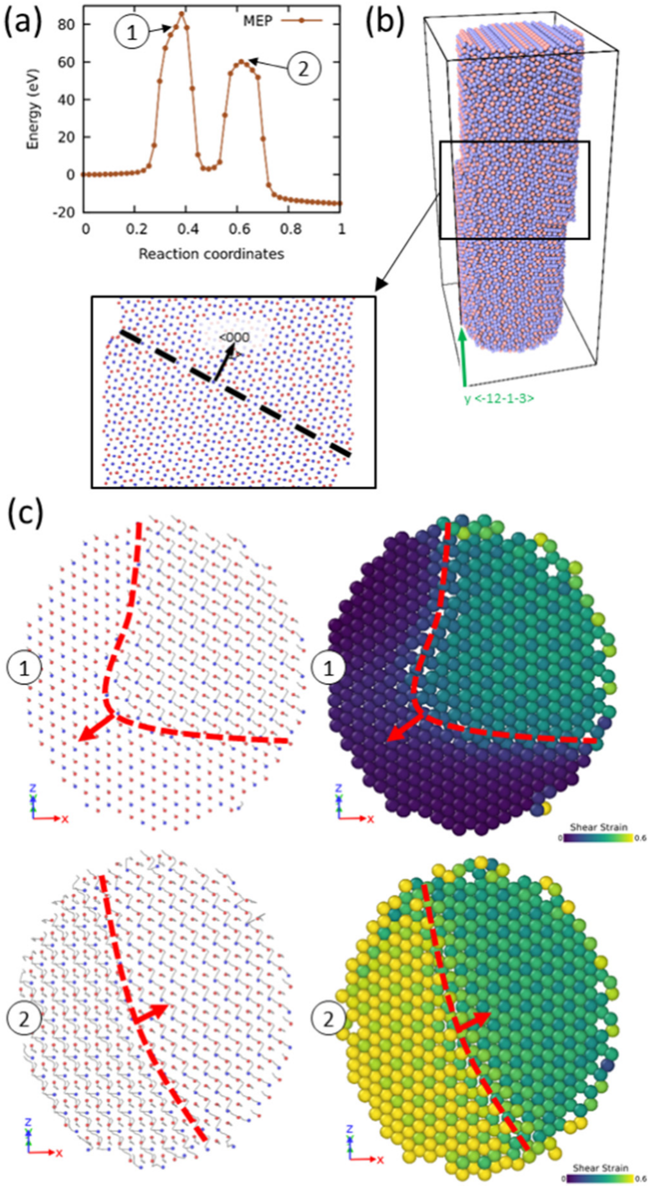

Fig. 4. Basal dislocation in C14 Mg_2Ca Laves phase nano-pillars. (a) Activation energy and minimum energy path for the nucleation of a dislocation in the basal plane. (b) Snapshot of the 8 nm nano-pillar after full slip. Inset of the glide plane and surface steps. (c) Atomic displacements and atomic shear strain of the triple-layer atoms involved in the slip mechanism, for two intermediate configurations indicated in (a). Dislocation line and dislocation motion indicated with dashed red line and red arrow, respectively. (For interpretation of the references to colour in this figure legend, the reader is referred to the web version of this article.)

To validate SS as the most probable mechanism for dislocation propagation, we have performed NEB calculations of the slip in a compressed nano-pillar (Fig. 4). The considered system was a cylinder with diameters of 8 nm (40,470 atoms) cut out of a C14 Mg_2Ca bulk phase. The pillar axis was oriented along $\langle \bar{1}2\bar{1}\bar{3}\rangle$ and strained by applying force fields at each end. The initial configuration was a non-faulted pillar, strained with a magnitude equivalent to a full slip, corresponding to an axial stress of approximately 250 MPa. Note that the intrinsic local stress was homogenous throughout the pillar (see Supplementary materials). The final configuration was a nearly stress-free pillar that has undergone a full slip of $^1/_3\langle 11\bar{2}0\rangle$ in the basal plane under maximum Schmid factor (Fig. 4b). Our NEB calculations clearly show the nucleation of slip from the surface, followed by its propagation *via* SS (Fig. 4c and Movie 4 in Supplementary materials). In particular, the first (Fig. 4c–1) and second (Fig. 4c–2) synchroshockley dislocations propagate by both the typical atomic displacements of the SS mechanism described above and the atomic von Mises shear strain [22,23,25]. The associated MEP exhibits a characteristic two-maxima profile corresponding to two successive SS (Fig. 3a). The details of the dislocation propagation remain unknown and suggested mechanisms, such as the vacancy-aided kink propagation [24], need to be further investigated. Nonetheless, with this NEB approach on a nano-pillar, we demonstrated the motion of a basal dislocation by SS.

The confirmation of the synchroshear mechanism in the present work as the most favourable mechanism for basal slip in a Laves phase is an important insight for future experimental and theoretical investigations of plasticity in general complex intermetallics. The final validation of SS will require a direct comparison between nano-mechanical experiments and nano-scale simulations at the experimental temperature.

Supplementary data to this article can be found online at https://doi.org/10.1016/j.scriptamat.2019.03.016.

Acknowledgements

Simulations were performed with computing resources granted by RWTH Aachen University under projects rwth0297 and thes0371. This project has received funding from the European Research Council (ERC) under the European Union's Horizon 2020 research and innovation programme (grant agreement No 639211).

References

[1] T.M. Pollock, Science 328 (2010) 986–987.

[2] A.J. Knowles, A. Bhowmik, S. Purkayastha, N.G. Jones, F. Giuliani, W.J. Clegg, D. Dye, H.J. Stone, Scr. Mater. 140 (2017) 59–62.
[3] P.M. Hazzledine, K.S. Kumar, D.B. Miracle, A.G. Jackson, MRS Proc. 288 (1992) 591.
[4] P.M. Hazzledine, P. Pirouz, Scr. Metall. Mater. 28 (1993) 1277–1282.
[5] M.F. Chisholm, S. Kumar, P. Hazzledine, Science. 307 (2005) 701–703 80-.
[6] Y. Zhong, J. Liu, R.A. Witt, Y. ho Sohn, Z.K. Liu, Scr. Mater. 55 (2006) 573–576.
[7] O. Vedmedenko, F. Rösch, C. Elsässer, Acta Mater. 56 (2008) 4984–4992.
[8] W. Zhang, R. Yu, K. Du, Z. Cheng, J. Zhu, H. Ye, Phys. Rev. Lett. 106 (2011) 2–5.
[9] Z.Q. Yang, M.F. Chisholm, B. Yang, X.L. Ma, Y.J. Wang, M.J. Zhuo, S.J. Pennycook, Acta Mater. 60 (2012) 2637–2646.
[10] N. Takata, H. Ghassemi Armaki, Y. Terada, M. Takeyama, K.S. Kumar, Scr. Mater. 68 (2013) 615–618.
[11] Y. Liu, W.C. Hu, D.J. Li, K. Li, H.L. Jin, Y.X. Xu, C.S. Xu, X.Q. Zeng, Comput. Mater. Sci. 97 (2015) 75–85.
[12] L. Liu, P. Shen, X. Wu, R. Wang, W. Li, Q. Liu, Comput. Mater. Sci. 140 (2017) 334–343.
[13] M.L. Kronberg, Acta Metall. 5 (1957) 507–524.
[14] G. Henkelman, B.P. Uberuaga, H. Jónsson, J. Chem. Phys. 113 (2000) 9901.
[15] G. Henkelman, H. Jónsson, J. Chem. Phys. 113 (2000) 9978.
[16] E. Maras, O. Trushin, A. Stukowski, T. Ala-Nissila, H. Jónsson, Comput. Phys. Commun. 205 (2016) 13–21.
[17] S. Brochard, P. Hirel, L. Pizzagalli, J. Godet, Acta Mater. 58 (2010) 4182–4190.
[18] J. Guénolé, J. Godet, L. Pizzagalli, Model. Simul. Mater. Sci. Eng. 18 (2010).
[19] K.-H. Kim, J.B. Jeon, B.-J. Lee, Calphad 48 (2015) 27–34.
[20] S. Plimpton, J. Comput. Phys. 117 (1995) 1–19.
[21] P.M. Anderson, J.P. Hirth, J. Lothe, Theory of Dislocations, Cambridge University Press, 2017.
[22] M.L. Falk, J.S. Langer, Phys. Rev. E 57 (1998) 7192–7205.
[23] F. Shimizu, S. Ogata, J. Li, Mater. Trans. 48 (2007) 2923–2927.
[24] K.S. Kumar, P.M. Hazzledine, Intermetallics 12 (2004) 763–770.
[25] A. Stukowski, Model. Simul. Mater. Sci. Eng. 18 (2010), 015012. https://doi.org/10.1088/0965-0393/18/1/015012.